UNIVERSITY OF SOUTHAMPTON

# COMPACT ULTRASHORT PULSE DIODE PUMPED VERTICAL CAVITY SURFACE EMITTING LASER

by

**Kęstutis Vyšniauskas**

A thesis submitted for the degree of
Doctor of Philosophy

**Department of Physics and Astronomy**
**Faculty of Science**

**May 2003**

UNIVERSITY OF SOUTHAMPTON

ABSTRACT

FACULTY OF SCIENCE

DEPARTMENT OF PHYSICS AND ASTRONOMY

Doctor of Philosophy

# COMPACT ULTRASHORT PULSE DIODE PUMPED VERTICAL CAVITY SURFACE EMITTING LASER

by Kęstutis Vyšniauskas

This thesis describes work carried out at Southampton University on the design of optically–pumped external-cavity surface emitting lasers (DP-VECSELs) and semiconductor saturable absorber mirrors, and their demonstration in the optimal laser configuration for passively mode–locked laser operation. Recent development of these structures combines the approaches of novel designs with control of their dispersive properties. These designs have been implemented in metal-organic chemical vapor deposition (MOCVD) technology, considering specific features of molecular beam epitaxy (MBE) growth technology, and in principle drawing on the advantages of both.

This work describes direct and indirect multilayer design methods and their successful applications to the design of DP-VECSELs and saturable absorber mirrors. Two specific indirect design algorithms were used to enhance such device performance. In general indirect design methods are very helpful if one wants to achieve particular results and there is still a lot of freedom and work that can be done for specific algorithm development.

A novel superlattice-based design of saturable absorber mirror (SUSAM) is introduced for the first time. It is shown that an additional strained superlattice can be used to shorten absorption recovery characteristics without increasing significantly non-saturable losses (<0.3%). A SUSAM has been successfully used to mode lock a DP-VECSEL at 1034 nm, generating 5-ps long (FWHM) pulses at a repetition rate of 330 MHz with average power of up to 45 mW in a circular diffraction-limited beam. Only single-step standard MOCVD growth is needed to manufacture SUSAMs. Three types of SUSAM are discussed. A few particular designs seem to be very promising for the high volume production.

The experimental part of the thesis can be divided into two parts which describe sample characterization, and the use of structures for CW and CW-mode-locking laser regimes. Characterization of the grown samples involves reflection or transmission measurements, photoluminescence measurements, pump-probe experiments and the CW and mode-locking results. Some experiments have been done to study global instabilities that seem to be an interesting problem in mode-locking. The whole thesis concludes with a summary, and some promising ideas for future improvements for next generation lasers and laser-based devices.

# CONTENTS

# ACKNOWLEDGEMENTS

I wish to express my gratitude to my supervisor Prof. Anne Tropper for her interest in this work, for giving me the opportunity to work in an extremely stimulating environment, and without whose unfailing help and encouragement this work would not have been possible.

I am also very grateful to all our group members who helped me during this period of research at Southampton.

I would like to thank University of Southampton for their encouragement and sponsorship of my graduate work during the last three years. I would also like to gratefully acknowledge the financial support of EPSRC.

Finally, I thank my patient wife, my family and friends for their continuing support.

# CHAPTER I

## CH.I. 1. Introduction

Efficient low- and high-power compact, easily manufacturable laser sources of tunable UV, VIS, NIR wavelength radiation with good spatial-beam profile characteristics are necessary for many applications including communications, spectroscopy, process monitoring, laser radar, and materials processing. Typical ultra-short pulse laser sources are, however, large and expensive. Therefore it is advantageous to have simpler ultra-short pulse sources with a minimum number of components. A compact pulse source such as a mode-locked semiconductor laser with comparable technical specifications to those standard laser systems would be attractive because of its simplicity and cost effectiveness.

In contrast, in-plane and electrically pumped semiconductor lasers can emit high power and single transverse mode beams – they are compact, efficient, and reliable. However, edge-emitting narrow-strip lasers emit elongated-profile beams with CW power reaching, at best, 0.3-0.4 W in a single transverse mode; typically less than 0.3 W is coupled into single mode fiber.[1,2,3] High power up to 10 W is achievable in wide-stripe lasers with multi-transverse mode output. However, the output beam of these wide-strip devices is strongly astigmatic, and therefore additional optics are needed for beam reshaping and coupling into single-mode fiber. Electrically pumped vertical cavity surface emitting lasers (VCSELs) have the desired circular output beams. For small emitter diameters (<10 μm), VCSELs operate in a single transverse mode with output power limited to less than about 10 mW.[4,5] For large diameters (>100 μm), VCSELs output power can be higher than 100 mW.[6,7] However the output beam has multiple transverse modes. Using an external cavity, a large-diameter VCSEL can be used, but the CW output power is limited by the lateral current injection and is only 2.4 mW.[8]

A new semiconductor laser technology, the optically pumped semiconductor vertical external cavity surface emitting laser (OPS-VECSEL) offers many advantages over in-plane lasers and electrically pumped diode lasers.[9,10] OPS-VECSELs combine the approaches of diode pumped solid state lasers, and semiconductor quantum well (QW) vertical cavity surface emitting lasers, drawing on the advantages of both. The use of this

approach allows the generation of high power in a circular near diffraction limited output beam directly from a semiconductor laser. A diode-pumped strain-compensated multi quantum well InGaAs-GaAs-GaAsP VECSEL operating continuous wave near 1.004 μm with output power of 0.69 W in $TEM_{11}$ mode, 0.52 W in $TEM_{00}$ mode, and 0.37 W coupled to a single mode fiber has been demonstrated.

Typically the output of a commercial multimode pump diode laser is focused onto the optically pumped semiconductor chip. The lasing cavity is formed between a high reflectivity mirror on the chip and one or more external spherical mirrors. Multiple QWs provide gain, and the external mirrors control the transverse mode. Thus, a diode-pumped vertical cavity surface emitting laser (DP-VECSEL) divides optical functions between the multi transverse mode diode laser pump which generates optical power, and the DP-VECSEL itself, which converts pump power to the circular fundamental transverse mode. Bandgap engineering of the multi QW semiconductor structures allows the design of active laser media with desirable laser properties, such as low threshold, high output power, high conversion efficiency, and wide wavelength tuning over >100 nm range. The operating wavelength of the laser can in principle be chosen by design from ultraviolet to the infrared wavelengths while keeping the pumping wavelength above bandgap. The interband absorption is spectrally broad (more than 40 nm). This ensures efficient absorption of the spectrally broad pump diode emission, and eliminates sensitivity to pump diode temperature and wavelength variation. Due to short pump absorption lengths (~1μm) in semiconductors, the pump efficiency is high, and there is no electrical power loss. The laser mode size (better than 50 μm in diameter) on the DP-VECSEL raises the power threshold for optical surface damage. The disadvantages of the DP-VECSEL approach are only the need for an external pump and an external cavity, which increase the size and complexity of the laser.

The first CW mode locking studies of electrically pumped semiconductor laser that produced reproducible pulses of 20 ps duration and less were carried out in a relatively short (5 cm) external cavity using uncoated diodes for convenience.[10,11,12] However the pulses were not Fourier transform limited. Sub-100 fs pulses have been demonstrated by compressing strongly chirped picosecond pulses from a synchronously pumped InGaAs-InP multi QW VECSEL.[13] The fundamental limit to the pulse width from a mode locked semiconductor laser is the gain bandwidth, which typically allows to have ~ 50 fs pulses. The actual pulse widths from mode locked semiconductor lasers to date are substantially

longer. However, the pulses are strongly chirped and that is the main cause of the long pulses. Various chirp compensation techniques inside and/or outside the mode locked cavity can be used to compress the pulses.

Due to the small gain saturation energy, the output power from a mode locked semiconductor laser is small. The peak power is limited to a few watts in the best cases. In comparison with other mode locked solid state lasers and dye lasers, semiconductor lasers are still low in average output power and long in pulse width. The use of DP-VECSEL gain structures in combination with the quantum-well-based semiconductor saturable absorber allows improve these characteristics of passively mode locked semiconductor lasers. In general these quantum-well-based semiconductor saturable absorbers have been used for numerous applications, such as laser tuning elements, wavelength-sensitive detectors[14], optical noise pulse suppression in high-speed optical communication[14], and in particular for passive mode-locking of a variety of solid-state laser materials including Ti:sapphire, Cr:LiSAF, Cr:YAG, Nd:$YVO_4$, Nd:YLF, Yb:YAG.[15-21] Fast recovery of the saturable absorption was achieved, for example using quantum wells (QW) grown by molecular-beam-epitaxy (MBE) under very critical growth conditions at low temperatures or using ion-implantation to enhance carrier recombination rates. The use of low temperature MBE growth or ion-implantation however introduces non-saturable losses. It has recently been shown that a semiconductor saturable absorber mirror (SESAM) can be used in a DP-VECSEL cavity to establish passive mode locking.[22] However the performance of these inherently low-gain devices is sensitive to the non-saturable loss.

In this work, for the first time a novel superlattice-based design of saturable absorber mirror (SUSAM) is introduced which has been grown by metal-organic chemical-vapor deposition (MOCVD) under standard conditions. In SUSAM devices a strained superlattice, adjacent to the absorbing quantum well, provides relatively rapid absorption recovery (50-130 ps) without increasing significantly non-saturable losses. Three different types of SUSAM designs are discussed. SUSAM has been used to mode-lock a DP-VECSEL at a repetition rate of 330 MHz generating 5 ps long pulses (FWHM – full width at half maximum) at 1034 nm. The maximum average output power of 45 mW was obtained in a circular diffraction-limited beam. The insertion loss of this device is estimated approximately to be 0.3%. It is also shown that SUSAM requires only a single-step MOCVD growth and there is no need for post-growth and chemical etching procedures to complete whole saturable absorber device. SUSAM has proved to have low-

insertion-loss, to be cost effective, easily manufacturable and effective in providing the necessary self-starting passive mode locking operation.

It is well known that most designs of semiconductor devices are limited because of specific requirements (for example, pump wavelength determines band-gap limitations in DP-VECSEL designs) by low available refractive index contrast and the reflection exceeding ~30% at air-semiconductor boundary is dominated. Therefore any specific and necessary additional AR coating could make the whole fabrication procedure less flexible, less cost effective and more complex involving dry or wet chemical etching procedures if additional technology is involved ($SiO_2/TiO_2$ based AR coatings). This could lead to additional insertion of undesirable losses with the possible degradation resulting in uncontrolled reduction of optical damage threshold. Specially designed semiconductor-based AR coatings, mirrors with their specific amplitude and phase properties could be of great use for potential integration with DP-VECSEL gain elements, SUSAMs, chirp compensating filters, mirrors. On the one hand such structures with desired amplitude-frequency and phase-frequency characteristics are demanding high refractive index contrasts. On the other hand semiconductor is not a convenient material for device dispersion formation because the allowed variation of refractive index is quite small. For example, the refractive index of AlGaAs is a function of the Al fraction mostly because the Al fraction dictates the band-gap energy. High-index contrast can be obtained only by approaching the band edge at the lower fractions. As a result there is a material dispersion that cannot be completely avoided. It has to be taken into account material and device dispersion. The maximum allowed variation of refractive index is then only 0.6. Therefore a lot of work in this thesis has been done on the development of specific algorithms that could allow to achieve relatively simple device designs with necessary amplitude-frequency, phase-frequency characteristics using low contrast materials. Two algorithms have been developed that solve indirect design problems. It is shown that both algorithms are effective in achieving original design solutions. One algorithm uses statistical approach to improve discrimination against solutions solving indirect synthesis problem. Another one also uses statistical approach but to have more control over independent weight factors that form convergence conditions in the desired spectral region. Only very interesting design solutions that satisfy MOCVD growth requirements are presented. The large amount of numerical simulations and achieved results concludes that the desired specifications of the entire device can be achieved optimizing one part of the device

(mostly AR region), while keeping the entire device as simple as possible. It is the most straightforward way to achieve design that is much more technologically simple and meets manufacturing demands. Very specific SUSAM designs illustrate that broad band AR coating can form linear GDD (group delay dispersion) for the entire device using low refractive index semiconductor materials. Therefore novel concept for the design of semiconductor devices is introduced and discussed in this work.

The experimental results and observations described in this work could be summarized as follows. First of all, the successful development and demonstration of SUSAMs in passively mode-locked DP-VECSEL laser is described. It is shown that SUSAMs are low-insertion loss devices (non-saturable loss ~ 0.3%) with sufficiently fast absorption recovery characteristics (3-repeat superlattice SUSAM ~ 50ps, and 2-repeat superlattice SUSAM ~130 ps), and which can be manufactured using standard single-step MOCVD growth. No additional post-growth processing is required. In addition, no further SUSAM degradation has been observed. In principle is shown that the strained superlattice adjacent to QWs quenches the carrier population in the absorbing QWs, effectively shortening the carrier lifetime without increasing significantly non-saturable losses in the entire SUSAM device. The strained absorbing active region can be integrated anywhere in the complex SUSAM device if oppositely strained materials are used to balance out the strain over an entire structure. Therefore SUSAMs with AR coatings (preferably with dispersion control) and strong loss mechanism (heavy delta doping below buffer layer) below integrated mirrors is necessary step for further passively mode-locked DP-VECSEL development in order to avoid any pulse break-up processes, instabilities.

In general, for the first time it is shown that a DP-VECSEL can be passively mode locked by introducing a novel superlattice-based semiconductor saturable absorber mirror SUSAM into the external cavity. By bandgap engineering, the saturable absorbers can be coordinated at lasing wavelength. Therefore, a properly designed DP-VECSEL together with SUSAM allows to have compact, ultra-short pulse laser source, which may produce high quality short pulses directly from the laser cavity without any need for an additional external cavity pulse compression.

## CH.I. 2. References


1. L. A. Coldren and S. W. Corzine, *Diode Lasers and Photonic Integrated Circuits.* New York, Academic, 1997.
2. M. Sagawa, T. Toyonaka, K. Hiramoto, K. Shinoda, and K. Uomi, "High-power highly-reliable operation of 0.98 μm InGaAs-InGaP strained-compensated single-quantum-well lasers with tensile-strained InGaAsP barriers," *IEEE J. Select. Topics Quantum Electron.,* vol. 1. pp. 189-794, 1995.
3. J. Temmyo, M. Sugo, T. Nishiya, T. Tamamura, F. Bilodeau, and K. O. Hill, "Improved coupling efficiency of a strained InGaAs-AlGaAs quantum-well laser into a fiber Bragg grating," *IEEE Photon. Technol. Lett.,* vol. 9, pp. 581-583, 1997.
4. K. D. Choquette, K. L. Lear, R. P. Schneider, K. M. Geib, J. J. Figiel, and R. Hull, "Fabrication and performance of selectively oxidized vertical-cavity lasers," *IEEE Photon. Technol. Lett.,* vol. 7, pp. 1237-1239, 1995.
5. R. Jager, M. Grabherr, C. Jung, R. Michalzik, G. Reiner, B. Weigl and K. J. Ebeling, "57% wallplug efficiency oxide-confined 850 nm wavelength GaAs VECSEL's," *Electron. Lett.,* vol. 33, pp. 330-331, 1997.
6. D. B. Young, J. W. Scott, F. H. Peters, M. G. Peters, M. L. Majewski, B. J. Thibeault, S. W. Corzine, and L. A. Coldren, "Enhanced performance of offset-gain high-barrier vertical-cavity surface-emitting lasers," *IEEE J. Quantum Electron.,* vol. 29, pp. 2013-2021, 1993.
7. J. J. Zayhowski and A. Mooradian, "Single-frequency microchip Nd lasers," *Opt. Lett.,* vol. 14, pp.24-26, 1989.
8. M. A. Hadley, G. C. Wilson, K. Y. Lau, and J. S. Smith, "High single-transverse-mode output from external-cavity surface-emitting laser diodes," *Appl. Phys. Lett.,* vol. 63, pp. 1607-1609, 1993.
9. W. Koechner, *Solid State Laser Engineering,* 4th ed. New York, Springer-Verlag, 1996.
10. P. T. Ho, L. A. Glasser, H. A. Haus and E. P. Ippen, *Picosecond Phenomena* eds. C. V. Shank, E. P. Ippen and S. L. Shapiro, Springer-Verlag, New York, 1978.
11. P. T. Ho, L. A. Glasser, E. P. Ippen and H. A. Haus, Appl. Phys. Lett. 33, pp. 241, 1978.

12. L. A. Glasser, Electron. Lett. 14, pp. 725, 1978.

13. W. H. Xiang, S. R. Friberg, K. Watanabe, S. Machida, Y. Sakai, H. Iwamura, Y. Yamamoto, "Sub-100 femtosecond pulses from an external-cavity surface-emitting InGaAs/InP multiple quantum well laser with soliton-effect compression," Appl. Phys. Lett. 59, 21 October 1991.

14. D. A. B. Miller, *IEEE J. Quantum Electron.*, vol. 30, pp. 732-749, 1994.

15. Zhigang Zhang, Tadashi Nakagawa, Hideyuki Takada, Kenji Torizuka, Takeyoshi Sugaya, Taisuke Miura, Katsuyuki Kobayashi, "Low-loss broadband semiconductor saturable absorber mirror for mode-locked Ti:sapphire lasers," *Opt. Commun.* 176 (2000) 171-175.

16. Sérgio Tsuda, Wayne H. Knox, S. T. Cundiff, W. Y. Jan, and J. E. Cunningham, "Mode-Locking Ultrafast Solid-State Lasers with Saturable Bragg Reflectors," *IEEE*, vol. 2, No. 3. September 1996.

17. D. Kopf, G. Zhang, R. Fluck, M. Moser, and U. Keller, "All-in-one dispersion-compensating saturable absorber mirror for compact femtosecond laser sources," *Opt. Lett.*, vol. 21, pp. 486-488,1996.

18. S. Tsuda, W. H. Knox, E. A. de Souza, W. Y. Jan, and J. E. Cunningham, "Low-loss intracavity AlAs/AlGaAs saturable Bragg reflector for femtosecond mode locking in solid-state lasers," *Opt. Lett.*, vol. 20, pp. 1406-1408, 1995.

19. U. Keller, T. H. Chiu, and J. F. Ferguson, "Self-starting and self-Q-switching dynamics of passively mode-locked Nd:YLF and Nd:YAG lasers, " *Opt. Lett.*, vol. 18, pp. 217-219, 1993.

20. R. Paschotta, J. Aus der Au, G. J. Spühler, F. Mourier-Genoud, R. Hövel, M. Moser, S. Erhard, M. Karszewski, A. Giesen, U. Keller, " Diode-pumped passively mode-locked lasers with high average power," *Appl. Phys. B* (2000).

21. C. Hönninger, G. Zhang, A. Giesen, and U. Keller, "Femtosecond Yb:YAG laser using semiconductor saturable absorbers," *Opt. Lett.*, vol. 20, pp. 2402-2404, 1995.

22. S. Hoogland, S. Dhanjal, A. C. Tropper, *Member, IEEE,* J. S. Roberts, R. Häring, R. Paschotta, F. Morier-Genoud, and U. Keller, "Passively Mode-Locked Diode-Pumped Surface-Emitting Semiconductor Laser," *IEEE Photon. Technol. Lett.*, vol. 12, pp. 1135-1137, 2000.

# CHAPTER II
# THEORETICAL BACKGROUND

## CH.II. 1. Introduction

This chapter describes in detail theoretical principles applied in this work to develop the multilayer-based optically pumped semiconductor lasers and saturable absorber structures. Any multilayer-based optical system can be considered as an optical interference filter, or a combination of such filters. It is well known that optical interference filters are widely used for optics, spectroscopy, laser optics, solar energy, semiconductor and space technology. These various applications require filters with specific characteristics. The antireflection (AR) coating of optical surfaces was one of the first problems solved with the aid of thin films and it is also discussed in the first book on the subject, published in 1946.[1] Since that time a lot of work has been done on AR coatings and high reflectors (HR) for spectral regions that extend from the ultraviolet to the infrared. AR coatings are particularly important in the infrared spectral region because many optical materials used in this region are semiconductors with high refractive indices.

There are many different methods for the design of interference film system. The most general method for calculating spectral characteristics of multilayer optical filters is based on a matrix formulation of the boundary conditions at the film surfaces derived from Maxwell`s equations.[1-9] Given the thickness and refractive index of each layer of the multilayer, as well as the indices of the substrate and incident medium, spectral characteristics can be calculated. For an interference film system of average complexity, a satisfactory design can be obtained with analytical methods based on series expansions. However, for some cases in which a system with a specific spectral behavior is required, the analytical synthesis methods are too complicated or even impossible to apply. For such cases, indirect synthesis, optimization methods including gradient, damped-least-squares, inverse Fourier synthesis methods, etc. for automatic design of optical thin-film systems have been developed. Gradient algorithms converge on the solution more slowly than damped least squares in many cases, but allow considerable freedom in the choice of the merit function whereas damped least squares require a least-squares merit function.

However, it should be pointed out that these methods give a slightly deviant design. If the target is unrealistic, then not only will the attainable result not match the target, but the merit function may have less sensitivity to the changes that would bring the design closer to the target, and the whole optimization process will be degraded. Methods based on the inverse Fourier transform are more promising for the generation of totally new designs.[10,11] It is necessary only to specify the required spectral curve, and then the number of layers, their thicknesses, and their refractive indexes are all obtained as a result of one synthesis process. However, it is limited to non-absorbing and non-dispersive materials. The interested reader is referred to one of the many review articles and text-books for a more in-depth overview of the topic.[1-30] Here it is sufficient to state that, to this day, there is no one algorithm that is superior in all situations. The best method for the solution of a given problem depends on the problem itself and on the type of solution required. Therefore new or improved methods are always welcome because they may have different capabilities.

The purpose of the investigation described in this chapter is to describe in some detail already known direct and indirect design methods, and to develop more flexible and better adapted systematic procedures for the design of semiconductor-based devices such as vertical-cavity surface-emitting lasers, and semiconductor saturable absorber mirrors. These devices for external cavity mode-locked semiconductor lasers are particularly interesting from the design point of view because the target design is multi-sectional and multi-functional with very limited available refractive index contrasts. From a technological point of view, the optimum solution is probably the system with the very best performance that can be obtained experimentally including manufacturing errors. The maximum complexity of the design will also depend on the available technology. From an economic point of view the optimum design solution will be that, which provides the minimum acceptable performance at the lowest possible cost. For a device that is to be mass-produced, the lowest cost will be associated with the highest production yield. Therefore final device design that will satisfy these requirements may be quite different from the computationally optimal solutions.

This chapter is organized as follows. First of all the conventional description of multilayer optical filters is summarized and notation is defined. Secondly, the two most general and basic direct design methods for multilayer optical filters, known as the matrix method and the tanh substitution technique are introduced. These are recognized as

simplest direct design methods to determine the general spectral characteristics of combinations of quarter-wave and half-wave multilayer structures. Next, attention will be paid to indirect multilayer design methods, including the most interesting from my point of view; namely those that are more effective and easily adaptable. The algorithms used in this work are described using block diagrams of the flow of calculations. A short discussion of the variation of spectral characteristics for a number of different types of possible inhomogenities in thin semiconductor layers is included. A simple model, which should hold in many cases, to account for vertical and lateral disorder in multilayer optical filters is introduced as well.

Theoretical background is given to establish necessary characteristics of CW and CW passively mode-locked semiconductor lasers. Finally, numerical results of spectral characteristics for a number of semiconductor structures are shown and summarized in table.

## CH.II. 2. Multilayer-based Devices

Most widely recognized is the way of describing multilayer optical filters where the optical thicknesses of the alternating layers are designated as fractions of $\lambda_0/4$, with $\lambda_0$ being the design wavelength. Let, for instance, a multilayer to be a two-component one, consisting of alternating layers featuring high $n_H$ and low $n_L$ refractive indices. Consider the example of writing down structure of such a multilayer:

17 S l LH 6L HLHLH 6L HLHLH 8L H 2L l 1.0

Number 17 on the extreme left shows the total number of layers in the given multilayer, the following letter S stands for the substrate. Then there is a consecutive list of the optical thicknesses in the direction from substrate to the outer space. The letters H and L refer to the layers having refractive indices of $n_H$ and $n_L$, respectively. The numerical coefficients before them show the optical thicknesses of the layer as fractions of $\lambda_0/4$. If a coefficient is absent, the corresponding layer has a quarter-wave optical thickness. The structural description is accompanied by indication of refractive indices for the substrate and the

layers. The outer space is air. Otherwise its refractive index has to be specified. In the case of very dispersive materials, refractive indices have to be specified in the region of spectral interest. For anisotropic materials refractive indices have to be given for both ordinary and extraordinary waves. In addition substrate orientation, doping, scattering loss, optical damage threshold, sensitivity to the temperature, ... have to be specified in a full description.

If repeated groups of layers occur in a coating, the number of repeats is usually shown as a power index, and the repeated group is put in brackets. For example, the two descriptions below are equivalent:

17 S l LH 6L HLHLH 6L HLHLH 8L H 2L l 1.0 and 17 S l LH 6L $[HL]^2$H 6L $[HL]^2$H 8L H 2L l 1.0

When a multilayer has layers of three or more different materials, additional designations are introduced: M, Z, C, .... The letter M is usually used to designate the layers with the refractive index lying between $n_H$ and $n_L$. If layers with their specific intermediate and not equal refractive indexes are used then the letters Z, C for example could be introduced.

The spectral curves of the transmittance and reflectance can be conveniently presented as a function of $\lambda / \lambda_0$ or $\lambda_0 / \lambda$. Substituting the concrete value of $\lambda_0$ we determine the thicknesses of the layers and the spectral band where it will apear.

## CH.II. 3. Direct Calculation Methods for Multilayer Optical Filters

### CH.II. 3-1. *Matrix Method*

We will be most interested in the solutions in the case of a multiple layered structure, in each layer of which the absorption and refractive index are constant. In this case, we can obtain the exact, general solution for a given layer, and obtain the solution for the entire multilayer structure using matrix techniques. Let us consider a layer system of

homogeneous isotropic and nonmagnetic materials. The incident wave is monochromatic with angular frequency $\omega$, so at any point in the structure, the wave is of the form

$$E = \frac{1}{2} E_0 e^{i\omega t} + c.c. \qquad \text{[CH.II. 3-1/1]}$$

Hence, the wave equation can be written in the form

$$\frac{d^2 E_0}{dz^2} = -\left[ \frac{n^2 \omega^2}{c^2} - \frac{\alpha^2}{4} - i\frac{n\alpha\omega}{c} \right] E_0 \qquad \text{[CH.II. 3-1/2]}$$

for a particular uniform layer, where we have anticipated a convenient notation for the general solution,

$$E_0(z) = Fe^{-i\left(k - i\frac{\alpha}{2}\right)z} + Be^{i\left(k - i\frac{\alpha}{2}\right)z}. \qquad \text{[CH.II. 3-1/3]}$$

In [CH.II. 3-1/2] and [CH.II. 3-1/3], the symbols have their usual meanings: $n$ is the refractive index, $\alpha$ is the absorption coefficient, $c$ is the velocity of light in free space, and the wave vector $k = 2\pi n / \lambda$ (where $\lambda$ is the free space wavelength). $F$ is the amplitude of the forward-going wave and $B$ is the amplitude of the backward-going wave. $F$ and $B$ are in general complex. Note that this sum of forward and backward waves is a general solution for [CH.II. 3-1/2] for a uniform layer, and allows matching of amplitude and derivative at a boundary.

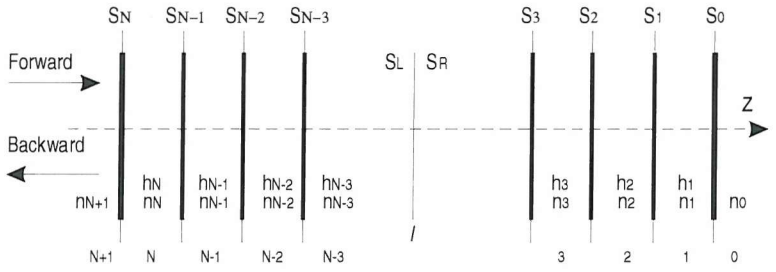


**Fig. CH.II. 3-1.1:** Schematic of a Multilayer Structure.

At a given interface between two layers of different materials, the boundary conditions are continuity of the transverse component of the electric field, which here means continuity of $E_0$, and continuity of the transverse component of the magnetic field,

which here results in continuity of $dE_0/dz$. The relations then between the wave amplitudes on the left of a boundary ($F_L$ and $B_L$) and those on the right ($F_R$ and $B_R$) are

$$\begin{cases} F_L = \frac{1}{2}[F_R(1+\sigma)+B_R(1-\sigma)] \\ B_L = \frac{1}{2}[F_R(1-\sigma)+B_R(1+\sigma)] \end{cases}, \qquad \text{[CH.II. 3-1/4]}$$

where

$$\sigma = \frac{ik_R + \alpha_R/2}{ik_L + \alpha_L/2}, \qquad \text{[CH.II. 3-1/5]}$$

in which the subscripts $L$ and $R$ refer to the materials on the left and right of the boundary respectively. Using [CH.II. 3-1/4] and [CH.II. 3-1/5] we can define a column vector

$$S = \begin{bmatrix} F \\ B \end{bmatrix}, \qquad \text{[CH.II. 3-1/6]}$$

whose elements are the forward and backward wave amplitudes. This matrix formulation differs from, e. g., (7) by using forward and backward amplitudes rather than amplitude and derivative, but these are both valid mathematically. Then we can write

$$S_L = DS_R, \qquad \text{[CH.II. 3-1/7]}$$

where $S_L$ and $S_R$ refer to the amplitude vectors on the left and right of the boundary respectively, in which

$$D = \begin{bmatrix} \frac{(1+\sigma)}{2} & \frac{(1-\sigma)}{2} \\ \frac{(1-\sigma)}{2} & \frac{(1+\sigma)}{2} \end{bmatrix}. \qquad \text{[CH.II. 3-1/8]}$$

Using the same conventions we can also define a propagation matrix, $P$, that relates the wave amplitude vector just inside the right hand side of a layer to those just inside the left side of the same layer

$$P = \begin{bmatrix} e^{i(k-i\alpha/2)h} & 0 \\ 0 & e^{-i(k-i\alpha/2)h} \end{bmatrix}, \qquad \text{[CH.II. 3-1/9]}$$

where $h$ is the thickness of the layer. Hence we can relate the wave amplitude vector, $S_1$, just inside the right hand side of the right-most layer (e. g., at the mirror surface), to the wave amplitude vector just to the left of the left-most layer of an $l$ layer structure (e. g., the entrance face of the whole structure) through the matrix multiplication

$$S_{l+1} = \left[\prod_l D_l P_l\right] S_0, \qquad \text{[CH.II. 3-1/10]}$$

where we multiply to the left with increasing $l$. The $l+1$th layer is the material to the left of the whole structure; only its absorption and refractive index are needed, not its thickness. When the mirror layer structure is included in the calculation, a convenient form for the vector $S$ for the right-most interface is to choose it to have unit forward amplitude and zero backward amplitude just to the right of the right-most interface. This means that we are presuming a wave leaks through the mirror, but that no wave is incident from the right. The overall reflectivity of the structure can be estimated from the ratio of the forward and backward amplitudes in the vector $S$ just to the left of the left-most interface. Note that the phase change on reflection can change quite markedly with the wavelength. The phase change on reflection can be estimated from the ratio of complex part and real part of amplitude reflectivity taking its tan. Group delay, group-delay dispersion (GDD), third-order dispersion (TOD), and fourth-order dispersion (FOD) can be calculated as the first, second, third, and fourth derivatives of phase shift respectively by the angular frequency.

## CH.II. 3-2. *Tanh Substitution Technique*

The tanh substitution technique provides a simple way to determine the reflectivity of combinations of quarter-wave and half-wave multilayer structures over the spectral region of interest. The benefit of this method over other analytical methods is the simplicity with which final expressions are obtained. Let's consider the Fabry-Perot cavity illustrated in Fig. CH.II. 3-2.1.

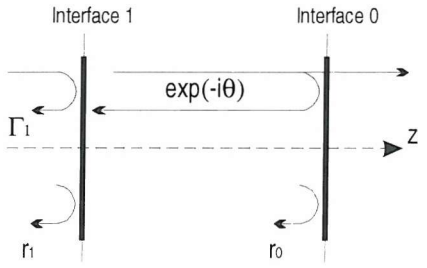


**Fig. CH.II. 3-2.1:** Schematic of a Fabry-Perot cavity.

Using the symbols defined in Fig. CH.II. 3-2. 1., we can write down the overall field reflectivity of the combined interfaces as seen at interface 1

$$\Gamma_1 = \frac{|r_1| + |r_0|\exp(-i\theta)}{1 + |r_1||r_0|\exp(-i\theta)}; \quad |r_j| = \frac{n_{j-1} - n_j}{n_{j-1} + n_j}, \qquad \text{[CH.II.3-2/1]}$$

where $r_{0,1}$ are the interface field reflectivities as seen from the left, and $\theta$ is the spatial phase shift experienced by the wave in traversing twice the distance between the two interfaces. The above equation can be simplified using the hyperbolic function identity

$$\tanh(a+b) = \frac{\tanh(a) + \tanh(b)}{1 + \tanh(a)\tanh(b)}. \qquad \text{[CH.II.3-2/2]}$$

We start here with the use of the substitution applied to the quarter-wave mirror case. In the case of a highly reflective stack all interfaces should reflect in phase with each other. This is accomplished by requiring that the index of refraction of each layer alternates between low and high values, and that the optical thickness of each layer be equal to one quarter-wavelength of the incoming light ($\theta = \pi$ for all layers) as shown in Fig. CH.II. 3-2.2.

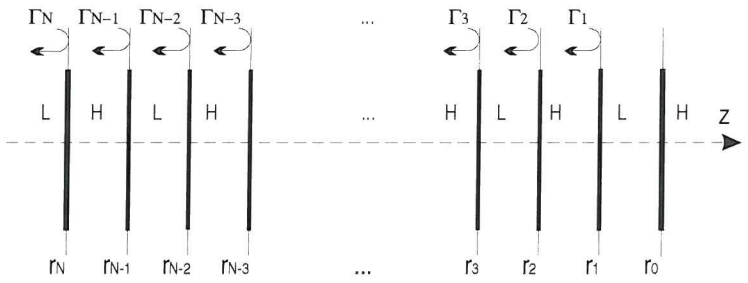


**Fig. CH.II. 3-2.2:** Schematic of a quarter-wave dielectric stack.

Comparing [CH.II.3-2/1] to [CH.II.3-2/2], we see that it would be useful to make the following variable substitution

$$|r_j| = \tanh(s_j). \qquad \text{[CH.II.3-2/3]}$$

The new variable, $s_j$, can be thought of as the reflectivity of the $j$th interface. Note that the $s_j$ are always positive numbers. Lets assume that the substrate starts off with a higher

index than the first layer as shown in Fig. CH.II.3-2.2. Then by setting $\theta = \pi$, equation [CH.II.3-2/1] becomes

$$\Gamma_1 = \frac{|r_1| + |r_0|}{1 + |r_1||r_0|} = \frac{\tanh(s_1) + \tanh(s_0)}{1 + \tanh(s_1)\tanh(s_0)} = \tanh(s_1 + s_0). \qquad \text{[CH.II.3-2/4]}$$

Replacing $r_1$ and $r_0$ in equation [CH.II.3-2/1] by $r_2$ and $\Gamma_1$, using the fact that $r_2 = -|r_2|$ and setting $\theta = \pi$, we then obtain $\Gamma_2$:

$$\Gamma_2 = -\frac{|r_2| + \Gamma_1}{1 + |r_2|\Gamma_1} = -\tanh(s_2 + s_1 + s_0). \qquad \text{[CH.II.3-2/5]}$$

Continuing this procedure to the left, we obtain the overall reflectivity $\Gamma_N$

$$\Gamma_N = (-1)^{N+1} \tanh\left(\sum_{j=0}^{N} s_j\right) = (-1)^{N+1} \tanh\left(\sum_{j=0}^{N} \tanh^{-1}|r_j|\right). \qquad \text{[CH.II.3-2/6]}$$

If we had started with a low index substrate, the final expression would be multiplied by $-1$. The alternating layers in the quarter-wave stack usually consist of two low and high refractive index materials. For this case, all of the $s_j$ within the stack are equal and [6] reduces to

$$|\Gamma_N| = \tanh[s_{top} + (N-1)s_{mirror} + s_{bot}], \qquad \text{[CH.II.3-2/7]}$$

where $s_{top}$ corresponds to the outer surface reflection, $s_{mirror}$ corresponds to the reflections within the stack, and $s_{bot}$ corresponds to the substrate reflection. Note that there are $N$+1 interfaces and $N$ quarter-wave layers. If one of the quarter-wave layers is replaced with a layer equal to a multiple of half-wavelengths, then $\theta = 2\pi m$ ($m$ is the number of half-wavelengths in the layer). Then the expression for $\Gamma_1$ [CH.II.3-2/1], assuming that the first layer is a multiple of half-wavelengths, should have the following form

$$\Gamma_1 = \frac{|r_1| - |r_0|}{1 - |r_1||r_0|} = \frac{\tanh(s_1) + \tanh(-s_0)}{1 + \tanh(s_1)\tanh(-s_0)} = \tanh(s_1 - s_0). \qquad \text{[CH.II.3-2/8]}$$

With the other layers having quarter-wave thicknesses, the form of [CH.II.3-2/5] does not change

$$\Gamma_2 = -\frac{|r_2| + \Gamma_1}{1 + |r_2|\Gamma_1} = -\tanh(s_2 + s_1 - s_0). \qquad \text{[CH.II.3-2/9]}$$

The half-wave layer inverts the sign of $s_0$ and the reflections from the zeroth interface are now out of phase with reflections from the other interfaces. If a half-wave layer is introduced into a quarter-wave stack, then all the interfaces above the half-wave layer reflect in phase with each other, similarly for all interfaces below the half-wave layer – but

these two groups of interfaces reflect out of phase with each other. Then the peak reflectivity of such structure will be

$$\Gamma_N = \tanh\left(\sum_{j=k+1}^{N} s_j - \sum_{j=0}^{k} s_j\right), \qquad \text{[CH.II.3-2/10]}$$

where

$$\sum_{j=k+1}^{N} s_j = s_{top} + (N_1 - 1)s_{mirror} + s_{cav}; \quad \sum_{j=0}^{k} s_j + (N_2 - 1)s_{mirror} + s_{bot}. \qquad \text{[CH.II.3-2/11]}$$

$N_{1,2}$ corresponds to the number of quarter-wave layers in the top and bottom quarter-wave stacks, and $s_{cav}$ is the reflectivity at the edge of the half-wave layer. If expression [CH.II.3-2/10] is made equal to [CH.II.3-2/11], then from [CH.II.3-2/9] it follows that the overall structure becomes 100% transmitting and we have what is termed a balanced Fabry-Perot cavity. Then the condition for the balanced cavity can be written as

$$s_{top} - s_{bot} = (N_2 - N_1)s_{mirror}. \qquad \text{[CH.II.3-2/12]}$$

Thus if the surface reflection is greater than the substrate reflection, the number of layers in the bottom stack should be increased, such that $N_2 > N_1$ to compensate.

## CH.II. 4. Indirect Calculation Methods for Multilayer Optical Filters

### CH.II. 4-1. *The Fourier Transform Method*

The method for the synthesis of multilayer-based optical filters described in this section is completely general and based on the use of Fourier transforms. This method does not make any assumptions about the number, thickness, or refractive indices of the individual films of the resulting multilayer. It is only necessary to specify the required spectral curve, and then the number of layers, their geometrical thicknesses, and their refractive indexes are all obtained as a result of one synthesis process by first finding an inhomogeneous layer satisfying spectral requirements and then approximating it by a series of homogeneous layers. The basic principles of the Fourier transform method were first described and published by E. Delano.[10] Then properties of FT method have been and subsequently discussed by L. Sossi.[11-13] For the purpose of this section it is sufficient to

quote without proof the essential equations of the FT method. For their derivation, the interested reader is referred to the original work.[10-17]

It has been shown that it is possible to relate the spectral transmittance of an inhomogeneous layer to its refractive index profile $n(x)$ by the following approximate expression:[12]

$$\int_{-\infty}^{\infty} \frac{dn}{dx}\frac{1}{2n}\exp(ikx)dx = Q(k)\exp[i\Phi(k)] = f(k), \qquad \text{[CH.II. 4-1/1]}$$

where $k=2\pi/\lambda$. In the above equation $Q(k)$ is a suitable even function of the desired transmittance $T(k)$ expressed as a function of the wave vector $k$. The spectral specification for synthesis with the Fourier transform method can be expressed in terms of either the complex amplitude coefficients (reflectance $r$ or transmittance $t$) or of the intensity coefficients ($R=|r^2|$ or $T=|t^2|$). The variable $x$ is twice the optical path and is defined to be

$$x = 2\int_0^z n(u)du, \qquad \text{[CH.II. 4-1/2]}$$

where $z$ is the geometrical coordinate within the layer. $\Phi(k)$ is a phase factor that must be an odd function to ensure that $n(x)$ is real. The choice of $\Phi(k)$ is arbitrary, which allows us to obtain many different solutions for the same synthesis problem by assigning different values to $\Phi(k)$. Note that $\Phi(k)$ is not the phase change on reflection or transmission. By applying a Fourier transformation to Eq. [CH.II. 4-1/1] and by integration with respect to $x$ one obtains

$$n(x) = \exp\left\{\frac{2}{\pi}\int_0^{\infty}\frac{Q(k)}{k}\sin[\Phi(k)-kx]dk\right\}. \qquad \text{[CH.II. 4-1/3]}$$

This is the refractive index profile of a non-absorbing non-dispersive inhomgeneous layer of finite extent with the desired spectral performance. Analytical integration of Eq. [CH.II. 4-1/1] is not possible for any but the simplest desired spectral transmittance curves. For most other complex cases numerical integration by computer is straightforward.

It is difficult to derive an exact expression for $Q(k)$. Although there are many ways in which the function may be defined, success is contingent on a good approximation of $Q(k)$. The most common Q-functions found in the literature are summarized in table CH.II. 4-1.

**Table. CH.II. 4-1:** Q – Functions.

| Number | Q - Function | References |
|---|---|---|
| 1. | $Q_1(k)=\sqrt{\frac{R(k)}{T(k)}}$ | 10 |
| 2. | $Q_2(k)=\sqrt{1-T(k)}$ | 16 |
| 3. | $Q_3(k)=\sqrt{\frac{1}{T(k)}-1}$ | 16 |
| 4. | $Q_4(k)=\sqrt{\frac{1}{2}\left[\frac{1}{T(k)}-T(k)\right]}$ | 15, 16 |
| 5. | $Q_5(k)=w\sqrt{1-T(k)}+(1-w)\sqrt{\frac{1}{T(k)}-1}$ | 16 |
| 6. | $Q_6(k)=\ln\left\{1+\frac{1}{4}\left(\frac{1}{T(k)}-T(k)\right)+\sqrt{\left[1+\frac{1}{4}\left(\frac{1}{T(k)}-T(k)\right)\right]^2-1}\right\}$ | 16 |

A fundamental limitation of the FT method is the approximate nature of the known $Q$ – functions. Therefore until an exact $Q$ – function is found, it is useful to have available a number of different approximate forms, and to select the most appropriate one for a particular application. The first $Q_1$ function has been used by Delano. $Q_3$ and $Q_4$ are the most commonly used functions in the literature.[10-17] $Q_2$ can be useful to form any suitable linear combination of $Q$ – functions. A new form of composite $Q_5$ function contains an additional adjustable parameter that helps to fit the target results. The additional parameter $w$ is a weight factor ($0 \le w \le 1$), which can be adjusted iteratively until the best match is obtained between the target spectral curve and the curve of the calculated layer system. $Q_6$ – function has logarithmic form and has been derived to increase the accuracy of the $Q$ – function. In principle simple approximate forms of the $Q$ – function can be found for small errors. If $|Q(k)| << 1$, it can be shown that

$$\frac{1}{T(k)}=1+|Q(k)|^2+O(Q(k)^4), \qquad \text{[CH.II. 4-1/4]}$$

and, to the same degree of approximation,

$$T(k)=1-|Q(k)|^2+O(Q(k)^4). \qquad \text{[CH.II. 4-1/5]}$$

In the above the term in $Q^4(k)$ is a crude estimate of the magnitude of the higher-order terms. It has been proved that it is possible to generate an infinite variety of acceptable $Q$ –

functions within the above degree of approximations. Any function $S(T)$ of the transmittance can be developed into a Taylor series:

$$S(T) = S(T=1) + \left(\frac{\partial S}{\partial T}\right)_{T=1}(T-1) + \frac{1}{2}\left(\frac{\partial^2 S}{\partial T^2}\right)_{T=1}(T-1)^2 + \ldots. \qquad \text{[CH.II. 4-1/6]}$$

In the above, the derivatives are evaluated for $T=1$. If now $(1-T)$ is replaced by $|Q^2(k)|$ Eq. [CH.II. 4-1/5] and if the terms in $Q^4(k)$ are neglected, it follows that

$$|Q(k)| = \sqrt{S(T(k))}. \qquad \text{[CH.II. 4-1/7]}$$

This is true provided that $S(T)$ satisfies the following conditions for $T=1$:

$$S = 0; \quad \frac{\partial S}{\partial T} = -1. \qquad \text{[CH.II. 4-1/8]}$$

In other respects the choice of $S(T)$ is arbitrary. Any function satisfying these conditions is an acceptable $Q$ – function. In particular this is also true for any suitable linear combination of $Q$ – functions.

From Eq. [CH.II. 4-1/3] follows that if the transmittance is specified in several distinct and non-overlapping spectral regions *A, B, C* ... then the refractive index profile of the combined transmittance curve is given by

$$n(x) = n_A(x) \cdot n_B(x) \cdot n_C(x)..., \qquad \text{[CH.II. 4-1/9]}$$

where $n_A(x)$, $n_B(x)$, $n_C(x)$... are the refractive index profiles corresponding to the transmission regions *A, B, C,* .... The superposition of refractive index profiles with higher frequency modulations onto the $n_A$ will result in relatively small modifications of the latter and not in major changes. It follows also from Eq. [CH.II. 4-1/9] that specifying transmittance features on the low wavenumber side of the spectral region of interest will have a significant effect on the refractive index profile. One extreme application of this is as follows. The FT method usually yields solutions in which the multilayer filter is embedded between two media of essentially the same index. One way to match such a filter into another medium is with a suitable set of antireflecting layers found with a numerical synthesis method. But it is also easy to specify a substrate in the FT method by calling for a constant transmittance at low wavenumbers. Since a thin film cannot affect the transmittance at low wavenumbers, the solution yields a semi-infinite film of the appropriate index, i.e., the substrate. It has also to be pointed out that the refractive index ratio increases and that the optical thickness of the inhomogeneous layer with significant refractive index variations decreases with increasing bandwidth of a target transmittance curve. Frequently the transmittance may be allowed to depart from unity at wavenumbers

higher than those of the spectral regions of interest. In such cases it is possible to bypass the determination of an inhomogeneous layer and to obtain the parameters of a homogeneous multilayer system with the desired spectral characteristics. Assuming that the desired spectral transmittance curve can be completely defined in the wave vector interval $0 \le k \le p$ and that the transmittance can be unity outside this range, then $p$ will be the wave vector displacement between adjacent harmonics. Then let $m$ such harmonics to be added to the original curve. By using the Fourier shift theorem[18], and by summation, it can be shown that the resulting refractive index profile will be given by

$$n(x) = \exp\left\{\frac{1}{\pi}\int_0^p Q(k)\sum_{m=0}^{m}\left[\frac{\sin[\Phi(k)-(mp+k)x]}{(mp+k)}\right]\right\}dk. \qquad \text{[CH.II. 4-1/10]}$$

This profile can be readily subdivided into a set of homogeneous layers. The desired transmission curve can also be repeated throughout the whole wave vector spectrum at intervals $p$ through the use of the Shah function (Shah is the name of the Russian letter, which is used to represent a replicating function in the Fourier theory). Using the properties of this function and the convolution theorem[18] the following expression for the refractive index profile is obtained:

$$n(x) = \exp\left[\frac{4}{p}\sum_{m=-\infty}^{\infty} F\left(\frac{m}{p}\right)\right], \qquad \text{[CH.II. 4-1/11]}$$

where $F(x)$ is the Fourier transform of $f(k)$ Eq. [CH.II. 4-1/1]. In the above expression $n(x)$ is evaluated only for values $n(x) = (m/p)$, $m = 0, \pm1, \pm2, \ldots$. For intermediate values of $x$ the refractive index $n$ has constant values.

Often the Fourier transform method results in solutions that call for refractive indices lying outside the range of values of available materials. It is important to have control over refractive index values since real materials must be used. There are several different ways of controlling the refractive index. One way is that the refractive index profile can be modified to a certain extent by suitably specifying the transmittance at wavenumbers lower than those corresponding to the spectral region of interest. Secondly, dividing the desired transmittance curve into several segments can also attain modifications of refractive index profile. Suppose that the refractive index profiles $n_A(x)$, $n_B(x)$, $n_C(x)\ldots$ yield transmittances $T_A(k)$, $T_B(k)$, $T_C(k)\ldots$, which are unity everywhere except in distinct and non-overlapping spectral regions $A$, $B$, $C\ldots$. It has been shown[19] that the combined transmittance curve $T(k) = T_A(k)\cdot T_B(k)\cdot T_C(k)\ldots$ is obtained not only with an

inhomogeneous layer having a refractive index profile given by Eq. [CH.II. 4-1/9], but also with the refractive index profile

$$n(x) = n_A(x) + n_B(x) + n_C(x) + ..., \qquad \text{[CH.II. 4-1/12]}$$

where the above summation is taken to mean that the multilayers are deposited on top of each another. The approach can be used to reduce the refractive index ratio of the profile. But the most satisfactory method of controlling the refractive index is through the control of the shape of the refractive index profile by means of the phase factor $\Phi(k)$ of the $Q$ – function. It follows from Eq. [CH.II. 4-1/3] that the refractive index profile $n(x)$, when plotted on a logarithmic scale, is symmetric or skew symmetric about the point $x = 0$ when the phase factor assumes constant values of 0 or $\pi/2$, respectively. The modulation of the refractive index profile is largest around $x = 0$ and increases with the general departure of the desired transmittance curve from unity. It is known that the envelope of the refractive index profile does not materially depend on the value of the constant phase factor. From the construction point of view, refractive index profiles with more rectangular envelopes would be very desirable. One would expect them to result in lower refractive index ratios. As was mentioned above, a more rectangular refractive index profile can be obtained if the transmittance curve is divided into segments, each with a different definition of the phase factor. Besides, if different phase factors are assigned to different parts of the transmittance curve, there will be regions in the inhomogeneous layer that are more closely associated with these parts than with others, in that way resulting in the variation in the thicknesses of the individual films of the resulting multilayer. Clearly more work is needed on the subject to realize the full potential of the FT design approach. In addition this can be attained in combination with numerical design procedures.

## CH.II. 4-2. *Optimization Methods*

An important aspect of thin film design work is the use of modern optimization algorithms to match the multilayer parameters to a set of optical specifications. In addition, optimization methods in combination with basic formulation[1-9] to the design of thin film multilayers allow specific designs with much more complex properties. These methods can be classified as either refinement or synthesis methods. Refinement methods

use a starting design that is not quite satisfactory and gradually adjust it to improve its performance. By contrast, synthesis methods frequently generate their own starting design. Usually this step is followed by refinement. Refinement methods can also be classified according to whether they optimize the quantities of interest directly, or indirectly through the use of merit functions. In this section only optimization methods that could be used for thin film optimization or have potential advantages in thin film design will be discussed in some details without entering into exhaustive mathematical discussions on the theory of the optimization procedures.

### CH.II. 4-2.1. *Adaptive Random Search*

The adaptive random search optimization method[20-21] periodically updates the magnitude of a step size to maintain the optimal rate of improvement of the merit function value of the layer system. It consists of a global and a local search that are applied alternately. The algorithm uses the merit function of a starting design, which may be a standard multilayer design. Then computation continues generating new layer systems, modifying the starting design through the use of a random construction parameter change vector, that is a random vector of unit length multiplied by the step size. First the algorithm searches for a layer system with a lower merit function within a large volume of the multidimensional construction parameter space. Computation continues by finding the most appropriate step size at that stage of the optimization process. This is achievable by evaluating the merit function of $N_{global}$ random layer systems for each of $K$ different step sizes that vary uniformly over several orders of magnitude. The local search uses the best layer system found in the global search, and the step size that yields it. The local search continues ($N_{local}>>N_{global}$) evaluating random layer systems until finds a layer system that corresponds to the local minimum of the merit function. Then using the best generated system as the starting design, the procedure is repeated until a satisfactory solution is found, or until the method stops converging.

From mathematical point of view the adaptive random search method in its simplest form could be summarized as follows. First the algorithm starts by generating $n \times m$ independent random numbers $\xi_{i,j}$ uniformly distributed in (0,1). If the multilayer system is considered as a system with periodically fixed refractive indexes, including

refractive indexes of incident medium and substrate, then problem becomes one-dimensional. Only the geometrical thickness of each layer has to be varied. At the beginning the algorithm calculates the merit function of a starting design, which can be considered at this stage as a system containing layers of equal geometrical thickness. Algorithm continues calculating $n \times m$ geometrical thicknesses using random numbers $\xi_{i,j}$:

$$d_{i,j} = a_i + (b_i - a_i)\xi_{i,j}, \qquad \text{[CH.II. 4-2.1/1]}$$

where $i = 1,...n \quad j = 1,...m$. The starting geometrical thickness range $a_i$ and $b_i$ can be considered constant but not equal. The algorithm calculates merit functions for $m$ new layer systems, arranging them in descending order of magnitude of merit function, then finds $t$ layer systems with lower merit function values. To keep computation continuous a new search region has to be created introducing new intermediate parameters:

$$\alpha_{i,t}^{\min} = \min\left\{d_i^{(1)}, d_i^{(2)}, ...d_i^{(t)}\right\}, \quad \beta_{i,t}^{\max} = \max\left\{d_i^{(1)}, d_i^{(2)}, ...d_i^{(t)}\right\}. \qquad \text{[CH.II. 4-2.1/2]}$$

Then new geometrical thickness search region is assumed to be:

$$d_{i,j}^{new} = a_{i,j}^{new} + \left(b_{i,j}^{new} - a_{i,j}^{new}\right)\xi_{i,j}^{*}, \qquad \text{[CH.II. 4-2.1/3]}$$

where,

$$\begin{aligned} a_{i,j}^{new} &= \alpha_{i,t}^{\min} - \left(\beta_{i,t}^{\max} - \alpha_{i,t}^{\min}\right)/(t-1); \\ b_{i,j}^{new} &= \beta_{i,t}^{\max} + \left(\beta_{i,t}^{\max} - \alpha_{i,t}^{\min}\right)/(t-1). \end{aligned} \qquad \text{[CH.II. 4-2.1/4]}$$

This procedure is repeated until a satisfactory solution is found or until the method stops converging.

## CH.II. 4-2.2. *Damped Least Squares Method*

The damped least-squares method[22-24] is the Gauss-Newton iteration method for solving nonlinear equations. In this method the following set of linear least-squares equations is solved[25]:

$$\delta Q = \begin{bmatrix} \delta Q_1 \\ \delta Q_2 \\ \cdot \\ \cdot \\ \cdot \\ \delta Q_m \end{bmatrix} = \begin{bmatrix} dQ_1/dp_1 & dQ_1/dp_2 & \cdot & \cdot & \cdot & dQ_1/dp_l \\ dQ_2/dp_1 & & & & & \\ \cdot & & & & & \\ \cdot & & & & & \\ \cdot & & & & & \\ dQ_m/dp_1 & \cdot & \cdot & \cdot & \cdot & dQ_m/dp_l \end{bmatrix} \begin{bmatrix} \delta p_1 \\ \delta p_2 \\ \cdot \\ \cdot \\ \cdot \\ \delta p_l \end{bmatrix}. \qquad \text{[CH.II. 4-2.2/1]}$$

The vector $\delta Q$ contains the desired changes $\delta Q_i$ in the $m$ quantities of interest, where on the right side is an $m \times l$ matrix composed of derivatives of the quantities with respect to the construction parameters, multiplying a column vector containing the required changes of the construction parameters $\delta p_j$. The solution of the above equation minimizes the quantity:

$$\left( \begin{bmatrix} \delta Q_1 \\ \delta Q_2 \\ \cdot \\ \cdot \\ \cdot \\ \delta Q_m \end{bmatrix} - \begin{bmatrix} dQ_1/dp_1 & dQ_1/dp_2 & \cdot & \cdot & \cdot & dQ_1/dp_l \\ dQ_2/dp_1 & & & & & \\ \cdot & & & & & \\ \cdot & & & & & \\ \cdot & & & & & \\ dQ_m/dp_1 & \cdot & \cdot & \cdot & \cdot & dQ_m/dp_l \end{bmatrix} \begin{bmatrix} \delta p_1 \\ \delta p_2 \\ \cdot \\ \cdot \\ \cdot \\ \delta p_l \end{bmatrix} \right)^2. \qquad \text{[CH.II. 4-2.2/2]}$$

It is necessary to ensure that the derivatives used in the calculations remain valid. For this reason major changes in the quantities of interest must be brought about gradually, by the repeated application of the solution routine. It is further necessary to ensure that the changes in the construction parameters be small at all times. This is done in the damped least-squares method by adding the following equations to [CH.II. 4-2.2/2]:

$$0 = \begin{bmatrix} B_{1,1} & 0 & \cdot & \cdot & \cdot & 0 \\ 0 & B_{2,2} & \cdot & \cdot & \cdot & 0 \\ \cdot & \cdot & \cdot & \cdot & \cdot & \cdot \\ \cdot & \cdot & \cdot & \cdot & \cdot & \cdot \\ \cdot & \cdot & \cdot & \cdot & \cdot & \cdot \\ 0 & \cdot & \cdot & \cdot & \cdot & B_{l,l} \end{bmatrix} \begin{bmatrix} \delta p_1 \\ \delta p_2 \\ \cdot \\ \cdot \\ \cdot \\ \delta p_l \end{bmatrix}. \qquad \text{[CH.II. 4-2.2/3]}$$

The elements $B_{j,j}$ are special damping constants. The starting values of the damping constants for thicknesses and refractive indices can be obtained using:

$$B_t = \left[\sum_{i=1}^{m}(\delta Q_i)^2\right]^{1/2} \Big/ (4/\Delta t); \qquad B_n = \left[\sum_{i=1}^{m}(\delta Q_i)^2\right]^{1/2} \Big/ (4/\Delta n)\ . \qquad \text{[CH.II. 4-2.2/4]}$$

The terms $\Delta t$ and $\Delta n$ are the maximum allowed changes in the thicknesses and refractive indices. The combination of Eq. [CH.II. 4-2.2/2] and Eq. [CH.II. 4-2.2/3] is solved simultaneously minimizing the quantity Eq. [CH.II. 4-2.2/5]:

$$\left(\begin{bmatrix}\delta Q_1\\ \delta Q_2\\ .\\ .\\ .\\ \delta Q_m\end{bmatrix} - \left(\begin{bmatrix} dQ_1/dp_1 & dQ_1/dp_2 & . & . & . & dQ_1/dp_l\\ dQ_2/dp_1 & & & & & \\ . & & & & & \\ . & & & & & \\ . & & & & & \\ dQ_m/dp_1 & . & . & . & . & dQ_m/dp_l\end{bmatrix} + \begin{bmatrix} B_{1,1} & 0 & . & . & 0\\ 0 & B_{2,2} & . & . & 0\\ . & . & . & . & .\\ . & . & . & . & .\\ . & . & . & . & .\\ 0 & 0 & . & . & B_{l,l}\end{bmatrix}^2\right)\begin{bmatrix}\delta p_1\\ \delta p_2\\ .\\ .\\ .\\ \delta p_l\end{bmatrix}\right)^2$$

The advantage of this is that the construction parameters now can be controlled. The equations can be solved using Crout's method[26]. The advantage of this method is that only part of the computation needs to be repeated. The damped least-squares optimization algorithm can be formed in the following order. Each iteration starts with the evaluation of a new set of derivatives. The equations are solved and the resulting system is examined to see if any of the construction parameters lie outside the permitted bounds. If so, they are set equal to the boundary values and the merit function of the resulting system is evaluated. Should the merit function have a lower value than that of the starting design, the algorithm proceeds to the next iteration. If not, the desired change vector $\delta Q$ is reduced, the damping constants $B_{j,j}$ of the parameters that went out of bounds are increased, and the equations are resolved. This procedure can be repeated until $\delta Q$ is 1% of it's original value. If the merit function is still greater than that of original system, $\delta Q$ is restored to its original value and the above calculations are repeated with larger values of all the damping constants $B_{j,j}$. The disadvantage of the damped least-squares optimization algorithm is the calculation of the derivatives. The calculation of the derivatives is the most time consuming part of the algorithm.

## CH.II. 4-2.3. *Modified Gradient Method*

There are number of methods for reducing a merit function by determining the gradient of the function at a given point and following the gradient down until a minimum is reached. The gradient algorithm calculates first derivatives to determine the gradient direction, then evaluates the merit function at several points along the gradient to find approximate minimum before determining a new gradient direction. Gradient algorithms such as described above in many cases converge to a solution more slowly than the damped least-squares method, but they have certain advantages. Two of the most important are the following: 1) The number of target points to be fit can be less than the number of variables. 2) Gradient methods allow considerable freedom in the choice of the merit function whereas the damped least-squares method requires, by definition, a least squares merit function. In the modified gradient method, the derivatives of the merit function are calculated numerically with respect to all construction parameters.[26] A construction parameter vector is determined representing the gradient direction $dM/dp$. Then, by trial an error, a step $s$ along this direction is found which leads to the greatest improvement in the merit function. The new construction parameter vector is given by the equation:

$$p = p_0 - sdM/dp, \qquad \text{[CH.II. 4-2.3/1]}$$

where $p_0$ is the original construction parameter vector. This procedure is repeated until no further improvements are made. The modified gradient method does not use the vector direction, but rather calculates the optimum changes $\delta p_j$ for the individual parameters $p_j$, assuming a parabolic dependence of the merit function on the parameters. Then quantities $dM/dp_j$, $d^2M/dp_j^2$ are calculated numerically, and from them quantities $\delta p_j$ for $j = 1,2...l$:

$$\delta p_j = -\frac{dM/dp_j}{d^2M/dp_j^2}. \qquad \text{[CH.II. 4-2.3/2]}$$

At this stage it is possible to reduce any parameter change that appears to be unreasonably large, and that would, therefore, lead to a strong nonlinear behavior of the solution process. Together they form a parameter change vector $\Delta p$. Merit functions

$$M = M(p + k\Delta p) \qquad \text{[CH.II. 4-2.3/3]}$$

are evaluated for $k = 1,1/2,1/4,...$ until, together with the merit function for $k = 0$, five values are found that are suitable for the parabolic interpolation of the value $k'$ that results in the optimum value of merit function. The whole process is repeated as long as a reasonable convergence is maintained.

## CH.II. 4-2.4. *Golden Selection Method*

In the golden section method[27-28] the parameters of a layer system are varied sequentially and quite large changes can be made. It is therefore possible for the solution to shift into the vicinity of a different, lower minimum. Let us assume that there is only parameter $p$ to be varied and there is one minimum of the merit function $M$ in the search region ($p_{min}$, $p_{max}$). The algorithm first evaluates the merit functions $M_{min}$, $M_{max}$, and $M_1$, $M_2$ for the values of the parameters $p$ equal to $p_{min}$, $p_{max}$. Then two specially spaced values $p_1$, $p_2$, given by:

$$p_1 = p_{min} + 0.382(p_{max} - p_{min}), \qquad p_2 = p_{min} + 0.618(p_{max} - p_{min}). \qquad \text{[CH.II. 4-2.4/1]}$$

The algorithm requires proper definition of the new search range. These are summarized in table CH.II. 4-2.4. 1.:

**Table CH.II. 4-2.4. 1:** Conditional search ranges.

| Nr. | Merit function inequalities | New search range |
|---|---|---|
| 1. | $M_2 > M_1$ | $(p_{min}, p_2)$ |
| 2. | $M_2 < M_1$ | $(p_1, p_{max})$ |
| 2. | $M_{max} < M_{min} < M_2$ | $(p_1, p_{max})$ |
| 3. | $M_{max} < M_2$ & $M_{min} < M_{max}$ | $(p_{min}, p_2)$ |

The golden section method converges to a solution quite rapidly. Because of the special choice of the parameter values $p_1$, $p_2$, only one merit function evaluation is needed for each further reduction of the search range by a factor of 0.618.

### CH.II. 4-2.5. *Hooke and Jeeves Pattern Search Method*

The Hooke and Jeeves pattern search method[29-30] consists only of two components, an exploration and a pattern move. The merit function is first evaluated for the starting design. Reasonable exploration step sizes for the thicknesses and refractive indices are then assigned. Next an exploration is executed in which one construction parameter at a time is adjusted by the appropriate step. If either of these operations succeeds in reducing the merit function, this new value and the corresponding value of the construction parameter are retained. The exploration is complete when all the parameters have been tested in this way. If the merit function has been reduced by this procedure, the resulting system becomes the new base system. In the pattern move that follows, all the construction parameters are extrapolated linearly in a single step in the direction defined by the new and old base systems. The sequence of explorations and pattern moves is then repeated with increasing step sizes as long as the merit function continues to be reduced. If the merit function is increasing then the step sizes are halved. The algorithm continues until the step sizes are reduced below a certain predefined limit.

### CH.II. 4-2.6. *Basic Powell Conjugate Search Method*

The Powell conjugate search method[31] is a direct search method that generates a set of conjugate search vectors that allows the merit function to converge efficiently to a minimum. The algorithm begins with a starting layer system and a set of search vectors which initially point along the coordinate directions. During an iteration a line search is made along each vector using Powell's quadratic interpolation routine to find a layer system with lower merit function values. After the searches have been made, a new vector is calculated that joins the initial and final layer systems of that iteration. For a system with $n$ parameters, this vector becomes the $n$th search vector for a next iteration and the first search vector is eliminated. A search is made using this new vector to complete an iteration. After $n$ iterations all the initial search vectors have been replaced with a set of conjugate search vectors. These should cause the rate of convergence to improve, but it is

possible that the set of vectors may become linearly dependent. In this case, only a subspace of the parameter space is searched. This can be obtained by resetting the search vectors to the coordinate directions if no improvement of the merit function is made during an iteration.

### CH.II. 4-2.7. *Rosenbrock's Rotating Coordinates Search Method*

In the Rosenbrock rotating coordinates search method[32] reasonable initial step sizes for the incrementation of the construction parameters must be provided. During the first stage of the algorithm, each parameter in turn is incremented by its appropriate step. If this leads to a decrease in the merit function, the step size is multiplied by a positive factor that is greater than one. If not, a negative factor in the range (-1,0) is used. This incrementation of the construction parameters is repeated until the change in every parameter has at least once succeeded and at least once failed to improve the value of the merit function. During the second stage of the algorithm, the Gramm-Schmidt orthonormalization[33] is used to generate a new set of vectors that are orthonormal to the direction of greatest improvement of the merit function obtained in the first stage. Then this new set of vectors is used in another round of increments of the construction parameters of the layer system. The above two stages are repeated until a satisfactory solution is found or until the rate of convergence becomes unacceptable.

### CH.II. 4-2.8. *Generalized Simulated Annealing Method*

The generalized simulated annealing method[34-35] is used for the solution of global minimization problems with a very large number of variables. In this method step sizes for changes in index and thickness have to be specified. The merit function $M_1$ of the starting design is evaluated and small random changes are made in all the construction parameters by multiplying the step sizes by random unit vectors. The merit function $M_2$ of the new system is evaluated and the probability $P$ of it replacing the previous system is given by:

$$\begin{aligned} P &= 1 && when \quad M_2 < M_1, \\ P &= \exp\left[\beta(M_1 - M_2)/M_1^g\right] && when \quad M_2 > M_1. \end{aligned} \qquad \text{[CH.II. 4-2.8/1]}$$

The new parameters $\beta$ and $g$ are constants that are greater than zero. The constant $\beta$ governs the percentage of systems with worse performance that are accepted. The term $M_1^g$ ensures that it is more difficult for the minimization procedure to go away from a low minimum. For a value of $g = 0$ the algorithm reduces to the standard simulated annealing procedure. It has been recommended that a value of $\beta$ be selected such that 50-90% of the detrimental changes are approved. The value of $\beta$ has to be updated each time after 50-90% of systems with higher merit functions were accepted.

## CH.II. 4-2.9. *Merit Functions (MF)*

The problem in numerical design of optical multilayer filters is to find the construction parameters of the system satisfying the desired specifications. The performance of the multilayer at any stage of the design is measured by the value of a merit function MF. This is a single-valued function that can be defined in terms of various quantities of interest that can be evaluated for the multilayer system. The most commonly specified quantities are the transmittance or reflectance for a given wavelength, angle of incidence, and plane of polarization. In general merit functions can be defined for very specific calculation methods. The most frequently used merit functions are listed in table CH.II. 4-2.9. 1.

**Table CH.II. 4-2.9. 1:** Merit Functions.

| Nr. | Merit function | References |
|---|---|---|
| 1. | $MF = \left[ \sum_{i=1}^{m} q_i \left\| f_i^T - f_i \right\|^k \right]^{1/k}$ | 24 |
| 2. | $MF = \sum_{i=1}^{m} q_i \left( f_i^T - f_i \right)^2$ | 24 |
| 3. | $MF = \left[ \frac{1}{m} \sum_{i=1}^{m} \left( \frac{f_i^T - f_i}{1/q_i} \right)^2 \right]^{1/2}$ | 15 |
| 4. | $MF = \frac{1}{m} \sum_{i=1}^{m} \left( \frac{f_i^T - f_i}{1/q_i} \right)^2$ | 15 |

Typical terms used in table CH.II. 4-2.9. 1, $f_i^T$, $f_i$, $q_i$ are, respectively, the target, present values, and the relative weight on the *i*th of the *m* quantities of interest making up the merit function. Typically the inverse value of the weight factor is called the tolerance at the *i*th wavelength. The tolerance can be kept within practical and necessary limits or in principle be included in optimization by suitable choice of weight factors at the *i*th wavelength for each iterative procedure. This is an additional possibility to control optimization processes over specific spectral regions. By the way this can also be included and used with different algorithms and with different merit functions. The parameter $k$ is an integer. The case $k = 2$ is the least squares fit, and it is the only merit function that can be used with damped least squares unless one is willing to go to extraordinary effort in defining the individual functions and their derivatives that make up the merit function. The case $k = 1$ is the merit function used in linear programming. The merit function Nr. 2 in table CH.II. 4-2.9. 1. can be used with gradient algorithms and is often referred to as the quadratic merit function. In the case of a very large number of sampling points, it is advantageous to normalize merit function to this number.

## CH.II. 4-2.10. *Numerical Optimization Method*

The main focus of this section is to describe the principal idea and general numerical optimization algorithm used in this work for the design of diode pumped vertical cavity surface emitting lasers and similar type devices. In general these devices have multi-sectional character with specific peculiarities. Therefore it is necessary to emphasize that the desired specifications have to be defined for each structural element of the device, because the general characteristic of the device is initially unknown, or is too difficult to define. The more complex device the more specific design and optimization algorithm is required. There is no one algorithm that has all required capabilities. The algorithm can be only as flexible as possible for required application. For example, the FT method is limited to non-absorbing and non-dispersive materials. Gradient algorithms converge on the solution more slowly than damped least squares in many cases, but allow considerable freedom in the choice of the merit function whereas damped least squares require a least-squares merit function and a lot more computation resources. Other methods including the adaptive random search optimization method, the Hooke and Jeeves pattern search method, the Powell conjugate search method, the Rosenbrock rotating coordinates search method may not sufficient sensitive to the changes that would bring the design closer to the target. Lower sensitivity of merit function may degrade the whole optimization procedure. Attempt to apply the adaptive random search optimization method to the design of diode pumped vertical cavity surface emitting lasers was unsuccessful. The main problems were associated with low refractive index contrast and merit function sensitivity variations. Therefore two algorithms that supplement each other have been developed for the design of saturable absorber mirrors and diode pumped vertical cavity surface emitting lasers.

The first algorithm used in this work is entirely numerical including global and local calculation procedures. Global procedures are related more to the formation of the entire device structure and are carried out left to right, entering already optimized device sections one after another. The local procedures are connected with individual layer and each structural element optimization. The algorithm is discussed with the aid of the schematic block diagram shown in Fig. CH.II. 4-2.10. 1. The algorithm can be assumed to

be two-part excluding calculation and optimization sections. It starts by simultaneously entering mandatory material data and optimization parameters.

- Typical mandatory parameters are the spectral region of interest, refractive indices of high and low refractive index materials defined for each structural element, optical thickness limits including maximum achievable optical thickness of individual layer, maximum optical thickness of structural element, minimum increment of metric thickness, angle of incidence.

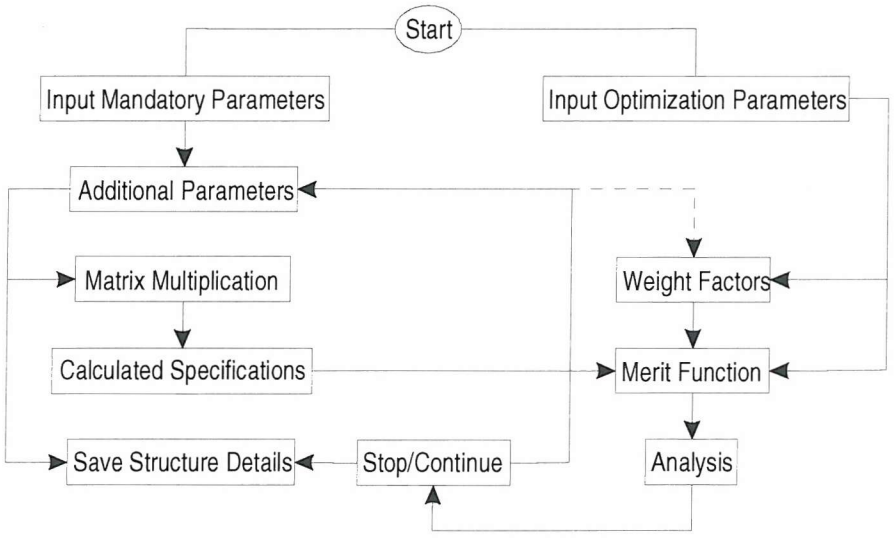


**Fig. CH.II. 4-2.10. 1:** General program diagram.

- Typical optimization parameters are desired spectral characteristics, weight factors and their limits. It is recommended to define weight factor as a parameter-dependent function, whose value can be controlled during the local optimization cycle. This helps to control conditions of convergence.
- In the next step additional parameters are constructed. These form a logic branch parameter system and provide the necessary background for iteration procedures to be completed.
- Calculations are then carried out using matrix multiplications. They done in two different ways for the entire device, and for local optimization of each structural element. An individual structural element is formed by increasing optical thickness

from the centre on both sides. A layer of high refractive index material with metric thickness of increment value is set in the structural element centre. Then calculations start increasing the geometric thickness of the layer with low refractive index material and continue until defined limits are reached. This repeats on other side after the optimum value of metric thickness has been found and inserted as a optimum on the previous side. Calculations are then continued by turns on both sides but with high refractive index material. This repeats by turns on the left hand side then on the right or other way round alternatively changing refractive index until multilayer system of structural element satisfying desired specifications is formed. It is evident that calculation and optimization procedures are closely connected. Calculations are carried out in the second cycle designing the next structural element if, and only if, desired requirements are met in previous one. The only difference is now that structural elements are placed from the left hand site to the right.

- Analysis proceeds by optimizing either amplitude-frequency or phase-frequency characteristics, searching for the optimal metric thickness of each individual layer. The algorithm stops if final multilayer system satisfies desired specifications or any structural element has been not optimized. In this case it is convenient to add into calculations parameter-dependent weight factors and to repeat calculations. Another option is to change input data limits. It could happen that satisfactory a solution is still not achievable. Then desired specifications should be pre-defined and calculations repeated.

The step-like numerical algorithm helps to focus on the design of each structural element if necessary and even to use different calculation methods. Typically the more complex desired specifications the more complicated design procedure. Very often designed multilayer systems satisfying desired specifications do not satisfy practical limits or fabrication requirements. Therefore only a few selected designs are used in high volume production. This computation program has mainly been used with low-contrast semiconductor materials but it can also be applied to a much wider range of problems. For the design of AR coatings, a subsidiary program has been written using the Fourier synthesis method. In general this method can be used only with non-dispersive and non-absorptive materials, due to the difficulties of using the complex Fourier integral. In principle the algorithm follows characteristic features of typical programs written for the

Fourier synthesis of optical multilayer AR coatings but differs in some details. A brief explanation of a possible flow of calculations is discussed below with the aid of the schematic block diagram of Fig. CH.II. 4-2.10. 2.

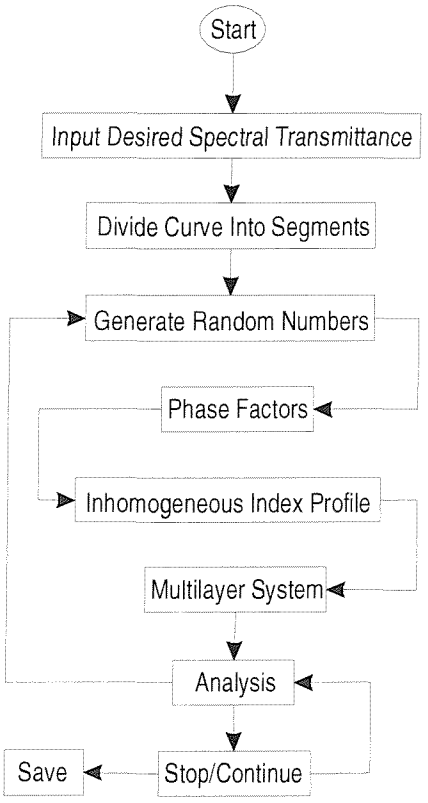


**Fig. CH.II. 4-2.10. 2:** Block diagram of the flow of calculations.

- First of all the desired spectral transmittance curve is entered, dividing it into a preliminary defined number of $N$ small segments.
- The next step is to choose a proper $Q$–function from available list. The function $Q_4$ appears to yield better synthesis results and was therefore chosen for the starting design. Other available $Q$–functions can also be selected and used.
- Then phase factors for each segment are defined using a random search approach. First of all the computer generates $m$ random numbers $\xi_m$ in the interval (-1, 1) for each segment independently, in that way creating a 2D random number space. Then these random numbers are used to form 2D random phase space

$\phi_{N,m} = \phi^{\min} + (\phi^{\max} - \phi^{\min})\xi_{N,m}$ (where $\phi^{\min}$, $\phi^{\max}$ are phase factors arbitrarily set at the beginning).

- Next, the refractive index profile $n(x)$ of an inhomogeneous layer is evaluated $m$ times, each time applying random phase factors for whole number of segments. Each inhomogeneous layer is transformed into a multilayer system of homogeneous layers. Then a program search for the minimum and maximum values of the refractive index in the multilayer system calculates the difference. This procedure is repeated until each multilayer system is analyzed. Then phase factors corresponding to a minimum and maximum refractive index value are evaluated for each segment. To keep computation continuous, and to form an iterative procedure, these new phase factors are automatically used as new $\phi_N{}^{\min}$, $\phi_N{}^{\max}$. Note that this time $\phi_N{}^{\min}$ and $\phi_N{}^{\max}$ are different for each segment. The procedure continues and phase factors are continuously renewed until a multilayer system with the minimum value of refractive index difference is found.
- The multilayer system consisting of a number of homogeneous layers and with the smallest refractive index ratio is considered to be the final solution.

The main difficulty in using this method is the large number of calculations needed. It can be seen that the above algorithm model is searching for a design with a minimum refractive index ratio corresponding to the practical limits. This is very useful for a real material system with a small available refractive index ratio. If the refractive indices still lie outside the practical limits, the transmittance curve outside the desired region can be modified also using a statistical search approach. Very specific designs then can be generated for a material system with a small refractive index ratio. A shortcoming of the Fourier synthesis method is always the solution that gives slightly deviant result. This always has to be corrected using additional computation procedures including dispersive and absorptive material properties. It is evident that both developed computation methods supplement each other. Therefore it is always useful to know more than one design method in order to achieve novel and specific results.

## CH.II. 5. Small Inhomogeneities in Thin Layers

Inhomogeneous layers can be both useful and a source of problems in multilayer-based optical systems. It is well known that the spectral characteristics of an individual layer can be influenced by even small inhomogeneities or variations in its complex-index profile.[36] In addition we always can expect small variations in geometrical thickness and material alloy composition, roughness effects. For example, an inhomogeneous layer whose refractive index varies smoothly from that of the substrate to that of the embient medium makes a good broadband antireflection coating. In any other instances, however, multilayers composed of homogeneous layers are optimal solutions to a design problem. In these cases inhomogeneities in individual layers can result in a degradation of the performance and can make accurate thickness control, based on optical monitoring, more difficult. It has been observed that it is quite difficult to predict whether spectral characteristics are affected by a small refractive-index or extinction coefficient inhomogeneity. Proper choice of technology and optimum manufacture conditions make it possible to grow even relatively thick homogeneous layers. However, for various reasons it is impossible to avoid layer microstructure that results is small variations in the refractive index profile at the beginning or at the end of the layer. Therefore it is advisable to check-up performance characteristics of any designed multilayer system including edge-type inhomogeneities. It is not very difficult to do.

## CH.II. 6. Unintentional Random Disorder in Multilayers

A certain amount of unintentional random disorder is always introduced in the semiconductor multilayer heterostructure growth process and this fact is well established to have influence on the characteristic properties of semiconductor heterostructures.[37] In the case of heterostructures consisting of very thin and even unequal optical thickness layers, a small amount of unintentional random variations in layer thickness could be particularly critical. Unintentional disorder can be classified into two categories: lateral and vertical. Vertical disorder occurs whenever the layer thickness or the mole fraction of

chemical species forming the alloy fluctuates around their nominal values. Lateral disorder occurs whenever adjacent semiconductor layers form chemically intermixed interfaces, steps and islands. This kind of disorder yields a rough interface where transitional symmetry in the plane perpendicular to the growth direction is broken. Both kinds of disorder take place in the growth process. A statistical approach is introduced below to account for random disorder effects. First of all, vertical disorder is considered. The model allows the optical thickness values of any two adjacent layers to be replaced with slightly deviant that fluctuate around their nominal values by using following parameters:

$$\begin{cases} p_{n,m} = 1 + \Delta\xi_m \\ p_{n+1,m} = 1 - \Delta\xi_m \end{cases}, \qquad \text{[CH.II. 6/1]}$$

where $\Delta$ is a positive disorder weight parameter which measures the maximum fluctuation while the $\xi_m$ are uncorrelated random numbers in the range (0,1). The new values of layer thickness then are:

$$\begin{cases} h_{n,m}^{new} = h_{n,m}^{old} p_{n,m} \\ h_{n+1,m}^{new} = h_{n+1,m}^{old} p_{n+1,m} \end{cases}, \qquad \text{[CH.II. 6/2]}$$

The same procedure can be used to change both refractive index and metric layer thickness, while the optical thicknesses of the two adjacent layers remain unchanged. Lateral disorder can be estimated easily, neglecting for the time being any vertical disorder. It means that for any sample the thickness of each individual layer can change in the transverse plane but its average coincides with the nominal one. It is quite difficult to make a prediction in a general case of lateral disorder since the problem is entirely three dimensional. It is possible to simplify the problem if the transversal average sampling dimension is not particularly small. The multilayer must be divided into $N$ elements of relatively small transversal dimension, where it is assumed that any characteristics of each element can be considered as transversally uniform. Any characteristics of a specific laterally disordered multilayer is then:

$$f_L = \frac{1}{N}\sum_{i=1}^{N} f_i \ , \qquad \text{[CH.II. 6/3]}$$

where $f_i$ is the characteristics of $i$th element. It allows us to characterize the distribution of the characteristics of the laterally disordered multilayers through its average and its standard deviation.

## CH.II. 7. Numerical Results

In this section only the most successful structure designs are summarized that achieved by using indirect design methods. These can be used either as final design or as starting design for further optimization if necessary. Using indirect design algorithms it has been established that the desired specifications of the entire device can be achieved optimizing only one structural element of the device (for example AR region), while keeping the entire device as simple as possible. It is the most straightforward way to achieve final design that is much more technologically simple and meets all manufacturing demands. Therefore a lot of attention has been paid to design AR coatings. All designs could be divided into three groups: single-band AR coatings, single-broadband AR coatings, and two-band AR coatings. These could be useful optimizing the performance of semiconductor devices such as DP-VECSEL's and saturable absorber mirrors. Results obtained including material dispersion of semiconductors used.

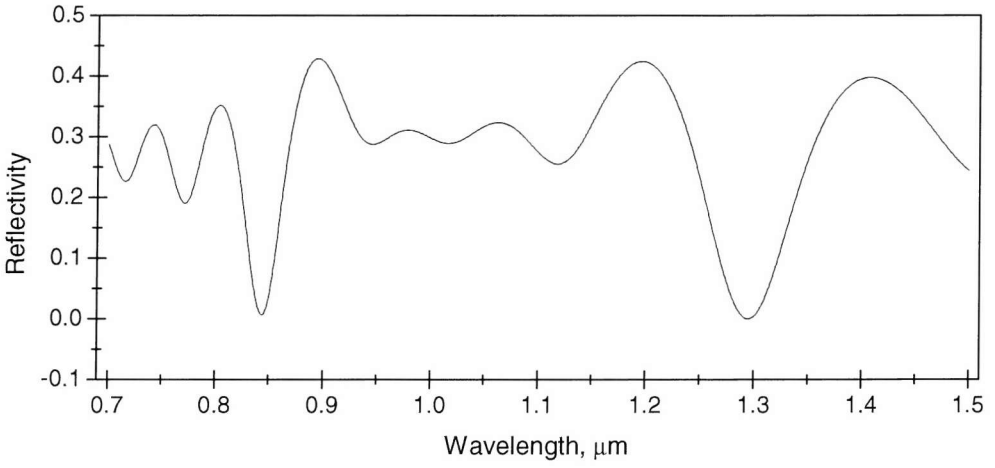


**Fig. CH.II. 7. 1.** Computed reflectivity of two-band antireflection coating as a function of wavelength. Structure formula: 7S □ 3.866L 1.127H 3.866L 1.127H 3.866L 1.127H 3.866L □ 1.0; ($\lambda_0 = 1.03$ μm, $n_L(AlAs) = 2.94$, $n_H(Al_{0.1}Ga_{0.9}As) = 3.43$, $n_S(GaAs) = 3.496$). This seven layer two-band AR coating design particularly useful for DP-VECSEL that is pumped at 0.83 μm and emitting 1.3 μm.

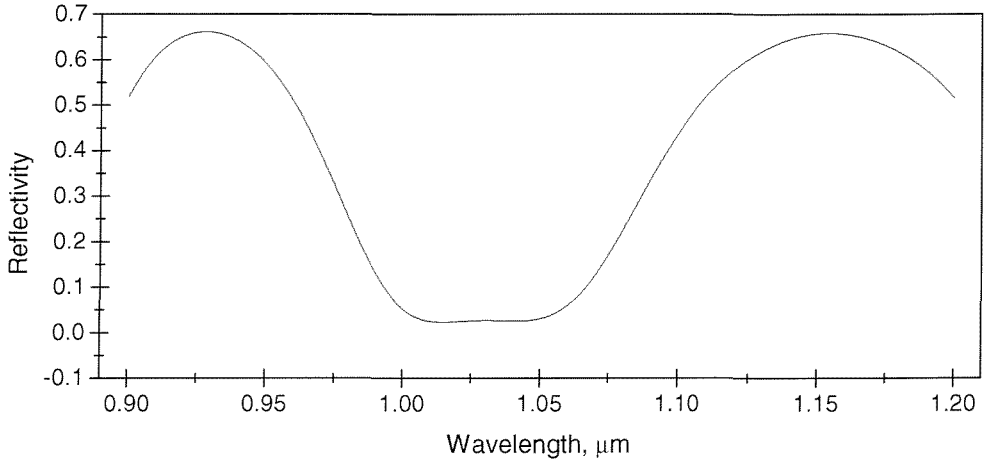


**Fig. CH.II. 7. 2.** Computed reflectivity of broad-band antireflection coating as a function of wavelength. Structure formula: 12S □ L H 4L H $[LH]^2$ 3L H L 2H □ 1.0; ($\lambda_0 = 1.03$ μm, $n_L(AlAs) = 2.94$, $n_H(Al_{0.1}Ga_{0.9}As) = 3.43$, $n_S(GaAs) = 3.496$). This particular design is applicable to a semiconductor device that requires flat AR coating in the spectral region exceeding ~30 nm.

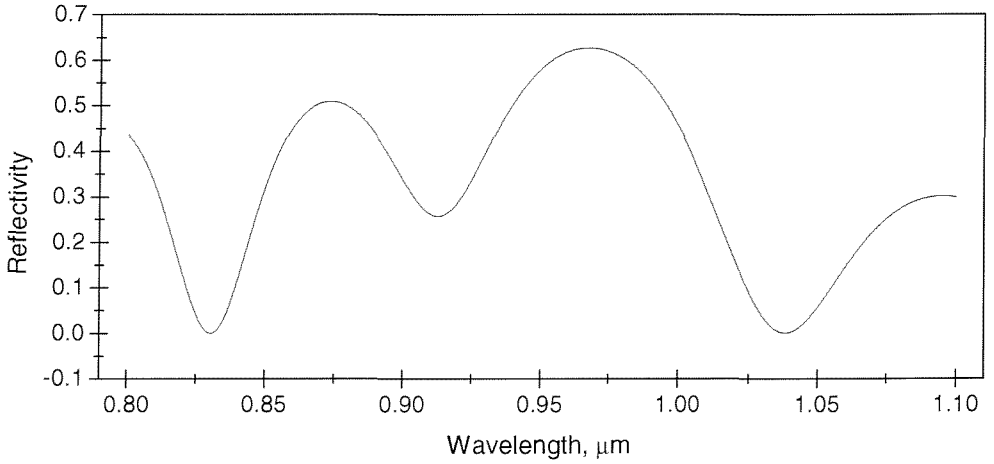


**Fig. CH.II. 7. 3.** Computed reflectivity of two-band antireflection coating as a function of wavelength. Structure formula: 12S □ 0.915L 0.52H 1.372L 0.52H 5.488L 0.52H 1.372L 0.52H 1.372L 0.52H 5.351L 0.136H □ 1.0; ($\lambda_0 = 1.03$ μm, $n_L(AlAs) = 2.94$, $n_H(Al_{0.1}Ga_{0.9}As) = 3.43$, $n_S(GaAs) = 3.496$). This particular design of two-band antireflection coating is useful for DP-VECSEL that could be pumped at 0.83 μm and could lase near 1.03 μm.

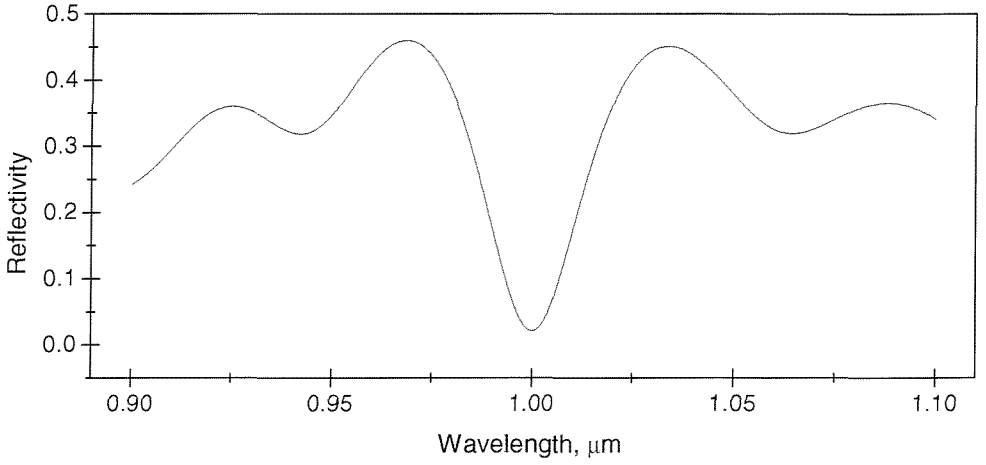


**Fig. CH.II. 7. 4.** Computed reflectivity of single-band antireflection coating as a function of wavelength. Structure formula: 7S □ 8.735L 2.906H 8.735L 2.906H 2.915L 5.826H 5.831L □ 1.0; ($\lambda_0 = 1.03$ μm, $n_L(AlAs) = 2.94$, $n_H(Al_{0.1}Ga_{0.9}As) = 3.43$, $n_S(GaAs) = 3.496$). This particular design achieved using triangle-shaped desired transmission function centered at 1 μm. It could be useful for an applications were symmetric AR coating is required.

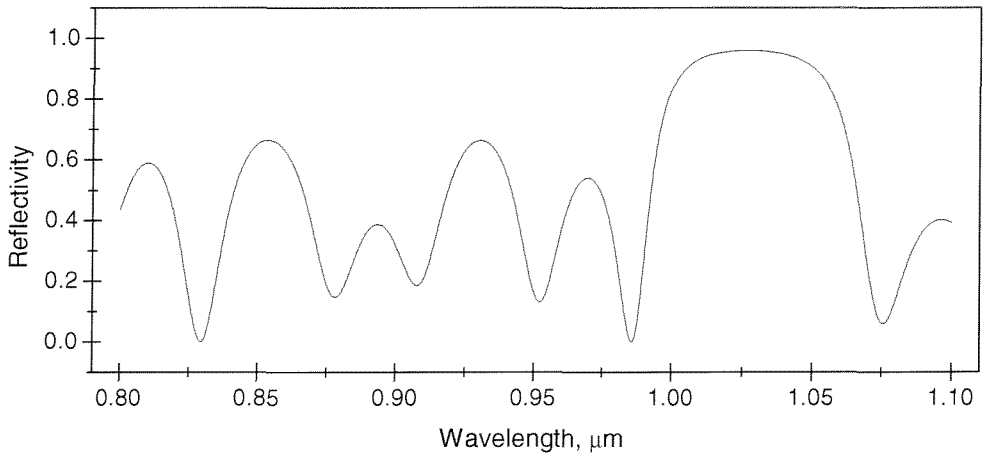


**Fig. CH.II. 7. 5.** Computed reflectivity of single-band antireflection coating and mirror as a function of wavelength. Structure formula: 22S □ 4.615L 1.012H [0.986L 1.012H]$^2$ 4.93L 1.012H 0.986L 1.012H 5.009L 1.012H [0.986L 1.012H]$^2$ 4.93L 1.012H 5.009L 3.036H 2.998L 0.984H □ 1.0; ($\lambda_0 = 1.03$ μm, $n_L(AlAs) = 2.94$, $n_H(Al_{0.1}Ga_{0.9}As) = 3.43$, $n_S(GaAs) = 3.496$). This structure is applicable to DP-VECSEL that requires top mirror with narrow AR coating region for an optical pumping.

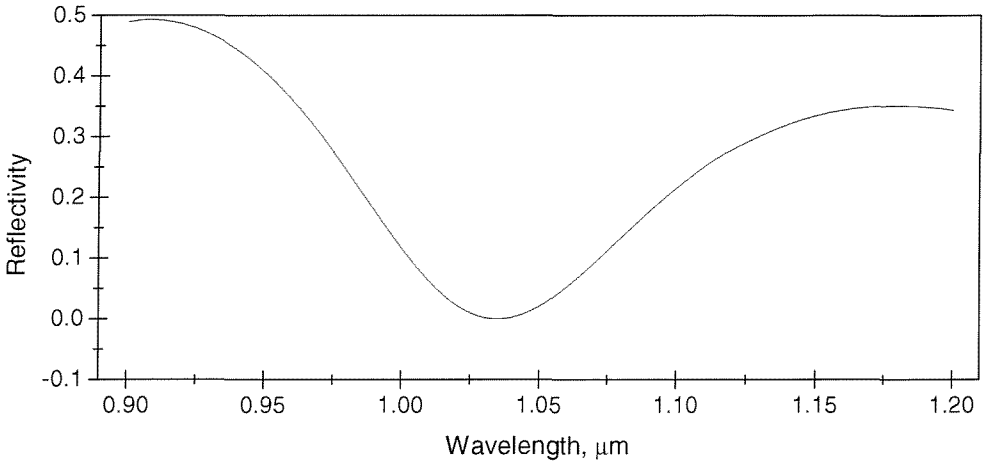


**Fig. CH.II. 7. 6.** Computed reflectivity of single-band antireflection coating as a function of wavelength. Structure formula: 10S □ 0.98L 0.975H 0.98L 1.588H 0.299L 1.588H 0.98L 0.975H 0.908L 0.298H □ 1.0; ($\lambda_0 = 1.03$ μm, $n_L(AlAs) = 2.94$, $n_H(Al_{0.1}Ga_{0.9}As) = 3.43$, $n_S(GaAs) = 3.496$). This particular design achieved using triangle-shaped wide-angle desired transmission function centered at 1.04 μm. It shows asymmetry and has ten layers.

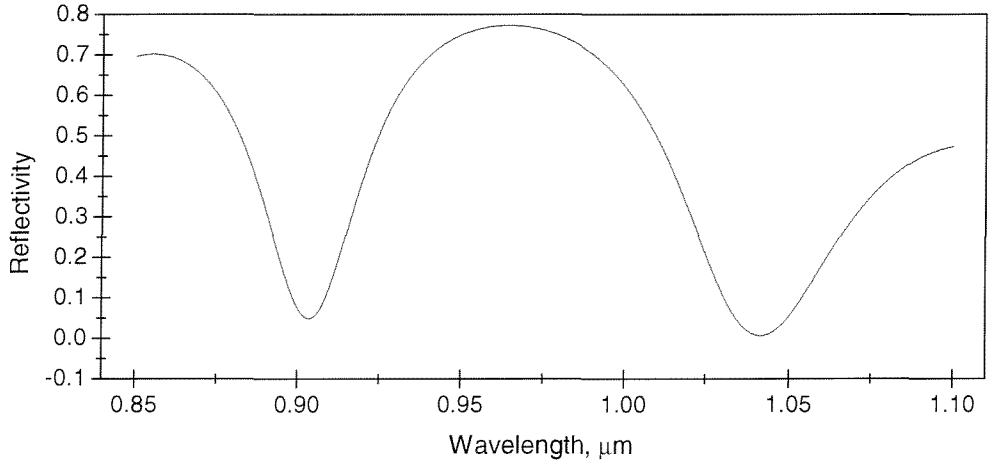


**Fig. CH.II. 7. 7.** Computed reflectivity of two-band antireflection coating as a function of wavelength. Structure formula: 20S □ 0.368L [1.023H 1.031L]$^4$ 0.061H 0.059L 0.061H 2.051L 2.06H 2.051L 1.272H 0.368L 1.272H 1.209L 0.422H □ 1.0; ($\lambda_0 = 1.03$ μm, $n_L(AlAs) = 2.94$, $n_H(Al_{0.1}Ga_{0.9}As) = 3.43$, $n_S(GaAs) = 3.496$). This design could be used for DP-VECSEL that is optically pumped at 0.908 μm and is lasing near 1.04 μm.

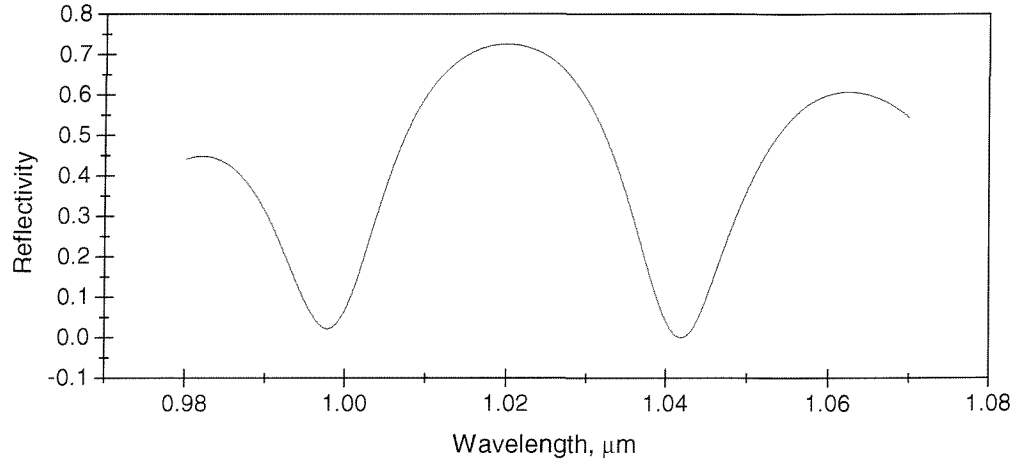


**Fig. CH.II. 7. 8.** Computed reflectivity of two-band antireflection coating as a function of wavelength. Structure formula: 10S □ [4.665L 1.36H]$^4$ 4.665L 32.637H □ 1.0; ($\lambda_0 = 1.03$ μm, $n_L(AlAs) = 2.94$, $n_H(Al_{0.1}Ga_{0.9}As) = 3.43$, $n_S(GaAs) = 3.496$). Design could be useful for an applications were symmetric two-band AR coating is required.

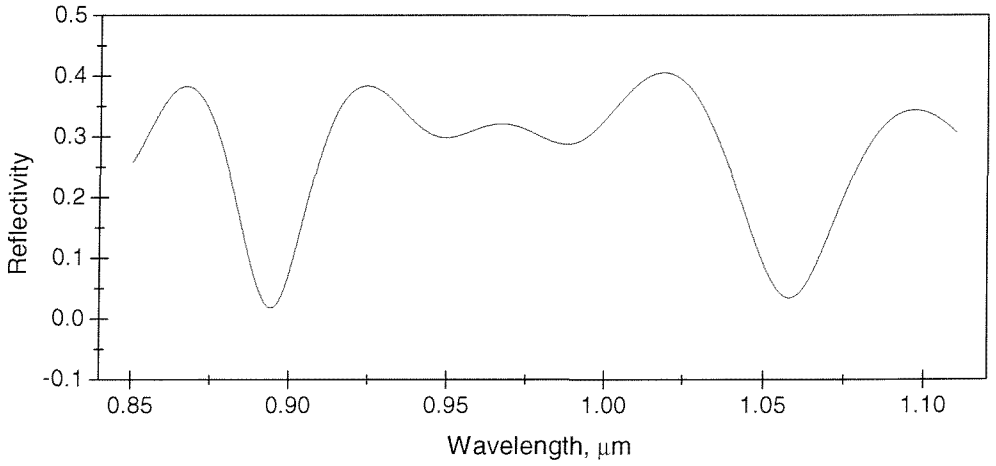


**Fig. CH.II. 7. 9.** Computed reflectivity of two-band antireflection coating as a function of wavelength. Structure formula: 8S □ 4.665L 4.742A 2.77H 2.332L 7.113A 2.77H 2.332L 7.113A □ 1.0; ($\lambda_0 = 1.03$ μm, $n_L(AlAs) = 2.94$, $n_H(GaAs) = 3.43$, $n_A(Al_{0.9}Ga_{0.1}As) = 2.993$, $n_S(GaAs) = 3.496$). Design is applicable to DP-VECSEL that is pumped at 0.908 μm and emitting near 1.06 μm.

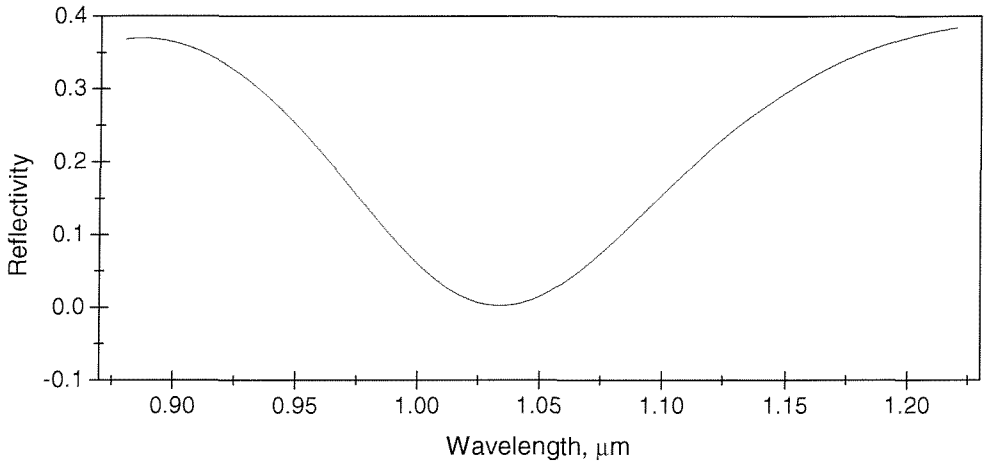


**Fig. CH.II. 7. 10.** Computed reflectivity of single-band antireflection coating as a function of wavelength. Structure formula: 7S □ [0.945L 1.083H]$^3$ 0.945L □ 1.0; ($\lambda_0 = 1.03$ μm, $n_L(AlAs) = 2.94$, $n_H(Al_{0.2}Ga_{0.8}As) = 3.373$, $n_S(GaAs) = 3.496$). This particular design achieved using triangle-shaped wide-angle desired transmission function centered at 1.04 μm. It shows symmetry and has only seven layers.

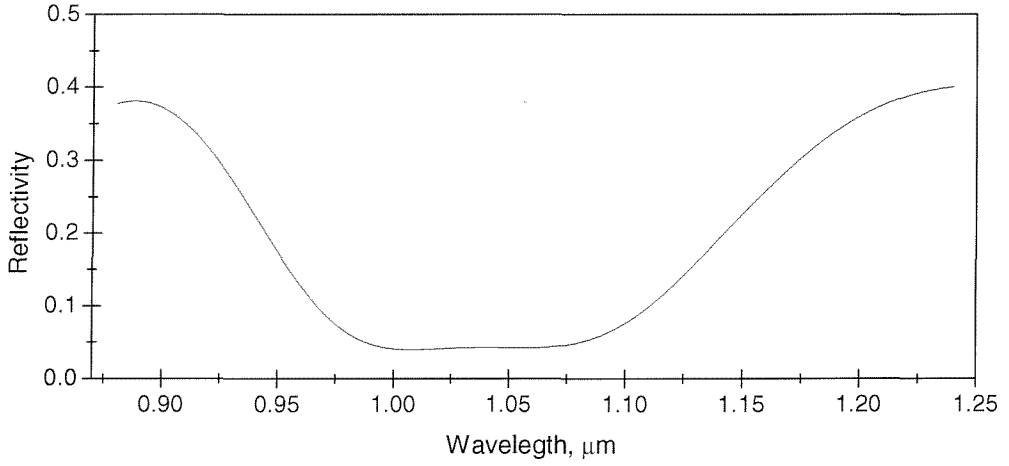


**Fig. CH.II. 7. 11.** Computed reflectivity of broad-band antireflection coating as a function of wavelength. Structure formula: 8S □ 1.413A 6.035L 1.083H [0.945L 1.083H]$^2$ 0.945L □ 1.0; ($\lambda_0 = 1.03$ μm, $n_L(AlAs) = 2.94$, $n_H(Al_{0.2}Ga_{0.8}As) = 3.373$, $n_A(Al_{0.1}Ga_{0.9}As) = 3.433$, $n_S(GaAs) = 3.496$). This particular design is applicable to a semiconductor device that requires flat AR coating in the spectral region exceeding ~70 nm.

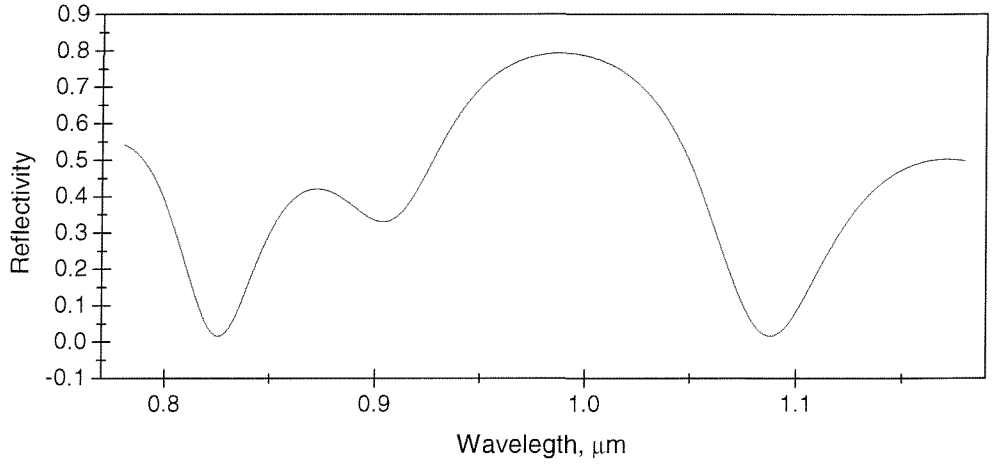


**Fig. CH.II. 7. 12.** Computed reflectivity of two-band antireflection coating as a function of wavelength. Structure formula: 14S □ 1.039L 0.673H 1.155L 0.673H 1.732L [0.673H 1.155L]$^3$ 2.693H 0.577L 1.347H □ 1.0; ($\lambda_0 = 1.03$ μm, $n_L(AlAs) = 2.94$, $n_H(Al_{0.1}Ga_{0.9}As) = 3.433$, $n_S(GaAs) = 3.496$). This design is applicable to DP-VECSEL that is pumped near 0.83 μm and emitting at 1.09 μm.

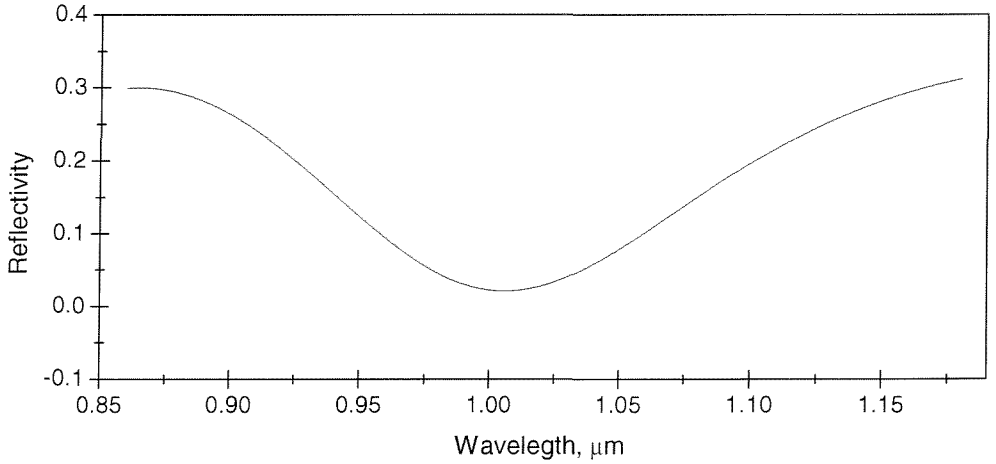


**Fig. CH.II. 7. 13.** Computed reflectivity of single-band antireflection coating as a function of wavelength. Structure formula: 7S □ 0.572L 0.667H 1.715L 0.667H 1.143L 0.667H 1.143L □ 1.0; ($\lambda_0 = 1.03$ μm, $n_L(AlAs) = 2.94$, $n_H(Al_{0.1}Ga_{0.9}As) = 3.433$, $n_S(GaAs) = 3.496$). This particular design achieved using triangle-shaped desired transmission function centered at 1.01 μm. It could be useful for an applications were symmetric AR coating is required.

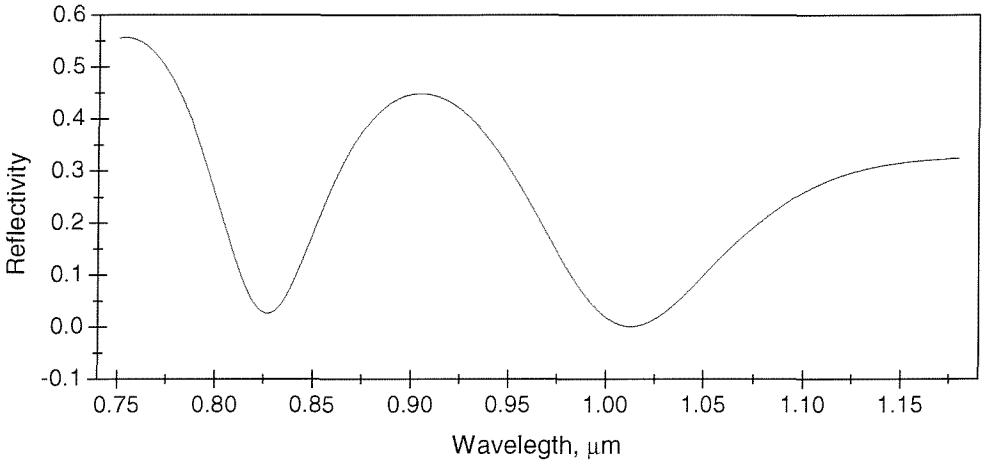


**Fig. CH.II. 7. 14.** Computed reflectivity of two-band antireflection coating as a function of wavelength. Structure formula: 11S □ 0.572L [0.667H 1.143L]$^2$ 0.667H 1.715L [0667H 1.143L]$^2$ □ 1.0; ($\lambda_0 = 1.03$ μm, $n_L(AlAs) = 2.94$, $n_H(Al_{0.1}Ga_{0.9}As) = 3.433$, $n_S(GaAs) = 3.496$). This design is applicable to DP-VECSEL that is pumped near 0.83 μm and emitting at 1.01 μm.

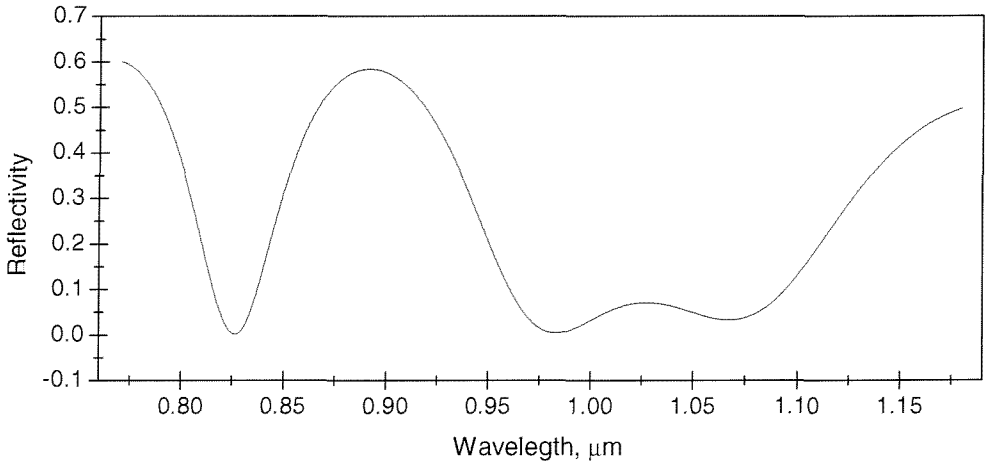


**Fig. CH.II. 7. 15.** Computed reflectivity of two-band antireflection coating as a function of wavelength. Structure formula: 15S □ [1.143L 0.667H]$^2$ 0.572L [0.667H 1.143L]$^2$ 0.667H 1.715L [0667H 1.143L]$^2$ □ 1.0; ($\lambda_0 = 1.03$ μm, $n_L(AlAs) = 2.94$, $n_H(Al_{0.1}Ga_{0.9}As) = 3.433$, $n_S(GaAs) = 3.496$). This design could be used for DP-VECSEL that is optically pumped near 0.803 μm and is tunable around 1.03 μm in the spectral region exceeding ~70 nm.

All numerical results that have been achieved using indirect design algorithms show very different and specific design solutions. In order to apply each design properly it is advisable to use refinement procedures in any case. Indirect design algorithms that include adaptive procedures could even modify desired specifications (to some degree of acceptance), and still generate very interesting and original design solutions. Therefore it is sufficient to conclude that indirect design algorithms have potential applications in almost any research and development area.

## CH.II. 8. Optical Gain and Laser Characteristics of DP-VECSEL

Optimization of the multi-quantum-well (MQW) laser structure is both costly and time consuming since there are innumerable possible combinations of optical confinement structure, well width, well number, and cavity length, only a few of which lead to useful devices. To prevent such a waste of time and money, a theoretical analysis of the problem and design algorithm is needed. Although there now exist a number of good models of the MQW laser, these are mostly concerned with specific structures, and give little information about the general optimization on MQW lasers. In this section very general and basic algorithm is discussed how any MQW structure may be optimized by constructing it out of individually optimized wells in DP-VECSEL.

### CH.II. 8-1. *Materials for Quantum Wells*

In general, semiconductors can be crystalline or amorphous solid materials in which electric conductivity is intermediate between metals and dielectrics, and is very strongly variable by changing temperature, amount of donor or acceptor impurities or by illumination with light ($h\nu \geq E_g$). These semiconductor properties arise from the energy level structure of these materials. Atoms in any material interact with one another, causing broadening of the atomic energy levels into bands corresponding to the electronic Bloch

states. Each band is formed by closely located discrete energy levels, which can be considered to form a continuum. Bands may be separated by forbidden regions of energy, to which no Bloch states correspond. It can then be found a specific forbidden band gap that is characteristic feature of the material. Materials that have $E_g > 3eV$, in which a valence band is filled by electrons, are dielectrics. Materials with small or absolutely with no forbidden band gap are conductors. Typical band gaps for semiconductors lie between 0.1 and 3 *eV*. The most widely used semiconductors after silicon are the binary combinations of III-V alloy semiconductors composed of (Al, Ga, In, ...) and (P, As, Sb, ...). These are enumerated in table CH.II. 8-1.

**Table CH.II. 8-1:** Selected semiconductors and their band gap energies; (I – indirect band gap, D-direct band gap).

| Material | Band gap energy, *eV* | Band gap wavelength, μm | Type |
|---|---|---|---|
| Ge | 0.66 | 1.88 | I |
| Si | 1.11 | 1.15 | I |
| AlP | 2.45 | 0.52 | I |
| AlAs | 2.16 | 0.57 | I |
| AlSb | 1.58 | 0.75 | I |
| GaP | 2.26 | 0.55 | I |
| GaAs | 1.42 | 0.87 | D |
| GaSb | 0.73 | 1.70 | D |
| InP | 1.35 | 0.92 | D |
| InAs | 0.36 | 3.5 | D |
| InSb | 0.17 | 7.3 | D |

The magnitude of the band gap of the ternary and quaternary alloys can be estimated from the binary data by interpolation:

$$E_{ABCD} = (1-x)(1-y)E_{AC} + x(1-y)E_{BC} + (1-x)yE_{AD} + xyE_{BD} \qquad \text{[CH.II. 8-1/1]}$$

for the $A_{1-x}B_xC_{1-y}D_y$ type, and

$$E_{ABCD} = xE_{AB} + yE_{AC} + (1-x-y)E_{AD} \qquad \text{[CH.II. 8-1/2]}$$

for the $AB_xC_yD_{1-x-y}$ type, where $E_{AB}$ is the energy of the top of the valence band of AB alloy. For example lattice-matched GaAs/$Al_xGa_{1-x}As$ material system can be used in short

wavelength 0.78-0.9 μm applications. For 1.3-1.55 μm applications, the quaternary lattice-matched $In_xGa_{1-x}As/InP$ material system is appropriate. It is obvious that the composition of four semiconductors allows more flexibility to choose semiconductor properties because of additional extent of freedom. For the sake of definition, a quantum well (QW) is a very thin layer of one semiconductor between two other semiconductor layers of higher band gap. If semiconductor layers composing the QW have the same lattice constant, the QW is unstrained or lattice-matched. Otherwise the QW is said to be under strain.

## CH.II. 8-2. *Refractive Index of $Al_xGa_{1-x}As$, $GaAs_{1-x}P_x$, $Ga_xIn_{1-x}P$*

Development of semiconductor-based devices requires accurate estimation of refractive index of different semiconductor materials for different alloy compositions. A simplified Semi-Empirical method for calculating the refractive index for some semiconductor materials as a function of wavelength and alloy composition has been developed by M. A. Afromowitz.[39] This method assumes that the imaginary part of the dielectric function can be represented by a single delta function at a specified energy. Then Kramers-Kronig dispersion relations can be used to estimate the refractive index. In this model, three energies must be defined as a function of mole fraction: the position of the delta function in energy, $E_0$, the strength of the delta function, $E_d$, and the $\Gamma$ valley band gap, $E_\Gamma$. These energies for three semiconductor material systems are summarized in table CH.II. 8-2.

**Table CH.II. 8-2:** List of $E_0$, $E_d$, $E_\Gamma$ energies for semiconductor $Al_xGa_{1-x}As$, $GaAs_{1-x}P_x$, and $Ga_xIn_{1-x}P$ materials.

| Energies, eV | $Al_xGa_{1-x}As$ | $GaAs_{1-x}P_x$ | $Ga_xIn_{1-x}P$ |
|---|---|---|---|
| $E_0$ | $3.65+0.871x+0.179x^2$ | $3.65+0.721x+0.139x^2$ | $3.391+0.524x+0.595x^2$ |
| $E_d$ | $36.1-2.45x$ | $36.1+0.35x$ | $28.91+7.54x$ |
| $E_\Gamma$ | $1.421+1.266x+0.26x^2$ | $1.441+1.091x+0.21x^2$ | $1.34+0.668x+0.758x^2$ |

If we let $E$ represent the energy at which we are evaluating the refractive index, then the approximate expression for the refractive index at room temperature is given by:

$$n^2(E) = 1 + \frac{\eta}{2\pi}\left(E_f^4 - E_\Gamma^4\right) + \frac{\eta}{\pi}\left(E_f^2 - E_\Gamma^2\right)E^2 + \frac{\eta}{\pi}E^4 \ln\left[\frac{E_f^2 - E^2}{E_\Gamma^2 - E^2}\right], \qquad \text{[CH.II. 8-2/1]}$$

where,

$$E_f = \left(2E_0^2 - E_\Gamma^2\right)^{1/2}, \quad \eta = \frac{\pi E_d}{2E_0^3\left(E_0^2 - E_\Gamma^2\right)}. \qquad \text{[CH.II. 8-2/2]}$$

It is important that the refractive index calculations are as efficient as possible to minimize the computation time. The normalization of Afromowitz's original expression reduces the number of algebraic operations by almost a factor of two. Expanding and eliminating $E_f$ and $\eta$, the original Afromowitz expression transforms into

$$n^2(E) = 1 + e_d\left[1 + e^2 + \frac{e^4}{2\alpha_\Gamma}\ln\left[\frac{\alpha + \alpha_\Gamma}{\alpha - \alpha_\Gamma}\right]\right], \qquad \text{[CH.II. 8-2/3]}$$

where

$$e = \frac{E}{E_0}, \quad e_d = \frac{E_d}{E_0}, \quad e_\Gamma = \frac{E_\Gamma}{E_0}, \quad \alpha = 1 - e^2, \quad \alpha_\Gamma = 1 - e_\Gamma^2. \qquad \text{[CH.II. 8-2/4]}$$

These formulas save approximately 30% of computation time compared to the original formulation and work well below the band gap of the material. However, as $E$ approaches the band gap, the argument of the natural log function goes to infinity. Above the band gap, the refractive index increases more or less linearly.[38] Adachi has also reported the approximate expressions for refractive indexes of GaP, GaAs, GaSb, InP, InAs, InSb, AlGAs, InGaAsP semiconductor materials in the range of 0-6 eV.[40] These expressions agree with experimental data over a wide energy range as well as Afromowitz's expression. However near the absorption energy level, calculated values of refractive index do not agree with experimental data.[38] More precise expressions for refractive index near the absorption edge for AlGaAs material was derived by Y. Kokubo.[41]

## CH.II. 8-3. *Carrier Induced Change in Refractive index*

There are three effects, band-filling, band gap shrinkage, and free-carrier absorption, that can produce substantial contributions to the total carrier induced changes in the refractive index. It is advantageous to take these effects into account when optimizing DP-VECSEL designs. Precise estimates of the effects can be found in literature.[42-46] Here it is only sufficient to mention basic principles without going into mathematical formulation.

- Band-filling.[42] A decrease in absorption for photon energies slightly above the nominal band gap has been observed for several semiconductors when they are doped. The effect is most pronounced in semiconductors with small effective masses and energy gaps. In the case of n-type semiconductors, the density of states in the conduction band is sufficiently low that a relatively small number of electrons can fill the band to an appreciable depth. With the lowest energy states in the conduction band filled, electrons from the valence band require energies greater than the nominal band gap to be optically excited into the conduction band. Hence, there is a decrease in the absorption coefficient at energies above the band gap. The situation is similar for holes in p-type semiconductor materials, but their larger effective mass means a higher density of states and hence a smaller band-filling effect for a given carrier concentration.
- Band gap shrinkage (renormalization). The basic mechanism is that injected electrons will occupy states at the bottom of the conduction band. If the concentration is large enough, the electron wave functions will overlap, forming a gas of interacting particles. The electrons will repel one another by Coulomb forces. In addition, electrons with the same spin will avoid one another for statistical reasons. The net result is a screening of electrons and a decrease in their energy, lowering the energy of the conduction band edge. A similar correlation effect for holes increases the energy of the valence band edge. The sum of these effects is band gap shrinkage. Shrinkage effects are determined by free carrier density, and are nearly independent of impurity concentration.[42]
- Free-carrier absorption. It is well known that a free carrier can absorb a photon and move to a higher energy state within a band. This intraband free-carrier absorption is

also known as the plasma effect, and is directly proportional to the concentrations of electrons and holes and the square of the wavelength. The sign of refractive index change from the plasma effect is always negative. Because of the square of the wavelength dependence, the plasma effect increases as the photon energy is decreased below the band gap. On the other hand, both the band-filling and band gap shrinkage effects on refractive index are largest near the band gap and approach zero for energies much below the band gap.

All three effects can give substantial contributions to the refractive index near the direct gap of III-V semiconductors. The band-filling and free-carrier absorption effects both produce a negative change in refractive index for a wavelengths in the transparent regime of the semiconductors; band gap shrinkage produces a positive change in refractive index in the same regime.

## CH.II. 8-4. *Gain, Threshold, and Output Power (CW Regime)*

The output laser characteristics of DP-VECSEL lasers can be estimated using a simplified model of the interaction between a standing wave electromagnetic field and the active gain medium. In such a theory, we first calculate the standing wave pattern neglecting any gain, and then calculate the total gain including standing wave effects within the QWs. An analogous argument holds for an absorptive case. This simple theory provides some simple analytic results, and gives a useful first approximation.[47-49] The standing wave intensity pattern for a monochromatic wave of wavevector $k$ in the positive $z$ direction (i.e., corresponding to propagation from the left to the right) is

$$I(z) = 2I_0(1+\cos(2kz)), \qquad \text{[CH.II. 8-4/1]}$$

where we have chosen $z = 0$ at the position of the mirror. For zero phase change on reflection, an antinode occurs at the mirror surface. If necessary, it is straightforward to extend this theory to include a phase shift on reflection by including a phase angle in the cosine term of [CH.II. 8-4/1]. Wavelength-dependent phase shifts, common in many mirrors, could also be straightforwardly included. For a QW of thickness $d$ centered at position $z_p$, the actual gain (the product of the gain per unit length and the effective gain length) in the standing wave will be

$$G = 2g\int_{z_p-d/2}^{z_p+d/2}(1+\cos(2kz))dz = 2g\left[d+\frac{1}{k}\sin(kd)\cos(2kz_p)\right]. \quad \text{[CH.II. 8-4/2]}$$

We can see that for a gain element positioned exactly at an antinode, $\cos(2kz_p)=+1$, then $G_{antinode}=4gd$. The factor of 4 comes from two factors of 2, one due to the fact that we have beams of unit intensity propagating in both directions (so that the average overall intensity is 2 units), and the other due to the standing wave effect. When the QW is exactly centered on a node, $\cos(2kz_p)=-1$, the resulting gain is, to lowest order in $k$,

$$G_{node} = \frac{gk^2d^3}{3} = \frac{4\pi^2}{3}\frac{gd^3}{\lambda^2}, \quad \text{[CH.II. 8-4/3]}$$

where $\lambda$ is the wavelength. We use the empirical logarithmic dependence of the gain $g$ on the carrier density $N$ in QWs

$$g = g_0\ln(N/N_0), \quad \text{[CH.II. 8-4/4]}$$

where $g_0$ is the material gain parameter, $N$ is the carrier density, and $N_0$ is transparency carrier density. The lasing threshold condition is

$$R_1R_2T_{loss}e^{G_{th}N_g} = R_1R_2T_{loss}e^{2\Gamma g_{th}N_g d} = 1 \quad \text{[CH.II. 8-4/5]}$$

where $R_1$ and $R_2$ are the cavity mirror reflectivities, $T_{loss}$ is the transmission factor due to round-trip cavity loss, $g_{th}$ is the threshold material gain, $N_g$ is the number of QWs. The longitudinal confinement factor $\Gamma$ characterizes overlap between the optical standing wave and the QWs spaced inside gain region. The carrier density $N$ below threshold can be calculated from the incident pump power $P_p$:

$$N = \frac{\eta_{abs}P_p}{h\nu N_g dA_p}\tau(N). \quad \text{[CH.II. 8-4/6]}$$

Here, $\eta_{abs}$ is the pump absorption efficiency, $h\nu$ is the photon energy, $A_p$ is the pump spot area, and $\tau$ is the carrier lifetime. Carrier lifetime is given by

$$\frac{1}{\tau(N)} = A + BN + CN^2 \quad \text{[CH.II. 8-4/7]}$$

where $A$, $B$, $C$ are the monomolecular, bimolecular, and Auger recombination coefficients. Using [CH.II. 8-4/1]-[CH.II. 8-4/7], we can derive expressions for the threshold carrier density $N_{th}$ and threshold pump power $P_{th}$:

$$\begin{cases} N_{th} = N_0 \left( \dfrac{1}{R_1 R_2 T_{loss}} \right)^{1/(2\Gamma g_0 N_g d)} \\ P_{th} = N_{th} \dfrac{h\nu N_g dA_p}{\eta_{abs} \tau(N_{th})} \end{cases} . \qquad \text{[CH.II. 8-4/8]}$$

The output power of the optically pumped semiconductor laser then is given by

$$P_{out} = (P_p - P_{th}) \eta_{diff} \qquad \text{[CH.II. 8-4/9]}$$

where the differential efficiency $\eta_{diff}$ is

$$\eta_{diff} = \eta_{out} \eta_{quant} \eta_{abs} . \qquad \text{[CH.II. 8-4/10]}$$

In addition to the pump absorption efficiency, $\eta_{abs}$, the components of the differential efficiency are the output efficiency,

$$\eta_{out} = \frac{\ln(R_2)}{\ln(R_1 R_2 T_{loss})}, \qquad \text{[CH.II. 8-4/11]}$$

where $R_2$ is the laser output mirror reflectivity, and the quantum efficiency

$$\eta_{quant} = \lambda_{pump} / \lambda_{laser} . \qquad \text{[CH.II. 8-4/12]}$$

From the above equations it follows that the discrimination against nonresonant wavelengths improves with increasing number of QWs, a situation analogous to the resolution of a grating being improved by illumination of a large area which includes more grating periods. Therefore in case of applications that require spectrally broad gain, QWs could have slightly different alloy compositions and placed at slightly deviant from their resonant positions. In general, the effective gain coefficient at the resonant wavelength in the vertical direction is twice as high as that in the transverse direction. It then follows that transverse amplified spontaneous emission is reduced by a factor of two, so that the semiconductor lasers with periodic gain elements have a reduced threshold and increased overall power efficiency compared to conventional structures with nonresonant periodic gain media.

## CH.II. 8-5. *Laser Temperature Characteristics*

In this section a very simple model is introduced to describe the temperature characteristics of any measurable laser parameter $X$ (such as threshold, differential quantum efficiency) in terms of the normalized change with respect to temperature $T$ .We can write

$$\frac{1}{X}=\frac{dX}{dT}=\frac{d\ln(X)}{dT}\equiv\pm\frac{1}{T_X} \qquad \text{[CH.II. 8-5/1]}$$

where $T_X$ is the characteristic temperature of parameter $X$ and + (-) sign is used when the value of $X$ increases (decreases) with temperature. Characteristic temperatures of threshold ($T_0$), external quantum efficiency ($T_e$), a maximum operation temperature ($T_{max}$) can be estimated from measurable laser parameter data. For example, characteristic temperatures define the optimum carrier confinement conditions, the best overlapping between standing wave optical field and QWs. It is well known that a high temperature laser is more cost effective and reliable than one that is thermoelectrically cooled because of its simplicity in packaging. Therefore in principle the design of high temperature lasers in terms of the quantum well number and the mirror loss is quite different from that of low-threshold lasers. QW structure for high temperature operation has to be optimized minimizing the temperature sensitivity in threshold and slope efficiency. Then any specific design of quantum well structure could be characterized by characteristic temperature of laser parameter.

## CH.II. 8-6. *CW Passive Mode Locking Regime*

Mode-locking is a very useful technique to generate ultra-short pulses in lasers. During the mode-locking process, many simultaneously oscillating axial modes in the laser cavity are locked or coupled together using an intra-cavity modulator. From a time-domain point of view, the output of mode-locked laser usually takes the form of an extremely short optical pulse train. This is the result of circulating short pulse inside the laser cavity and partially emerging through an end facet at a repetition rate corresponding

to the round-trip time inside the laser cavity. From a frequency point of view, the spectrum of a mode-locked laser shows many oscillating modes that are locked in phase. In general, mode-locking involves several physical mechanisms responsible for short pulse formation and stabilization.

Mode-locking can be classified as passive, active, passive-active, passive or active with negative active or passive feedback control[50-63], colliding pulse mode-locking (CPM)[64-66], additive pulse mode-locking (APM)[67-70], Kerr lens mode-locking (KLM)[71-72], soliton mode-locking[73-74]. The traditional approach to passive mode-locking has been to use a saturable absorber. In pulsed mode-locked lasers, the simultaneous Q-switching effect prevented efficient pulse shortening because of the early saturation of the saturable absorber. Active and passive feed-back control schemes have been devised to overcome this limitation. In CPM the two counter-propagating pulses inside the ring cavity collide in the saturable absorber to form an instantaneous standing-wave grating, which enhances the saturation of the saturable absorber and shortens the pulse duration. It has been shown that self-phase modulation (SPM) and group velocity dispersion (GVD) are the main factors in generating shorter pulses, while collision in a CPM laser lowers the mode-locking threshold and stabilizes mode-locking operation. APM is based on the coherent addition of a weak nonlinear phase shifted pulse returning from the coupled nonlinear auxiliary cavity to interfere with the main cavity pulse. The artificial saturable absorber action introduced by this coherent field superposition process has an extremely fast response time and broad bandwidth. In APM the time-dependent phase shift induced by Kerr nonlinearities (intensity-dependent index of refraction) has been utilized for passive modulation. However, this phase shift depends not only on time but also on the transverse spatial coordinates, thus leading to an intensity dependent variation of the beam profile. Combined with some spatial aperture, the intensity dependent beam diameter provides an extremely simple means of ultra-fast all-optical modulation. This effect can be enhanced by introducing an additional hard aperture in the cavity, or by using a soft aperture such as the pumped volume in the gain medium.

In each case the pulse formation dynamics are very similar - simultaneously oscillating axial modes experience amplitude-phase fluctuations, and form competitive mode clusters that finally develop into one with relatively stable amplitude-phase characteristics. In time domain, this mode cluster corresponds to a pulse.

Many different models have been developed to study pulse evolution and the necessary conditions to achieve it. The interested reader is referred for a detailed overview to a number of papers.[63-74] Here, it is sufficient to refer to one model that is mostly appropriate. In this section only the necessary conditions to achieve CW passive mode-locking of semiconductor laser are discussed. It is well established that passive mode-locking is a cost effective and reliable technique for generating ultra-short pulses. A common feature of passively mode-locked lasers is the existence of a threshold intra-cavity power required for self-starting. They typically have two possible steady-state or equilibrium behaviors. The first one is continuous wave operation and the second is pulsed operation. Of course, a third possibility, often observed in practice, is that there is no steady state operation. It is desirable for the laser to self-start into pulsed operation without the need for any further modulation or adjustment of the laser. Discussing the details of such laser we will focus on the topic of how to passively mode-lock them. First of all, laser should have a saturable absorber - passive modulator. The threshold for the intra-cavity pulse energy $E_p$, above which stable CW mode-locking is achieved is then given by[62]

$$E_p^2 > F_{sat,L} A_L F_{sat,A} A_A \Delta R = E_{sat,L} E_{sat,A} \Delta R \,. \qquad \text{[CH.II. 8-6/1]}$$

$E_{sat,L}$ is the saturation energy of the gain, which is defined as the product of saturation fluence $F_{sat,L} = h\nu/(m\sigma_L)$ and the effective laser mode area inside the gain medium $A_L$. The effective mode area is defined as $A_L = \pi w^2$, where $w$ is the $1/e^2$ Gaussian beam radius with respect to intensity. $h\nu$ is the laser photon energy and $\sigma_L$ the emission cross section of the gain. The factor $m$ in the definition of $F_{sat,L}$ is the number of passes through the gain element per cavity round trip. Because of this factor, the gain saturation depends on the geometry of the laser cavity. For example, for a ring cavity, $m = 1$, while for a standard standing-wave cavity $m = 2$. For a cavity with multiple passes through the gain medium, $m$ respectively can be larger than 2. $E_{sat,A}$ denotes the absorber saturation energy and is defined by the product of absorber saturation fluence $F_{sat,A}$ and effective laser mode area on the saturable absorber $A_A$. The term $\Delta R$ corresponds to saturable absorber modulation depth. The absorber recovery time must be much shorter than the cavity round-trip time. A specific model has been developed that includes both the slow and fast components of saturable absorber saturation for stability analysis.[63] It was shown

analytically that the fast component of the absorption helps considerably in the formation of short pulses, defines self-starting conditions. For pulse widths of the order of 1 psec or less, the slow saturable absorber component does not necessary contribute to pulse stability. The slow saturable absorber component controls the stability conditions preventing relaxation oscillations, and the conditions for pulse formation at the repetition frequency corresponding to the cavity round-trip time. The absorber parameters are very important and can be custom designed within a wide range. Perhaps it is useful to rewrite equation [CH.II. 8-6/1] criterion introducing the saturation parameter

$$S = E_p / E_{sat,A} \qquad \text{[CH.II. 8-6/2]}$$

thus obtaining

$$E_p > E_{sat,L} \frac{\Delta R}{S}. \qquad \text{[CH.II. 8-6/3]}$$

The pulse energy $E_p$ enters this equation both directly and indirectly through the saturation parameter $S$, but this form of the equation is useful for the following discussions. The saturation parameter affects pulse energetic and temporal characteristics. With increasing $S$, the saturable absorber is more strongly saturated, and mode cluster discrimination conditions are more effective. With decreasing $\Delta R$, the discrimination level is reduced, and this typically leads to longer pulses. For a given values of $\Delta R$ and $S$ we can control the intra-cavity pulse energy using an output coupler with smaller or higher transmission coefficient. Another very practical way of optimizing passively mode-locked laser output characteristics is to change laser cavity length (cavity round-trip time). It is reasonable to assume that, as the cavity is made shorter, while the overage power remains constant, the energy per pulse decreases accordingly. The pulse width is inversely proportional to the pulse energy. Thus the pulse width is expected to scale inversely with the cavity length. The cavity could be made quite short if one is willing to sacrifice pulse width.

## CH.II. 8-7. *Strained $In_{1-x}Ga_xAs_yP_{1-y}$ Quaternary Material for QW Lasers*

The use of strained quaternary $In_{1-x}Ga_xAs_yP_{1-y}$ material for QW lasers allows far wider scope for possible laser structures.[75,76] The growth of strained layer structures in this material system is mainly focused on the use of ternary $In_{1-x}Ga_xAs$ quantum wells and quaternary $In_{1-x}Ga_xAs_yP_{1-y}$ barriers. This gives a wide variation in quantum well width and in the composition and strain in both the well and barrier. In principle there is a limit to the amount of strained material that can be introduced and hence a limit to the number of strained quantum wells that can be grown between lattice-matched barriers while maintaining device quality material.[77] It is possible to use oppositely strained well and barrier materials to balance out the strain over an entire structure. So long as the strain in each layer does not exceed a critical value, it is then possible to design zero net-strain structures, and compensated strain structures where no maximum is set on the number of quantum wells. The useful growth combinations are then compressive wells with unstrained or tensile barriers, and tensile wells with unstrained or compressive barriers. In addition, structures can be grown which contain both compressive and tensile wells with unstrained barriers. The carrier leakage through the barrier is one important factor causing the laser characteristic degradation at high temperature and carrier density.[78] Due to the difference in the effective mass, the electron with its lighter effective mass requires a tighter confinement than the hole. Therefore, in quantum well structures the $In_{1-x}Ga_xAs_yP_{1-y}/In_{1-x}Ga_xAs/In_{1-x}Ga_xAs_yP_{1-y}$ for its larger conduction band offset instead of $GaAs/In_{1-x}Ga_xAs/GaAs$ can provide a strong electron confinement in the well and maintain uniform hole distribution among the wells. The larger the conduction band offset, the better the electron confinement in the conduction band and, therefore the higher the temperature stability. It is difficult to investigate all possible well and barrier combinations; easier to search for optimum quantum well laser structure by focusing on optimized key parameters in quantum well design such as well width and strain. This allows the important trends to be established which can then be applied to other quantum well laser structures.[79,80]

## CH.II. 8-8. *DP-VECSEL Gain Structure Design*

This section describes a DP-VECSEL design that was achieved using an indirect design method and optimization procedures. In general the entire DP-VECSEL can be expressed by the formula: Air □ two-band-AR 6-QW-gain-region two-band-HR buffer-layer □ Substrate. The profile of the conduction band edge in the structure is shown in Fig. CH.II. 8-8. 1.

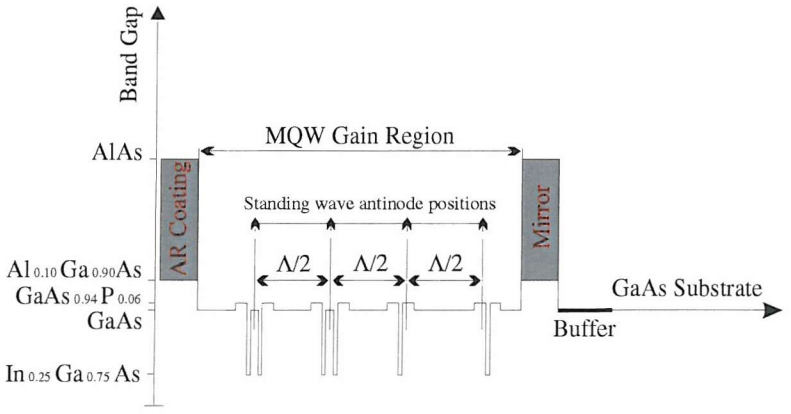


**Fig. CH.II. 8-8. 1:** Conduction band diagram of DP-VECSEL design. DP-VECSEL consists of three structural elements: two-band AR coating, MQW gain region, two-band mirror.

A DP-VECSEL structure was designed for pump at 0.83 μm and 1.03μm lasing wavelengths. The two-band normal incidence AR coating is shown in Fig. CH.II. 7. 14. Two-band AR layer sequence is 11S □ 0.572L [0.667H 1.143L]$^2$ 0.667H 1.715L [0667H 1.143L]$^2$ □ 1.0; ($\lambda_0 = 1.03$ μm, $n_L(AlAs) = 2.94$, $n_H(Al_{0.1}Ga_{0.9}As) = 3.433$, $n_S(GaAs) = 3.496$). The AR region has alloy composition AlAs-$Al_{0.1}Ga_{0.9}As$ that is transparent at 0.83 μm pump wavelength and has been optimized to have reflectivity equal to approximately 1% at 0.83μm and 1.03μm. Therefore almost all the pump power can be efficiently transmitted to the gain region. The gain region has in total 6-QWs: two $GaAs_{0.94}P_{0.06}$- $In_{0.25}Ga_{0.75}As$-GaAs, two GaAs-$In_{0.25}Ga_{0.75}As$-$GaAs_{0.94}P_{0.06}$ and two $GaAs_{0.94}P_{0.06}$- $In_{0.25}Ga_{0.75}As$-$GaAs_{0.94}P_{0.06}$ with QW alloy composition optimised

@1.01μm. DP-VECSEL at room temperature will operate near 1.03 μm. GaAs in the active gain region absorb around 75% of pump energy in single pass, then induced carriers drop into the QWs to provide gain near 1.03μm. The carrier leakage through the barrier layer is one important factor causing the laser performance degradation at high temperature and high carrier density. All QWs have $GaAs_{0.94}P_{0.06}$ barriers to increase conduction band offset and carrier confinement, and in addition to compensate for the strain between GaAs and $In_{0.25}Ga_{0.75}As$. Without strain-compensating $GaAs_{0.94}P_{0.06}$ layers, DP-VECSEL structure having 6-$In_{0.25}Ga_{0.75}As$ QWs exceed the critical thickness limit. Therefore compressive (1.8%) strain of $In_{0.25}Ga_{0.75}As$ QWs is compensated by the tensile-strained $GaAs_{0.94}P_{0.06}$ strain-compensating barriers. First two and next two QWs form QW pairs that are placed symmetrically near the standing wave antinode maxima. These $In_{0.25}Ga_{0.75}As$ QW pairs have $GaAs_{0.94}P_{0.06}$ barriers from one side and GaAs barrier between them in order to achieve more uniform carrier confinement in both QWs. These quasi-strained QWs are used to reduce the laser threshold, Auger recombination, and intervalence band absorption through reducing the in-plane hole effective mass by the combination of biaxial strain and quantum confinement. The strain is compensated for QW pair. The last two QWs are of same alloy composition and are shifted by 2% apart from their standing wave antinode positions, 4% apart from each other. This is to minimise sensitivity of laser characteristics to the temperature and growth errors. The average longitudinal confinement factor is equal approximately to 1.8. In general, QW positions in the gain region were refined optimising electromagnetic field at each QW and integrating with respect to the wavelength. The two-band HR mirror follows MQW gain region. HR mirror formula: 71S □ 0.59L 1.03H 0.88L 1.37H 0.88L 1.03H 1.18L 0.35H 1.18L 0.69H 1.18L $[1.03H\ 0.88L]^2$ 1.37H $[0.88L\ 1.03H]^3$ 0.88L 1.37H $[0.88L\ 1.03H]^3$ 0.88L 1.37H $[0.88L\ 1.03H]^3$ 0.88L 1.37H $[0.88L\ 1.03H]^3$ 0.88L 1.37H $[0.88L\ 1.03H]^3$ 0.88L 1.37H $[0.88L\ 1.03H]^3$ 0.73L □ 3.496; ($\lambda_0 = 1.03$ μm, $n_L(AlAs) = 2.94$, $n_H(Al_{0.1}Ga_{0.9}As) = 3.433$, $n_S(GaAs) = 3.496$). To avoid possible absorption of the pump power in GaAs substrate and increase absorption efficiency, pump radiation is reflected back from HR mirror to the gain region.

Fig. CH.II. 8-8. 2. shows computed reflectivity as a function of wavelength of two-band AR region and two-band HR that comprising the DP-VECSEL. AR region is matched with HR region @ 0.83 μm and @ 1.02 μm.

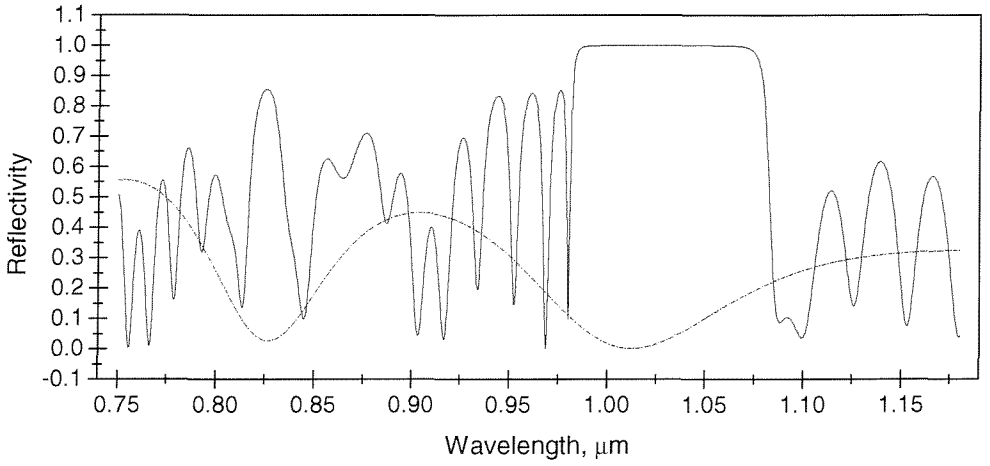


**Fig. CH.II. 8-8. 2:** Computed reflectivity as a function of wavelength of two-band AR region (solid line) and two-band HR (dotted line) that comprising the DP-VECSEL. AR structure formula: 11S □ 0.572L $[0.667H\ 1.143L]^2$ 0.667H 1.715L $[0667H\ 1.143L]^2$ □ 1.0; HR structure formula: 71S □ 0.59L 1.03H 0.88L 1.37H 0.88L 1.03H 1.18L 0.35H 1.18L 0.69H 1.18L $[1.03H\ 0.88L]^2$ 1.37H $[0.88L\ 1.03H]^3$ 0.88L 1.37H $[0.88L\ 1.03H]^3$ 0.88L 1.37H $[0.88L\ 1.03H]^3$ 0.88L 1.37H $[0.88L\ 1.03H]^3$ 0.88L 1.37H $[0.88L\ 1.03H]^3$ 0.88L 1.37H $[0.88L\ 1.03H]^3$ 0.88L 1.37H $[0.88L\ 1.03H]^3$ 0.73L □ 3.496; ($\lambda_0 = 1.03$ μm, $n_L(AlAs) = 2.94$, $n_H(Al_{0.1}Ga_{0.9}As) = 3.433$, $n_S(GaAs) = 3.496$).

Fig. CH.II. 8-8. 3. shows the calculated threshold pump power as a function of the number of QWs for several output couplers. The threshold power is in the range of 100 mW for 6 QWs. Fig. CH. II. 8-8. 4. shows the calculated output laser power as a function of the number of QWs for several different output couplers. Output laser power for 6QWs is in the range of 500 mW for the 2W incident pump power and using 2% output coupler.

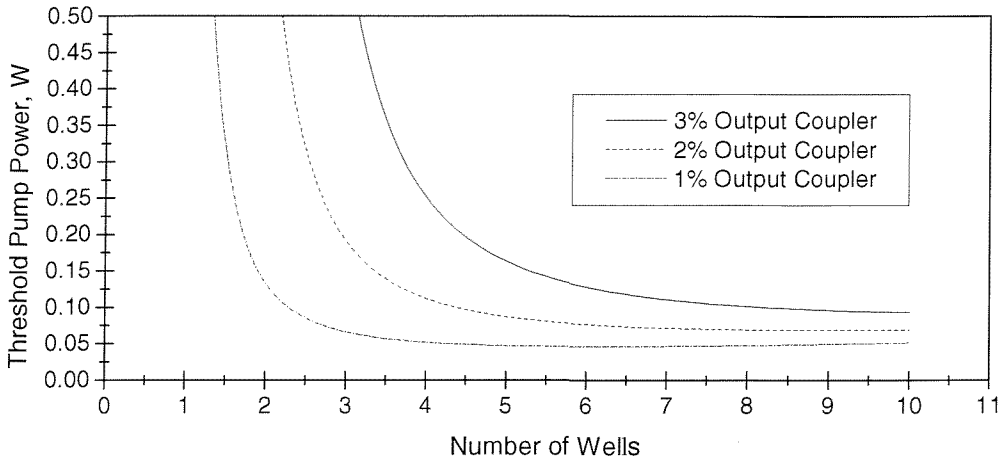


**Fig. CH.II. 8-8. 3:** Threshold pump power versus number of QWs calculated using equation [CH.II. 8-4/8] for three different values of output coupler (1% output coupler – dotted line, 2% output coupler – dashed line, 3% output coupler – solid line).

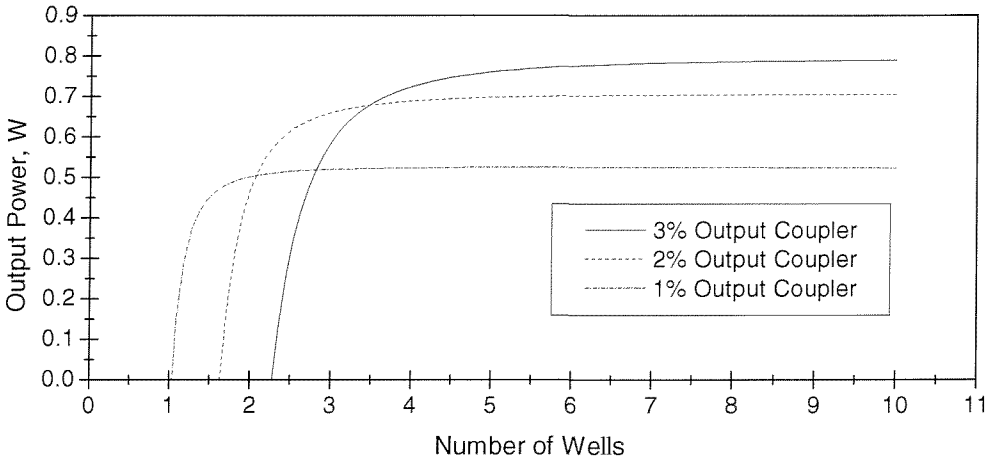


**Fig. CH.II. 8-8. 4:** Output power versus number of QWs calculated using equation [CH.II. 8-4/9] for three different values of output coupler (1% output coupler – dotted line, 2% output coupler – dashed line, 3% output coupler – solid line).

Fig. CH.II. 8-8. 5. shows the calculated output laser power as a function of the input pump power. Theoretical calculations indicate that more than 25% slope efficiency can be achieved from 6-QW DP-VECSEL.

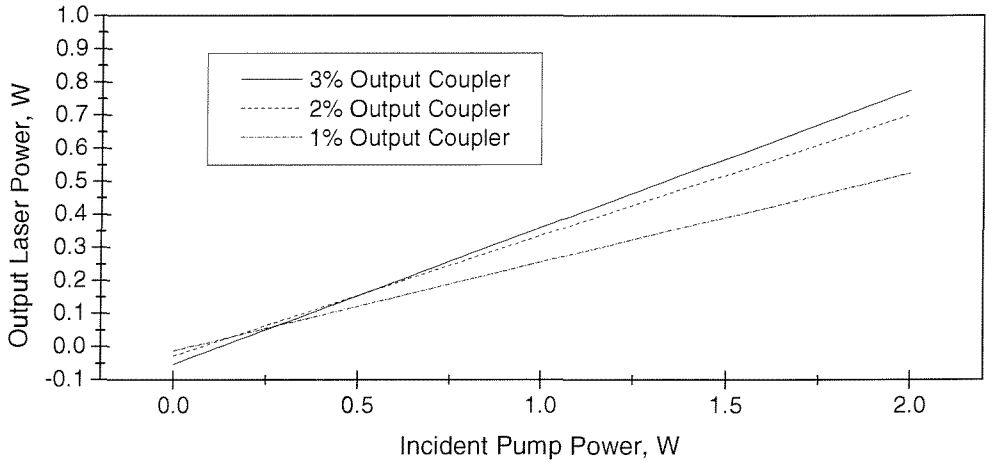


**Fig. CH.II. 8-8. 5:** Output laser power versus incident pump power calculated using equation [CH.II. 8-4/9] for three different values of output coupler (1% output coupler – dotted line, 2% output coupler – dashed line, 3% output coupler – solid line).

The laser and material parameters used in the calculations are summarized in table CH.II. 8-8. 2. There were two attempts to grow DP-VECSELs using standard MOCVD growth (wafers: QT1656 and QT1677). In both cases growth was unsuccessful. Samples were having remarkable surface degradation with very complex combination of surface defects. DP-VECSEL was designed to have strain-balanced structure. However high density of crater-like surface defects have shown growth problems associated with balancing the chemical reaction. Growth also was complicated because the whole DP-VECSEL structure had aperiodic character. Perhaps the same DP-VECSEL but with metal back mirror would be the option for future improvements. The use of metal-based mirrors usually offers broad-band high reflection within thin metal thickness what also improves thermal contact between gain region and heatsink. Most importantly boundary conditions at the metal-semiconductor interface are much more defined than in the case of semiconductor-semiconductor interface. In that way standing wave optical field will be fixed within QWs more accurately. This also helps to avoid any undesirable phase fluctuations in relatively long DBR mirrors. The combination of two-band AR, MQW gain region and metallic

mirror could be perfect. Very specific discussions about further DP-VECSEL development and improvements will be summarised at the end of this thesis (see future work).

**Table CH.II.8-8. 2:** List of laser and material parameters used in the DP-VECSEL laser characteristic calculations.

| Parameter | Description | Value | Units |
|---|---|---|---|
| $g_0$ | Material gain coefficient | 2000 | $cm^{-1}$ |
| $N_0$ | Transparency carrier density | $1.75x10^{18}$ | $cm^{-3}$ |
| $\Gamma$ | Longitudinal confinement factor | 1.8 | - |
| $L_{QW}$ | Quantum well thickness | 10.0 | nm |
| $R_B$ | On-wafer mirror reflectivity | 0.999 | - |
| $T_{Loss}$ | Roundtrip loss transmission factor | 0.990 | - |
| $\lambda_{Laser}$ | Laser wavelength | 1.03 | µm |
| $\lambda_{Pump}$ | Pump wavelength | 0.83 | µm |
| $d_{Pump}$ | Pump spot diameter | 140 | µm |
| $\eta_{abs}$ | Pump absorption efficiency | 0.75 | - |
| $A$ | Monomolecular recombination coefficient | $1.0x10^{7}$ | $s^{-1}$ |
| $B$ | Bimolecular recombination coefficient | $1.0x10^{-10}$ | $cm^3/s$ |
| $C$ | Auger recombination coefficient | $6.0x10^{-30}$ | $cm^6/s$ |

## CH.II. 9. References


1. I. V. Grebenshchikov, *Prosvetlenie Optiki* (*Antireflection Coating of Optical Surfaces*) (State Publishers of Technical and Theoretical Literature, Moscow, 1946).
2. J. T. Cox and G. Hass, "Antireflection coatings for optical and infrared optical materials," in *Physics of Thin Films*, G. Hass and R. E. Thun, eds. (Academic, New York, 1964), pp. 239-304.
3. H. A. Macleod, *Thin-Film Optical Filters* (Adam Hilter, London, 1969).
4. M. Born and E. Wolf, *Principles of Optics* (Pergamon, New York, 1970), pp. 51-70.
5. A. Mussett and A. Thelen, "Multilayer antireflection coatings," in *Progress in Optics,* E. Wolf, ed. (Pergamon, New York, 1970), pp. 203-237.
6. P. G. Kard, *Analysis and Synthesis of Multilayer Interference Coatings* (Valgus, Tallin, Estonia, 1971) (in Russian).
7. H. A. Macleod, *Thin Film Optical Filters* (McGraw-Hill, New York, 1986).
8. A. Thelen, *Design of Optical Interference Coatings* (McGraw-Hill, New York, 1988).
9. S. Furman and A. V. Thikhonravov, *Basics of Optics of Multilayer Systems* (Editions Frontieres, Gif-sur-Yvette, France, 1992).
10. E. Delano, "Fourier Synthesis of Multilayer Filters," J. Opt. Soc. Am. **57,** 1529-1553 (1967).
11. L. Sossi, "A Method for the Synthesis of Multilayer Dielectric Interference Coatings," Eesti NSV Tead. Akad. Toim. Fuus. Mat. **23,** No. 3, 229-237 (1974).
12. L. Sossi, "On the Theory of the Synthesis of Multilayer Dielectric Light Filters," Eesti NSV Tead. Akad. Toim. Fuus. Mat. **25,** No. 2, 171-176 (1976).
13. L. Sossi, "Synthesis of Dielectric Interference Filters with Narrow Reflection Bands," Eesti NSV Tead. Akad. Toim. Fuus. Mat. **28,** No. 3, 213-220 (1979).
14. J. A. Dobrowolski and D. Lowe, "Optical Thin Film Synthesis Program Based on the Use of Fourier Transforms," Appl. Opt. **17,** 3039-3050 (1978).
15. J. A. Dobrowolski, "Comparison of the Fourier transform and flip-top thin-film synthesis methods," Appl. Opt. **25,** 1966-1972 (1986).

16. P. G. Verly, J. A. Dobrowolski, W. J. Wild, and R. L. Burton, "Synthesis of high rejection filters with the Fourier transform method," Appl. Opt. **28,** No 14, 2864-2875 (1989).

17. P. G. Verly, J. A. Dobrowolski, and R. R. Willey, "Fourier-transform method for the design of wideband antireflection coatings," Appl. Opt. **31,** No. 19, 3836-3846 (1992).

18. R. M. Bracewell, *The Fourier Transform and its Applications* (McGraw-Hill, New York, 1965).

19. J. A. Dobrovolski, "Subtractive Method of Optical Thin-Film Interference Filter Design," Appl. Opt. **12,** 1885-1893 (1973).

20. S. F. Masri and G. A. Bekey, "A Global Optimization Algorithm Using Adaptive Random Search," Appl. Math. Comput. **7,** 353-375 (1980).

21. J. F. Tang, Q. Zheng, "Automatic design of optical thin-film systems – merit function and numeric optimization method," J. Opt. Soc. Am. **72,** 1522-1528 (1982).

22. P. W. Baumeister, "Design of Multilayer Filters by Successive Approximations," J. Opt. Soc. Am. **48,** 955-958 (1958).

23. J. A. Dobrowolski, "Automatic Refinement of Optical Multilayer Assemblies," J. Opt. Soc. Am. **51,** 1475 (1961).

24. A. L. Bloom, "Refining and Optimization in Multilayers," Appl. Opt. **20,** 66-73 (1981).

25. L. E. Scales, *Introduction to Non-Linear Optimization* (Springer-Verlag, New York, 1985), pp. 110-113.

26. L. E. Scales, *Introduction to Non-Linear Optimization* (Springer-Verlag, New York, 1985), pp. 56-51.

27. C. Holm, "Optical Thin Film Production with Continuous Reoptimization of Layer Thicknesses," Appl. Opt. **18,** 1978-1982 (1979).

28. T. E. Shoup and F. Mistree, *Optimization Methods with Applications to Personal Computers* (Springer-Verlag, New York, 1985), pp. 36-41.

29. J. A. Aguilera *et al.,*"Antireflection Coatings for Germanium IR Optics: A Comparison of Numerical Design Methods," Appl. Opt. **27,** 2832-2840 (1988).

30. T. E. Shoup and F. Mistree, *Optimization Methods with Applications to Personal Computers* (Springer-Verlag, New York, 1985), pp. 110-118.

31. M. J. D. Powell, "An Efficient Method for Finding the Minimum of a Function of Several Variables without Calculating Derivatives," Computer J. **7,** 155-162 (1964).

32. H. H. Rosenbrock, "An Automatic Method for Finding the Greatest or Least Value of a Function," Computer J. **7,** 308-313 (1964).

33. J. Stoer, *Introduction to Numerical Analysis* (Springer-Verlag, New York, 1980), pp. 195-197.

34. S. Kirkpatrick, C. D. Gellatt and M. P. Vecchi, "Optimization by Simulated Annealing," Science **220,** 671-680 (1984).

35. I. O. Bohachevsky, M. E. Johnson and M. L. Stein, "Generalized Simulated Annealing for Function Optimization," Technometrics **28,** 209-217 (1986).

36. A. V. Tikhonravov, M. K. Trubetskov, Brian T. Sullivan, and J. A. Dobrowolski, "Influence of small inhomogeneities on the spectral characteristics of single thin films," Appl. Opt. **36,** No. 28, 7188-7198 (1997).

37. Francesco Banfi, Vittorio Bellani, Ignacio Gomez, Enrique Diez and Francisco Dominguez-Adame, "Interface roughness effects in Gaussian superlattices," Semicond. Sci. Technol. **16,** 304-309 (2001).

38. H. C. Casey and M. B. Panish, *Heterostructure Lasers, Part A,: Fyndamental Principles.* Orlando: Academic Press, 1978.

39. M. A. Afromowitz, "Refractive index of $Al_xGa_{1-x}As$," Solid State Communications, vol. **15,** pp. 59-63, 1974.

40. S. Adachi, J. Appl. Phys. **66**, pp. 6030, 1989.

41. Y. Kokubo and I. Ohta, "Refractive index as a function of photon energy for AlGaAs between 1.2 and 1.8 eV," J. Appl. Phys. **81** (4), 15 February 1997.

42. Brian R. Bennett, Richard A. Soref, Jesus A. Del Alamo, "Carrier-Induced Change in Refractive Index of InP, GaAs, and InGaAsP," *IEEE J. Quantum Electron.*, vol. 26, No. 1, p. 113, 1990.

43. A. D. Yas'kov, "Influence of doping on the dispersion of the optical refractive index of semiconductors," *Sov. Phys. – Semicond.*, vol. 17, pp. 937-939, 1983.

44. L. P. Zverev, S. A. Negashev, V. V. Kruzhaev, and G. M. Min'kov, "Mechanism of band gap variation in heavily doped gallium arsenide," *Sov. Phys. – Semicond.*, vol. 11, pp. 603-605, 1977.

45. F. Stern, "Dispersion of the index of refraction near the absorption edge of semiconductors," *Phys. Rev. A*, vol. 133, pp. 1653-1664, 1964.

46. S. Adachi, "Material parameters of $In_{1-x}Ga_xAs_yP_{1-y}$ and related binaries," *J. Appl. Phys.*, vol. 53, pp. 8775-5792, 1982.

47. M. Ogura, T. Hata, and T. Yao, "Distributed feedback surface emitting laser diode with multilayered heterostructure," *Japan. J. Appl. Phys.*, vol. 23, pp. L512-L514, 1984.

48. K. Iga, F. Koyama, and S. Kinoshita, "Surface emitting semiconductor lasers," *IEEE J. Quantum Electron.*, vol. QE-24, pp. 1845-1855, Sept. 1988.

49. Mark Kuznetsov, Farhad Hakimi, Robert Sprague, and A. Mooradian, "Design and Characteristics of High-Power (>0.5-W CW) Diode-Pumped Vertical-External-Cavity Surface-Emitting Semiconductor Lasers with Circular $TEM_{00}$ Beams," *IEEE J. of Select. Top. in Quantum Electron.*, vol. 5, No. 3, 1999.

50. F. Krausz, T. Brabec, and C. Spielmann, "Self-starting passive mode locking," *Opt. Lett.*, vol. 16, p. 235, 1991.

51. H. A. Hauss and E. P. Ippen, "Self-starting of passively mode-locked lasers," *Opt. Lett.*, vol. 16, p. 1331, 1991.

52. H. A. Hauss, "Parameter ranges for CW passive mode locking," *IEEE J. Quantum Electron.*, vol. QE-12, p. 169, 1976.

53. Geoffrey H. C. New, "Pulse Evolution in Mode-Locked Quasi-Continuous Lasers," *IEEE J. Quantum Electron.*, vol. QE-10, No. 2, p. 115, 1974.

54. H. A. Haus, "Theory of mode locking with a fast saturable absorber," J. Appl. Phys., vol. 46, No. 7, p. 3049, 1975.

55. C. J. Chen, P. K. A. Wai, and C. R. Menyuk, "Self-starting of passively mode-locked lasers with fast saturable absorbers," *Opt. Lett.*, vol. 20, No. 4, p. 350, 1995.

56. J. Zehetner, CH. Spielmann, and F. Krausz, "Passive mode locking of homogeneously and inhomogeneously broadened lasers," *Opt. Lett.*, vol. 17, No. 12, p. 871, 1992.

57. H. A. Hauss, and Ping-Tong Ho, "Effect of Noise on Active Mode Locking of a Diode Laser," *IEEE J. Quantum Electron.*, vol. QE-15, No. 11, p. 1258, 1979.

58. E. P. Ippen, D. J. Eilenberger, and R. W. Dixon, "Picosecond pulse generation by passive mode locking of diode lasers," Appl. Phys. Lett. **37** (3), p. 267, 1980.

59. Y. Silberberg, P. W. Smith, D. J. Eilenberger, D. A. B. Miller, A. C. Gossard, W. Wiegmann, "Passive mode locking of a semiconductor diode laser," *Opt. Lett.*, vol. 9, No. 11, p. 507, 1984.

60. H. A. Haus, "Modelocking of Semiconductor Laser Diodes," JAPANESE JOURNAL OF APPLIED PHYSICS, Vol. 20, No. 6, pp. 1007-1020, 1981.

61. L. A. Kotomtseva, "Solid-State Laser with a Saturable Absorber Models for the Tunable Passive Loss Modulation and Mode-Locking Regimes," Laser Physics, Vol. 8, No. 1, pp. 254-258, 1998.

62. C. Hönninger, R. Pashotta, F. Mourier-Genoud, M. Moser, and U. Keller, "Q-switching stability limits of continuous-wave passive mode locking," J. Opt. Soc. Am. **B**, Vol. 16, No. 1, pp. 46-56, 1999.

63. H. A. Haus and Y. Silberberg, "Theory of mode locking of a laser diode with a multiple-quantum-well structure," J. Opt. Soc. Am. **B**, Vol. 2, No. 7, pp. 1237-1243, 1985.

64. Y. K. Chen, M. C. Wu, T. Tanbun-Ek, R. A. Logan and M. A. Chin, "Subpicosecond monolithic colliding-pulse mode-locked multiple quantum well laser," *Appl. Phys. Lett.*, **58**, p. 1253, 1991.

65. Ching-yue Wang, Lu Chai, Weili Zhang, and Kwong Mow Yoo, "Pulse colliding in a self-mode-locked ring-cavity Ti:sapphire lase," *Appl. Opt.*, vol. 37, No. 3, pp. 522-525, 1998.

66. Joaquim F. Martins-Filho, Eugene A. Avrutin, C. N. Ironside, and J. S. Roberts, "Monolithic Multiple Colliding Pulse Mode-Locked Quantum-Well Lasers," *IEEE J. of Select. Top. in Quantum Electron.*, vol. 1, No. 2, pp. 539-551, 1995.

67. E. P. Ippen, H. A. Haus, and L. Y. Liu, "Additive pulse mode locking," *J. Opt. Soc. Amer.* ***B,*** vol. 6, p. 1736, 1989.

68. E. P. Ippen, L. Y. Liu, and H. A. Haus, "Self-starting condition for additive-pulse mode-locked lasers," *Opt. Lett.*, vol. 15, p. 183, 1990.

69. H. A. Haus, J. G. Fujimoto, and E. P. Ippen, "Structures for additive pulse mode locking," *J. Opt. Soc. Amer.* ***B,*** vol. 8, p. 2068, 1991.

70. T. Brabec, F. Krausz, C. Spielmann, E. Wintner, and M. Budil, "Effects of dispersion in additive-pulse mode-locked lasers," *J. Opt. Soc. Amer.* ***B,*** vol. 8, p. 1818, 1991.

71. T. Brabec, C. Spielmann, P. F. Curley, and F. Krausz, "Kerr-lens mode locking," *Opt. Lett.*, vol. 17, 1992.

72. S. Chen and J. Wang, "Self-starting issues of passive self-focusing mode locking," *Opt. Lett.*, vol. 16, p. 1689, 1991.

73. T. Brabec, C. Spielmann, and F. Krausz, "Mode locking in solitary lasers," *Opt. Lett.*, vol. 16, p. 1961, 1991.

74. T. Brabec, C. Spielmann, and F. Krausz, "Limits of pulse shortening in solitary lasers," *Opt. Lett.*, vol. 17, p. 748, 1992.

75. M. Krijn, G. W. `t Hooft, M. J. B. Boermans, P. J. A. Thijs, T. van Dongen, J. J. M. Binsma, L. F. Tiemeijer, and C. J. van der Poel, "Improved performance of compressively as well as tensile strained quantum-well lasers," *Appl. Phys. Lett.* Vol. 61, pp. 1772-1774, 1992.

76. D. Ahn and S. L. Chuang, "Optical gain in strained-layer quantum well lasers," *IEEE J. Quantum Electron.*, vol. 24, pp. 2400-2406, 1988.

77. T. J. Andersson, Z. G. Chen, V. D. Kulakovski, A. Uddin, and J. T. Vallin, "Variation of the critical layer thickness with In content in strained InGaAs-GaAs quantum wells grown by molecular beam epitaxy," *Appl. Phys. Lett.* Vol. 51, pp. 752-754, 1987.

78. M. C. P. M. Krijn, "Heterojunction band offsets and effective masses in III-V quaternary alloys," *Semiconduct. Sci. Technol.*, vol. 6, pp. 27-32, 1991.

79. A. R. Adams, "Band-structure engineering for low threshold high efficiency semiconductor lasers," *Electron. Lett.*, vol. 22, pp. 249-250, 1986.

80. W. Streifer, D. R. Scifres, and R. D. Burnham, "Optical analysis of multiple-quantum-well lasers," *Appl. Opt.*, vol. 18, pp. 3547-3548, 1979.

# CHAPTER III
# SUPERLATTICE-BASED SATURABLE ABSORBER MIRRORS (SUSAM's)

## CH.III. 1. Introduction

There has been a great deal of interest recently in optical switching devices that can operate at picosecond speeds and at low optical powers. In order for such devices to find practical applications, however, it is necessary for the design to be simple, reliable, and compact. Significant progress has been made using group III-V semiconductors. In these devices, optical interactions take place inside the nonlinear medium where a strong optical field induces a nonlinear change in the optical properties of the material. The material is optically nonlinear in the sense that the value of its refractive index and/or absorption coefficient has intensity dependent characteristics. Then optical switching can be achieved by using a suitable device structure in which the nonlinear refractive index and/or absorption coefficient results in switching of the signal that passes through it. Optical switching can be achieved for both the transmitted and the reflected power. The device operating in the reflection mode and where the switching mainly depends on the absorption changes in the active layer has recently been named as saturable absorber mirror. It is more practical and therefore the whole attention will be addressed in this chapter to saturable absorber mirrors.

There are several physical mechanisms that can bring about changes in optical properties of a semiconductor material. One mechanism of optical nonlinearity is band-filling and exciton bleaching that occurs at optical energies near the band gap energy.[1,2] In this case, photocarrier generation due to one or two photon absorption results in changes in absorption spectrum and a corresponding change in the refractive index. Another method is the application of a dc electric field to sweep out the photogenerated carriers from the effective nonlinear region.[3] While the above mentioned effects are due to the generation of real carriers, another mechanism that results in a refractive index change is the Kerr nonlinearity for photon energies below one half the band gap energy.[4] In this case, the effect is instantaneous but requires very high optical intensities to cause switching. Additionally, the high intensities required for switching result in multi-photon absorption

and the creation of free carriers. Yet another mechanism for optical nonlinearity is the optical or ac Stark effect in semiconductors.[5-11] In this case, electric field component of the optical wave interacts with the exciton levels in somewhat of a similar manner to the ac Stark effect of two-level atoms whereby a shift or splitting of the levels occur. The optical Stark effect that occurs in quantum wells when the excitation is detuned away from resonance is a consequence of virtual excitation of excitons. The anharmonic behavior of the exciton-photon, exciton-phonon and exciton-exciton interactions causes nonlinearities that depend directly on the density of virtual excitons. The nonlinear mechanisms are quite complex, but the net effect is a blue shifting of the exciton. The main disadvantage of the optical Stark effect is that the nonlinearity exhibit a strong wavelength and polarization dependence.

In general, an ideal saturable absorber mirror device should have ultrafast switching speeds, low insertion losses, wavelength-independent, polarization-independent absorption characteristics if necessary. A number of technologies have been used to fulfill these requirements including low-temperature molecular beam epitaxy (LT-MBE)[8-12], metal-organic chemical-vapor deposition (MOCVD), ion-implantation[13-16]. However any technology has characteristic features and their application is limited. Therefore this chapter describes design principles and characteristic features of technologies used to manufacture saturable absorbers. The key point of this chapter is to introduce a novel design of saturable absorber mirror that has been manufactured using only MOCVD growth. The design, characteristics and possible improvements are discussed as well.

## CH.III. 2. Ideal Saturable Absorber Mirror Performance

The general structure of a saturable absorber mirror is shown in Fig.CH.III.2. 1. It is composed of a pair of mirrors, high-reflectivity back mirror ($R_B$) and a low-reflectivity front mirror ($R_F$), that are separated by a space layer with absorbing QWs. The position of QWs in a space layer is an important design parameter. The incident and reflected light forms a standing-wave pattern. Since the QW is very thin relative to the wavelength of light in the device, it can be placed anywhere relative to intensity. This field overlap determines the effective saturation intensity of the structure. Since we would like to

achieve a wide-bandwidth, it is advantageous to design QWs operating above band gap to have large absorption changes. A few QWs of different alloy composition can be used to increase bandwidth. $R_B$ should be as close to unity as possible, and $R_F$ is chosen to optimize saturable absorber mirror performance either for maximum reflection change or maximum contrast.

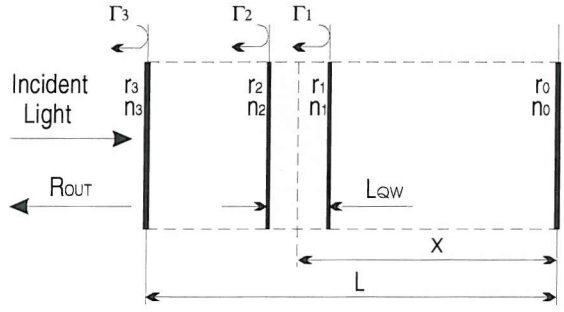


**Fig. CH.III. 2. 1:** General saturable absorber mirror structure. Here $L$ is the length of the cavity, $L_{QW}$ is the QW geometrical thickness, $x$ is the QW position in the device, $\alpha_{QW}$ is the QW absorption coefficient which is actually wavelength dependent, $n_0$, $n_1$, $n_2$, $n_3$ are refractive indexes, and $r_0$, $r_1$, $r_2$, $r_3$ are interface amplitude field reflectivities.

The device output is the reflection which may be derived using tanh substitution technique. Then, assuming symbols used in Fig.CH.III. 2. 1., the optical amplitude reflectivities at a boundaries are given by

$$\Gamma_1(\lambda, x, L_{QW}) = \frac{|r_1| + |r_0| \exp\left[-i2\frac{2\pi}{\lambda} n_0 (x - L_{QW}/2)\right]}{1 + |r_1||r_0| \exp\left[-i2\frac{2\pi}{\lambda} n_0 (x - L_{QW}/2)\right]}, \qquad \text{[CH.III. 2/1]}$$

$$\Gamma_2(\lambda, x, L_{QW}) = -\frac{\left|\frac{n_1 - n_0}{n_1 + n_0}\right| + |\Gamma_1(\lambda, x, L_{QW})| \exp\left[-i2\frac{2\pi}{\lambda} n_1 L_{QW}\right] \exp\left[-A_{eff}(\lambda, x, L_{QW})\right]}{1 + \left|\frac{n_1 - n_0}{n_1 + n_0}\right| |\Gamma_1(\lambda, x, L_{QW})| \exp\left[-i2\frac{2\pi}{\lambda} n_1 L_{QW}\right] \exp\left[-A_{eff}(\lambda, x, L_{QW})\right]},$$

$$\Gamma_3(\lambda, x, L_{QW}) = \frac{|r_3| + |\Gamma_2(\lambda, x, L_{QW})| \exp\left[-i2\frac{2\pi}{\lambda} n_2 (L - x - L_{QW}/2)\right]}{1 + |r_3||\Gamma_2(\lambda, x, L_{QW})| \exp\left[-i2\frac{2\pi}{\lambda} n_2 (L - x - L_{QW}/2)\right]},$$

where the effective integrated absorption coefficient

$$A_{eff}(\lambda, x, L_{QW}) = 2\alpha_{QW} \int_{x-\frac{L_{QW}}{2}}^{x+\frac{L_{QW}}{2}} \left[1 + \cos\left(2\frac{2\pi}{\lambda} n_1 x\right)\right] dx . \qquad \text{[CH.III. 2/2]}$$

The intensity reflection takes the form:

$$R_{OUT}(\lambda, x, L_{QW}) = |\Gamma_3(\lambda, x, L_{QW})|^2 . \qquad \text{[CH.III. 2/3]}$$

Here $\lambda$ is the free-space wavelength of the standing wave optical field, $L$ is the length of the cavity, $L_{QW}$ is the QW geometrical thickness, $x$ is the QW position in the device, $\alpha_{QW}$ is the QW absorption coefficient which is actually wavelength dependent, $n_0$, $n_1$, $n_2$, $n_3$ are refractive indexes, and $r_0$, $r_1$, $r_2$, $r_3$ are interface optical field reflectivities. The interface reflectivities $r_0$ and $r_3$ can be both wavelength dependent. This is usually the case of saturable absorber mirrors. Since the QW active medium is nonuniform, the spatial overlap integral [CH.III. 2/2] between the standing-wave optical field in the device and the position of the absorbing QW is of primary interest. The possible phase shift available on reflections and/or in the QW can be taken into account by simply inserting it into exponential brackets using the equations CH.III. 2/1. In case of more than one QW specific equations must be derived similarly as CH.III. 2/1. It follows that optimization of the overlap integral between standing-wave optical field and QW's at a specific design wavelength is extremely important.

The maximum reflection from the device can be achieved when the round-trip phase shift is an odd integer multiple of $\pi$ (antiresonance condition). The locations of these maxima are at wavelengths

$$\lambda_q = 4n(\lambda_q)L/q , \qquad \text{[CH.III. 2/4]}$$

where $q = 1,3,5,7,...$ is an odd integer.

Conversely, the minimum reflection is achieved when the round-trip phase shift is an even integer multiple of $\pi$ (resonance condition). The locations of the minima are also given by [CH.III. 2/4] but, in this case, parameter $q$ is an even integer. The wavelength difference

between two adjacent minima or maxima, referred to as the free spectral range (FSR), can be calculated by

$$FSR = \Delta\lambda = \lambda^2 / (2n(\lambda)L). \qquad \text{[CH.III. 2/5]}$$

FSR bandwidth for the anti-resonant device is determined by the separation of the maxima.

Below are shown results of calculated reflectivity as a function of QW width, QW position in the device and wavelength assuming that QW absorption is wavelength independent, top surface of device has 30% of reflectivity and bottom mirror is either wavelength independent or typical distributed Bragg reflector (DBR) mirror.

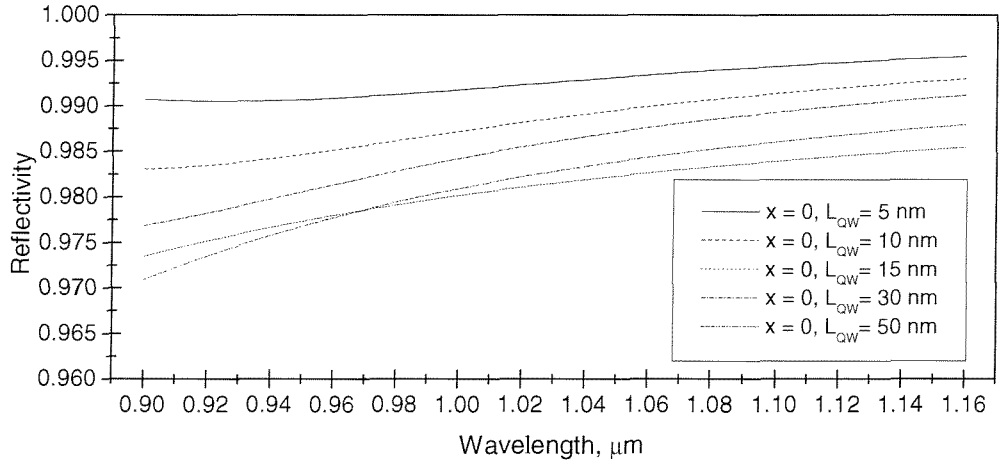


**Fig. CH.III. 2. 2:** Computed reflectivity of saturable absorber mirror containing the absorbing QW as a function of wavelength and different QW widths at a constant $x = 0$ QW position. Device optical thickness is equal to 1.03/4 μm.

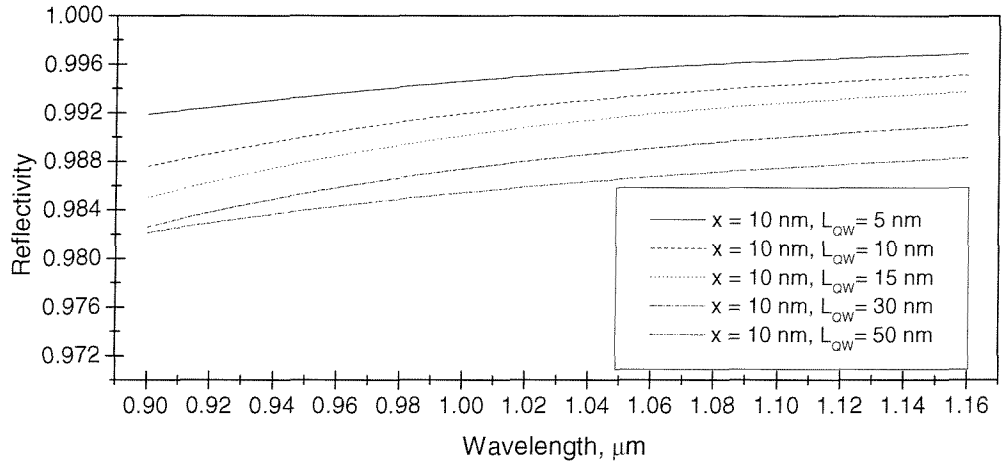


**Fig. CH.III. 2. 3:** Computed reflectivity of saturable absorber mirror containing the absorbing QW as a function of wavelength and different QW widths at a constant $x = 10$ nm QW position. Device optical thickness is equal to 1.03/4 μm.

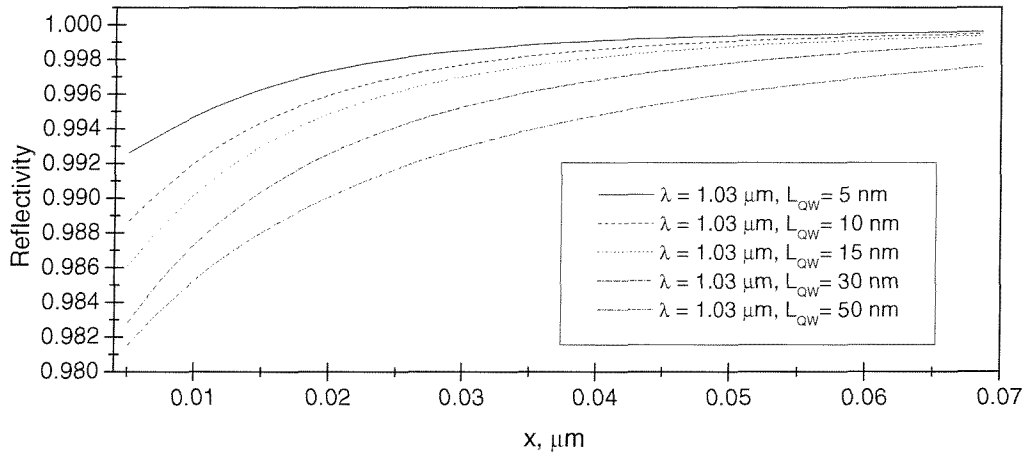


**Fig. CH.III. 2. 4:** Computed reflectivity of saturable absorber mirror containing the absorbing QW as a function of QW position for different QW widths at a wavelength $\lambda = 1.03$ μm. Device optical thickness is equal to 1.03/4 μm.

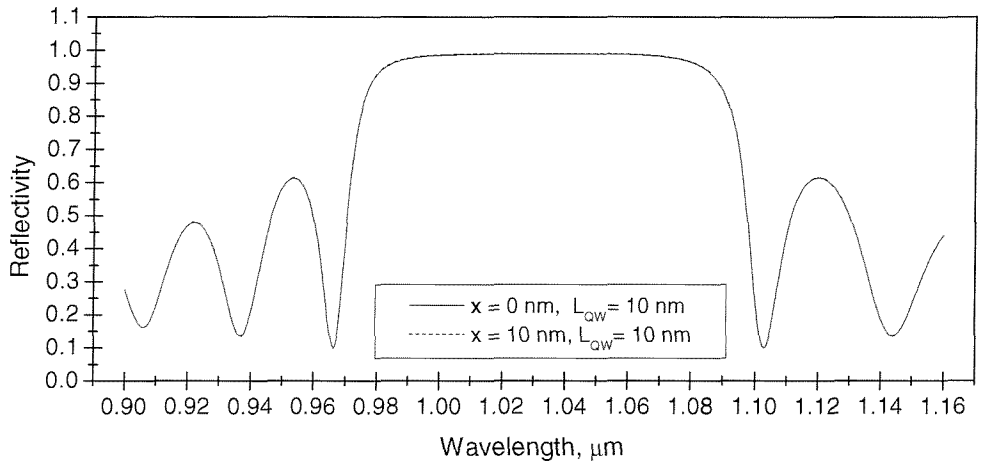


**Fig. CH.III. 2. 5:** Computed reflectivity of saturable absorber mirror containing the absorbing QW and DBR back mirror as a function of wavelength for two different QW positions. Device optical thickness between mirrors is equal to 1.03/4 μm.

Figures CH.III. 2. 2. and CH.III. 2. 3. show reflection spectrum of saturable absorber mirror for different QW widths and positions, assuming that QW absorption, front and back mirror reflectivities are wavelength independent. Calculations show that reflectivity decreases with increasing QW width. Fig. CH.III. 2. 4. shows calculated reflectivity as a function QW position and assuming different QW widths. Reflectivity decreases shifting QW from its antinode position. Fig. CH.III. 2. 5. shows reflection spectrum using same QW width and assuming that back mirror is typical 25 period DBR. There is a small difference in reflection spectrum that can not been seen in Fig. CH.III. 2. 5. for a small 10 nm QW shift.

In general refractive index and absorption coefficient both can be wavelength, intensity, polarization, temperature dependent functions. These characteristics can be considered in designing the saturable absorber device if necessary.

## CH.III. 3. Absorption Recovery in Saturable Absorber Mirrors

Absorption recovery of semiconductor saturable absorbers is an important characteristic in applications such as passive mode locking and ultra-fast optical switching. The absorption recovery is related to carrier recombination processes in absorbing QW's and therefore carrier recombination lifetime is of primary interest. In general carrier recombination mechanism is related to defects such as chemical impurities, mechanical defects, and grain boundaries in many of the most common semiconductors. It can be shown that the carrier recombination rate at low and high injection levels is a function of the defect electron and hole capture cross-sections. It is also a function of the defect energy levels in the forbidden band gap or that lie near band gap. Therefore full analysis is very complex. Some work has been done using models involving multiple trapping of free carriers in spatially localized subband gap states having various energy distributions (exponential, Gaussian, linear, etc.).[17] This analysis has been especially useful for amorphous or polycrystalline semiconductors. A method based on the Orenstein and Kastner model (referenced to as the OK model), has been developed for an exponential distribution of localized energy states.[18] However, the experimental data showed some inconsistencies with this model. The more flexible method based on numerical solution of multiple trapping rate equations that involves complex algorithms to solve the high degree polynomial equation.[19] Therefore it is obvious that full analysis is very complex requiring large experimental data for a better fit to final model. Very specific and sensitive carrier lifetime spectroscopy techniques can be used for qualitative and quantitative analysis. For a simplicity and quantitative analysis the total lifetime may be expressed using the law of the addition of reciprocal lifetimes

$$\frac{1}{\tau_{TOTAL}} = \left[\frac{1}{\tau_B} + \frac{1}{\tau_S}\right]_D + \left[BN + C_A N^2\right] + \left[\frac{1}{\tau_{LD}}\right], \qquad \text{[CH.III. 3/1]}$$

and

$$\frac{1}{\tau_{TOTAL}} = \left[\frac{1}{\tau_B} + \frac{2S}{d}\right]_D + \left[BN + C_A N^2\right] + \left[\frac{8D}{w_0^2}\right]. \qquad \text{[CH.III. 3/2]}$$

Here $\tau_B$ is the recombination lifetime component (bulk defects); $B$ is the radiative coefficient; $C_A$ is the Auger coefficient; $N$ is the total free carrier density (doping produced

carriers plus injected carriers); $\tau_S$ is the recombination lifetime component (surface defects); $S$ is a surface recombination velocity; $d$ is distance from the surface; $\tau_{LD}$ is the carrier diffusion lifetime component (lateral carrier diffusion); $D$ is diffusion coefficient; $w0^2$ - the Gaussian-beam waist. The recombination lifetime is expressed as a combination of three terms. The first term is responsible for defects. In general defects can be separated into surface and bulk defects. The surface component can be written in terms of surface recombination velocity $S$, as is seen in first brackets of [CH.III. 3/1] and [CH.III. 3/2] equations. The next term is responsible for material properties. The radiative coefficient (or $B$ coefficient) and the Auger coefficient $C_A$ are specific to a given semiconductor. The Auger effect is a dominant recombination mechanism for highly doped semiconductors. The last term is responsible for carrier diffusion processes. In the case of a passively mode locked laser, the intracavity optical field is usually tightly focused into a small QW region of saturable absorber mirror. In this case carriers may diffuse laterally out of the interaction region in times comparable with or even shorter than the recombination lifetimes. The diffusion lifetime $\tau_{LD}$ is a characteristic time, not an exponential lifetime. Note that reducing absorption recovery time increase the saturation intensity of the saturable absorber, but does not necessarily affect the absorption cross section. There have been several techniques used for shortening the absorption recovery time of saturable absorbers. One involves InGaAs based devices grown at low temperatures by molecular beam epitaxy (MBE). LT-BME growth results in very poor crystalline quality of these materials. Critical growth conditions such as temperature and annealing regime determine the final absorption recovery characteristics. The purpose of annealing is to eliminate shallow traps, which may anneal spontaneously, and thus stops degradation of characteristics, ensure better long-term stability for grown samples. Fig. CH.III. 3. 1. shows typical characteristics of saturable absorber mirrors achieved by using LT-MBE technology.

**Table. CH.III. 3. 1:** Measured SESAM's parameters.[12]

| SESAM's (Growth Method) | Saturation Fluence, ($\mu J/cm^2$) | Modulation Depth, (%) | Nonsaturable Loss, (%) | Recovery Time, (ps) |
|---|---|---|---|---|
| 1QW of 25-nm InGaAs (MBE) | 100±20 | 0.9 | 0.4 | 4 |
| 1QW of 25-nm InGaAs (MBE) | 80±10 | 1.0 | 0.6 | 9 |
| 2QW's of 10-nm InGaAs (MBE) | 45±5 | 1.2 | 0.4 | 14 |
| 1QW of 25-nm InGaAs (MBE) | 65±10 | 1.3 | 0.5 | 40 |

Fig. CH.III. 3. 1. shows measured absorption recovery temporal characteristics as a function of MBE growth temperature.

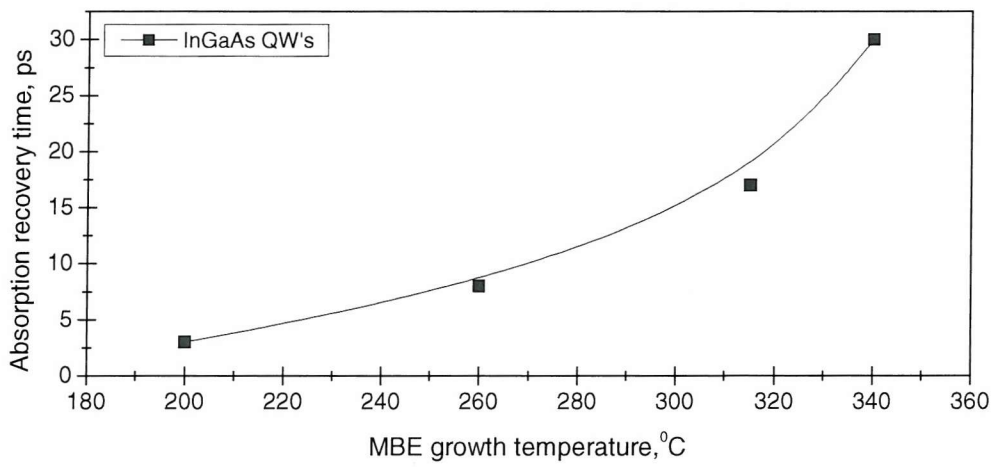


**Fig. CH.III. 3. 1:** Measured absorption recovery time as a function of MBE growth temperature for InGaAs QWs.[12]

It is evident from these results that the lower the growth temperature, the faster the absorption recovery of QWs. In principle these results could vary using different MBE

techniques and growth regimes. After annealing (annealing temperature and duration are very specific and critical), any post-growth processing is very limited. Post-growth introduces undesirable losses in the final device, modifies lifetime characteristics. In addition, for low insertion loss saturable absorbers no post-growth is recommended after LT-MBE material has been grown. This is one of the shortcomings of LT-MBE method in reducing saturable absorption recovery. The other method for shortening absorption recovery time is a controlled damaging of the structure by ion-implantation, proton bombardment. This is an alternative to LT materials. It is well established that ion-implantation, or proton bombardment increases carrier recombination rate by generating damage centers, which serve as recombination sites. This has been verified with a variety of different ions, proton doses, and semiconductor materials.[15] Fig. CH.III. 3. 2. shows the measured absorption recovery lifetime for different proton doses in annealed and unannealed $Al_{0.29}Ga_{0.71}As$/GaAs QW samples.

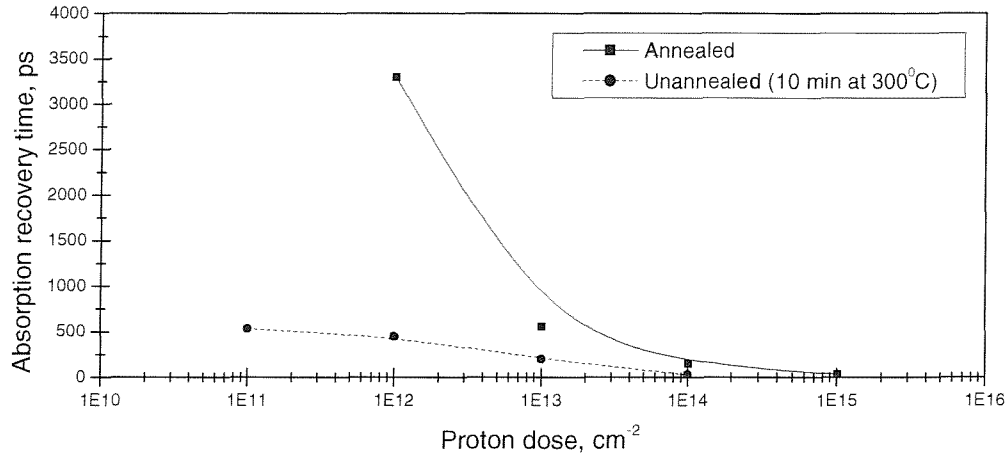


**Fig. CH.III. 3. 2:** Measured absorption recovery time as a function of proton dose for annealed and unannealed 10.1/8 nm $Al_{0.29}Ga_{0.71}As$/GaAs MQW samples. Proton energy – 200 keV.[13]

It is evident that annealing is very critical even using a gentle 10 min LT ($300^0$C) annealing regime. It has been demonstrated that not only the concentration of defects but also the nature of defects is important. Defects such as point defects, defect clusters, dislocation loops and polycrystalline material determine different contributions to the shortening of the recovery times. It was established that point defects are the main cause

of reduction in recovery times, since the formation of dislocation loops and defect clusters consumes point defects. If damaging doses are too high this leads to amorphization, poor recrystallization, and polycrystalline material after annealing. The polycrystals usually tend to increase the carrier lifetimes. As a result high damaging doses should be avoided under these conditions.

In general, all the effects that disturb crystalline structure of a semiconductor can generally be expected to shorten the absorption recovery characteristics. Therefore there should be many ways of doing it. The most interesting are those that involve magnetically-active, electrically-active defects.

## CH.III. 4. Novel Design of Superlattice-Based Saturable Absorber Mirror

During the past several years, various groups of researchers have used intracavity quantum-well-based semiconductor saturable absorbers to mode-lock solid-state and semiconductor lasers including Ti:sapphire, Cr:LiSAF, Cr:YAG, Nd:$YVO_4$, Nd:YLF, Yb:YAG, OP-VECSEL.[20-28] Mostly these devices used QWs grown by molecular beam epitaxy (MBE) at low growth temperatures to achieve short decay times. AlGaAs-based device designs have been limited by low refractive index contrast and the reflection at air-semiconductor boundary was dominant. Therefore some designs incorporated additional dielectrics ($SiO_2$ / $TiO_2$) making them most promising for intra-cavity broadband feedback with prescribed phase properties or AlGaAs distributed Bragg reflectors were replaced by silver mirrors. Unfortunately the fabrication of such structures became a quite complex and long process, that required post-growth chemical etching procedures. Also there is a possibility in increase of non-saturable losses during chemical etching and silver deposition procedures. MOCVD grown QW structures typically have long decay times because of high standard growth temperatures. Typically normal MOCVD growth temperatures lead to very low non-saturable losses. The shortening of decay times can be achieved by additionally using ion-implantation or surface recombination processes placing absorbing layers close to the semiconductor-air interface. However, in this case any post-growth processing to modify the whole device is impossible due to annealing. Therefore one wants to have very simply manufacturable saturable absorber devices.

In this section we introduce a novel superlattice-based design of saturable absorber mirror (SUSAM), grown by metal-organic chemical-vapor deposition (MOCVD) under standard conditions, in which a strained superlattice, adjacent to the absorbing quantum well is expected to produce sufficiently rapid absorption recovery necessary to passively mode-lock diode pumped external cavity surface emitting laser (DP-VECSEL). The concept of strain-induced shortening of absorption recovery is offering promises of improved performance. We demonstrate that our structure requires only a single MOCVD growth and there is no any need of post-growth and chemical etching processes. The use of single technology is very promising for low undesirable loss devices. There are three slightly different designs of SUSAM's that are going to be discussed. The conduction band diagram of the general I-type SUSAM stucture is shown in Fig. III. 4. 1.

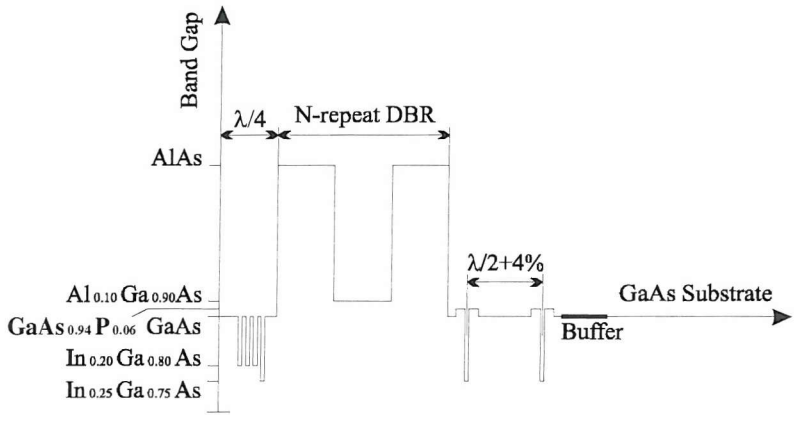


**Fig. CH.III. 4. 1:** Conduction Band Diagram of Superlattice-based Saturable Absorber Mirror (SUSAM, I-type). DBR is Distributed Bragg Reflector.

The entire I-type SUSAM structure can be represented as Substrate | 2H B-2QW L $(HL)^N$ A-QW-A | Air, where H and L corresponds to quarter-wavelength layers of high (H-$Al_{0.10}Ga_{0.90}As$, $n$=3.433) and low (L-AlAs, $n$=2.944) refractive index materials. SUSAM can be grown by metal organic chemical vapor deposition (MOCVD) at normal growth temperatures on a 0.5-mm-thick un-doped GaAs wafer oriented $3^0$ from the (100) toward the (110) plane. A thick $Al_{0.10}Ga_{0.90}As$ buffer layer is used to improve crystalline structure that must be grown upon GaAs substrate. Then two strain-balanced quantum wells follow the buffer layer and have the following structure: GaAs spacer 24-nm barrier $GaAs_{0.94}P_{0.06}$

well-10 nm $In_{0.27}Ga_{0.73}As$ 24-nm barrier $GaAs_{0.94}P_{0.06}$ GaAs spacer 24-nm barrier $GaAs_{0.94}P_{0.06}$ well-10 nm $In_{0.27}Ga_{0.73}As$ 24-nm barrier $GaAs_{0.94}P_{0.06}$ GaAs spacer, so the total thickness between QWs is equal to $\lambda/2+4\%$ of a 1.03 μm half-wave layer. The 4% opposite shift is necessary to reduce sensitivity to optical field shift against QW position due to growth errors. In general back QWs are designed to decrease weak but dominant Fabry-Perot modulation due to substrate in that way technologically simplifying packaging procedures. In general Fabry-Perot effects due to substrate are met if even small fraction of light is transmitted through the distributed Bragg reflector, which then interfere with reflected back from the substrate light part already weakened by the possible losses in the substrate.

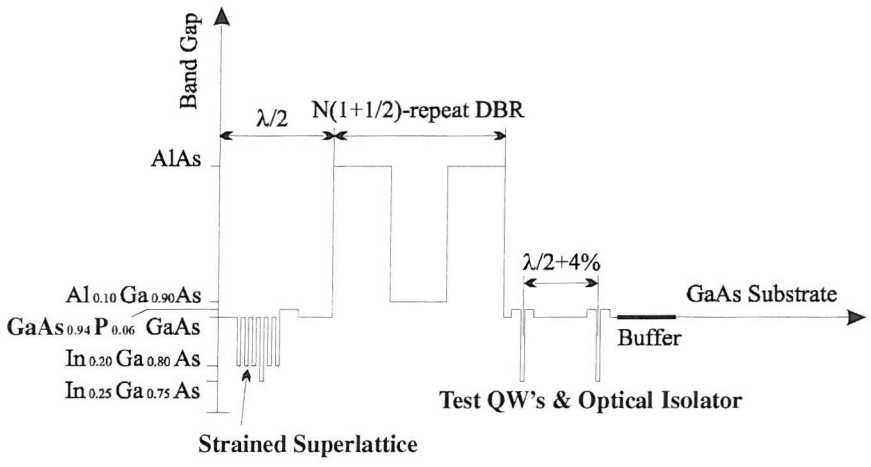


**Fig. CH.III. 4. 2:** Conduction Band Diagram of Superlattice-based Saturable Absorber Mirror (SUSAM, II-type). DBR is Distributed Bragg Reflector.

In general, any additional loss mechanism in the substrate is quite original, efficient and technologically simple way to avoid undesirable spectral modulation given by light interference from the substrate. QWs in the substrate are also of great importance for calibration of lifetime characteristics of front fast QW with back QWs that are grown under normal strain-balanced conditions. The calibration of lifetime characteristics if necessary can be related to QW photoluminescence measurements. The use of back QWs could be not efficient as expected in case of relatively large phase changes introduced due to entire structure errors. The use of strong absorption mechanism at the device-substrate

interface is strongly recommended because of more accurate definition of boundary conditions. The next two designs of SUSAM show improvements related to strain balancing effects. Fig. III. 4. 2. shows the conduction band diagram of the II-type SUSAM stucture. Any strain will tend to propagate deep into mirror by creating undesirable losses and imperfections. Therefore the local high-strain region introduced by superlattice around front QW should be compensated or stopped to keep high quality entire structure. This can be achieved by introducing $GaAs_{0.94}P_{0.06}$ layer of variable thickness depending on the integrated strain. The II-type SUSAM design is also anti-resonant at the design wavelength as I-type SUSAM design. To keep anti-resonant conditions in the second design the first layer is set equal to $\lambda/2$ and then $N(1+1/2)$ repeat DBR. Third type design of SUSAM includes AR coating region as illustrated in Fig. III. 4. 3.

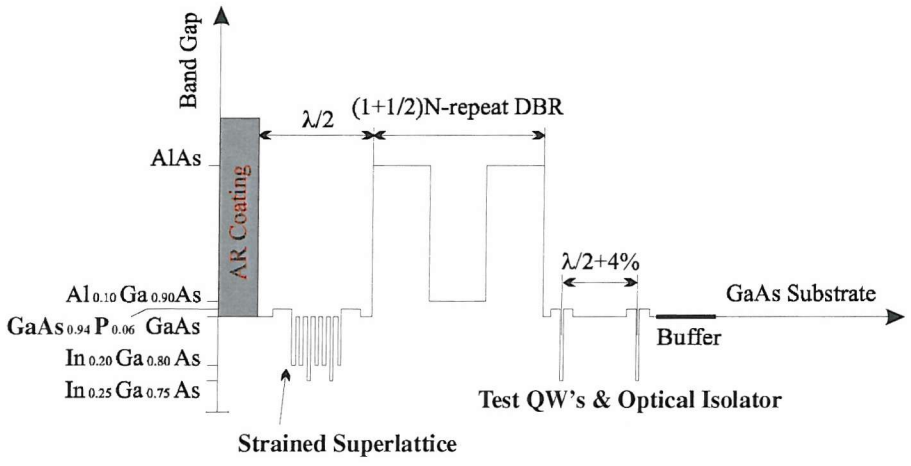


**Fig. CH.III. 4. 3:** Conduction Band Diagram of Superlattice-based Saturable Absorber Mirror (SUSAM, III-type). DBR is Distributed Bragg Reflector.

In case of any integration of AR coating strain introduced by superlattice must be compensated and on other side. The positions of QWs must be refined in any case as well. Strain induced effects to shorten absorption recovery characteristics are believed to be wavelength independent. Integrated AR region usually reduces effective saturation fluence of the device and increases modulation depth using the same QW thickness and relative position with respect to optical field. All designs with specific AR coatings have to be refined to optimize device performance in the region of specific wavelength interests. So

the main idea to design SUSAM is to integrate strained superlattice in the effective QW region and then to compensate it for the entire device.

In general, all SUSAM designs could be described that have loss component below the mirror to avoid undesirable interference effects from the substrate, then follows mirror, absorbing QWs inserted or adjacent to the strained superlattice to decrease absorption recovery characteristics, and finally AR coating if it is necessary to increase modulation depth and to compensate for high order dispersion. Highly strained superlattice region should be isolated to prevent strain propagation deep into other parts of the device. This allows to have the whole device growth more simply avoiding complex post-growth procedures.

Below are shown some characteristics of a few SUSAM designs. DBR's with 26, 26.5 periods of $Al_{0.10}Ga_{0.90}As$/AlAs quarter-wave layers for 1.03 μm are designed to have reflectivity of ~99.9% and over greater than 70-nm wavelength bandwidth. The integration of QWs below the distributed Bragg reflector (DBR) inserts ~2% loss for light transmitted through DBR. The position of the saturable absorber layer inside the structure is an important design parameter therefore we placed the saturable absorber layer close to the field maximum location, such that effective saturation fluence of the device is reduced. Integrated QWs are designed to have a maximum absorption at 1.04 μm. Then the average ~0.7% modulation depth at 1.03 μm is expected to be sufficient to achieve self-starting passive mode-locking.

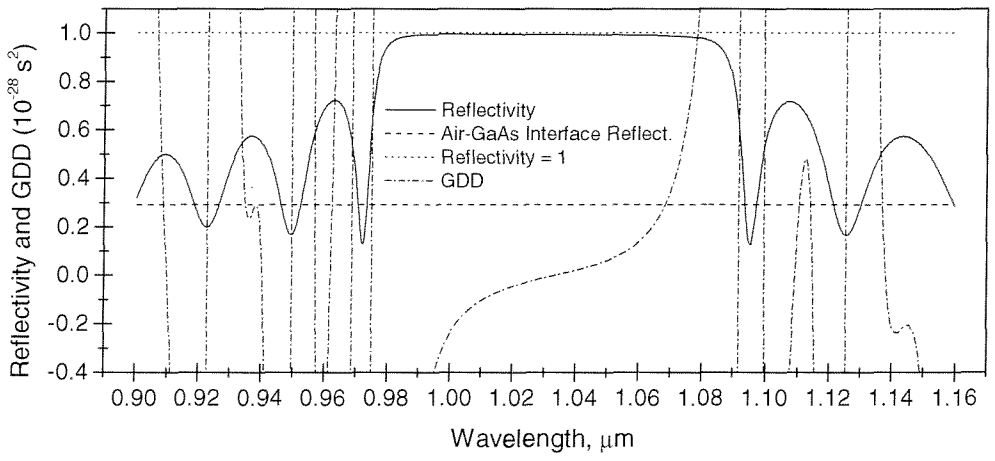


**Fig. CH.III. 4. 4:** Computed reflectivity and GDD as a function of wavelength of I-type SUSAM. Structure formula: 64S □ LC [HL]$^{27}$ 0.204H 0.13L$_{qw}$ [0.095H 0.091L$_s$]$^3$ 0.109H □ 1.0; ($\lambda_0 = 1.03$ μm, $n_L(AlAs) = 2.94$, $n_{Ls}(In_{0.20}Ga_{0.80}As) = 3.342$, $n_{Lqw}(In_{0.25}Ga_{0.75}As) = 3.344$ $n_H(Al_{0.1}Ga_{0.9}As) = 3.433$, $n_S(GaAs) = 3.496$), LC – loss component. I-type SUSAM design has nonlinear GDD characteristics.

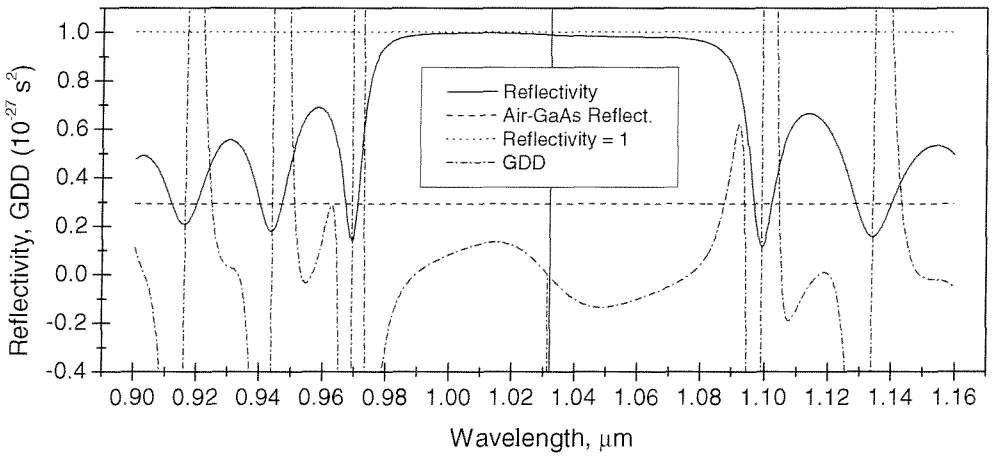


**Fig. CH.III. 4. 5:** Computed reflectivity and GDD as a function of wavelength of II-type SUSAM. Structure formula: 65S □ LC L $[HL]^{27}$ 0.754H $0.13L_{qw}$ $[0.095H\ 0.091L_s]^3$ 0.559H □ 1.0; ($\lambda_0 = 1.03$ μm, $n_L(AlAs) = 2.94$, $n_{Ls}(In_{0.20}Ga_{0.80}As) = 3.342$, $n_{Lqw}(In_{0.25}Ga_{0.75}As) = 3.344$, $n_H(Al_{0.1}Ga_{0.9}As) = 3.433$, $n_S(GaAs) = 3.496$), LC – loss component. II-type SUSAM design has nonlinear GDD characteristics. Strained superlattice changes GDD characteristics.

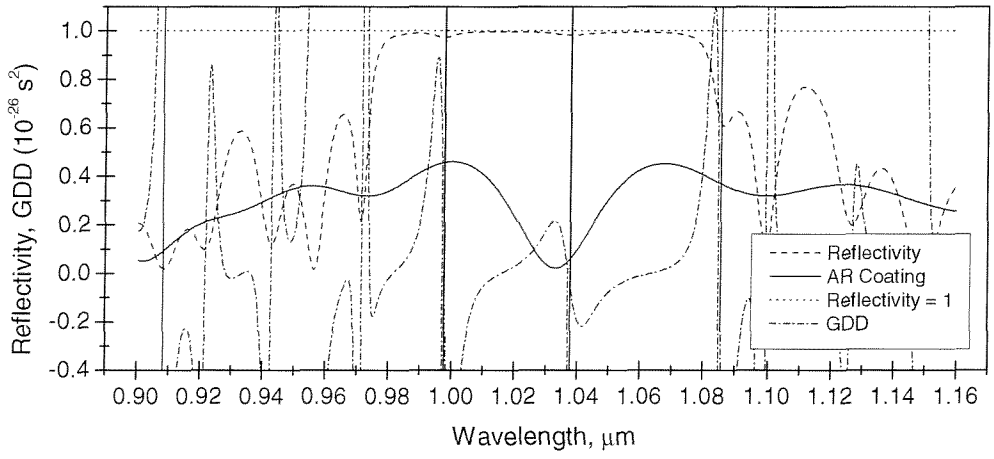


**Fig. CH.III. 4. 6:** Computed reflectivity, AR coating and GDD as a function of wavelength of III-type SUSAM. Structure formula: 72S □ LC L [HL]$^{27}$ (0.537H 0.13L$_{qw}$ [0.095H 0.091L$_s$]$^3$ 0.109H) (9.023L 3.002H 9.023L 3.002H 3.012L 6.018H 6.023L) □ 1.0; ($\lambda_0 = 1.03$ μm, $n_L(AlAs) = 2.94$, $n_{Ls}(In_{0.20}Ga_{0.80}As) = 3.342$, $n_{Lqw}(In_{0.25}Ga_{0.75}As) = 3.344$, $n_H(Al_{0.1}Ga_{0.9}As) = 3.433$, $n_S(GaAs) = 3.496$), LC – loss component. Narrow-band AR coating introduces an additional modulation into GDD characteristics.

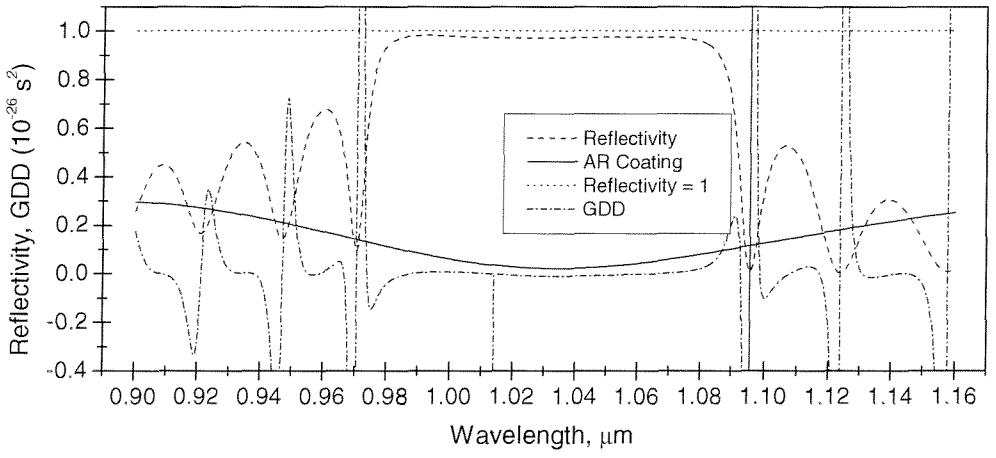


**Fig. CH.III. 4. 7:** Computed reflectivity, AR coating and GDD as a function of wavelength of III-type SUSAM. Structure formula: 72S □ LC L $[HL]^{27}$ (0.204H 0.13$L_{qw}$ $[0.095H\ 0.091L_s]^3$ 0.109H) (0.584L 0.681H 1.753L $[0.681H\ 1.168L]^2$) □ 1.0; ($\lambda_0 = 1.03$ μm, $n_L(AlAs) = 2.94$, $n_{Ls}(In_{0.20}Ga_{0.80}As) = 3.342$, $n_{Lqw}(In_{0.25}Ga_{0.75}As) = 3.344$, $n_H(Al_{0.1}Ga_{0.9}As) = 3.433$, $n_S(GaAs) = 3.496$), LC – loss component. Broad-band AR coating helps to achieve linear GDD characteristics (GDD is linear in the spectral region exceeding ~40 nm).

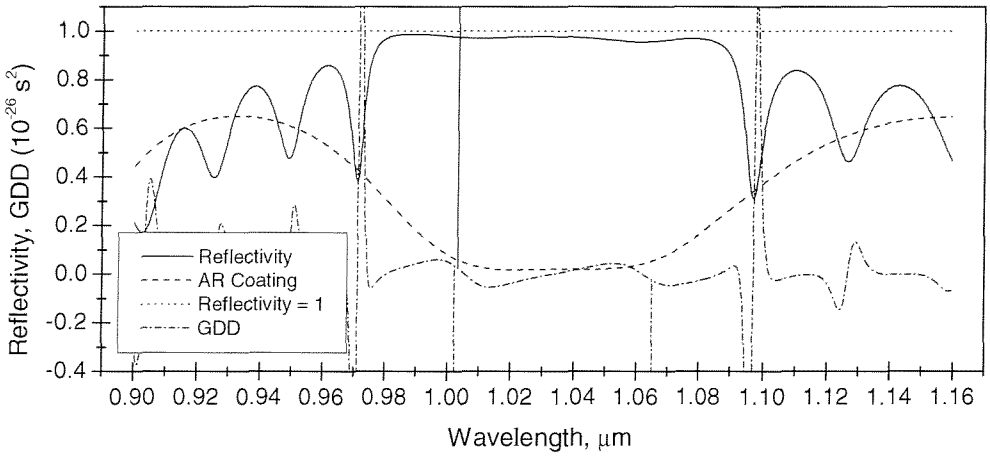


**Fig. CH.III. 4. 8:** Computed reflectivity, AR coating and GDD as a function of wavelength of III-type SUSAM. Structure formula: 77S □ LC L $[HL]^{27}$ (0.204H 0.13$L_{qw}$ $[0.095H\ 0.091L_s]^3$ 0.109H) (L 1.005H 4.022L $[1.005H\ L]^2$ 1.005H 3.01L 1.005H L 2.01H) □ 1.0; ($\lambda_0 = 1.03$ μm, $n_L(AlAs) = 2.94$, $n_{Ls}(In_{0.20}Ga_{0.80}As) = 3.342$, $n_{Lqw}(In_{0.25}Ga_{0.75}As) = 3.344$, $n_H(Al_{0.1}Ga_{0.9}As) = 3.433$, $n_S(GaAs) = 3.496$), LC – loss component.

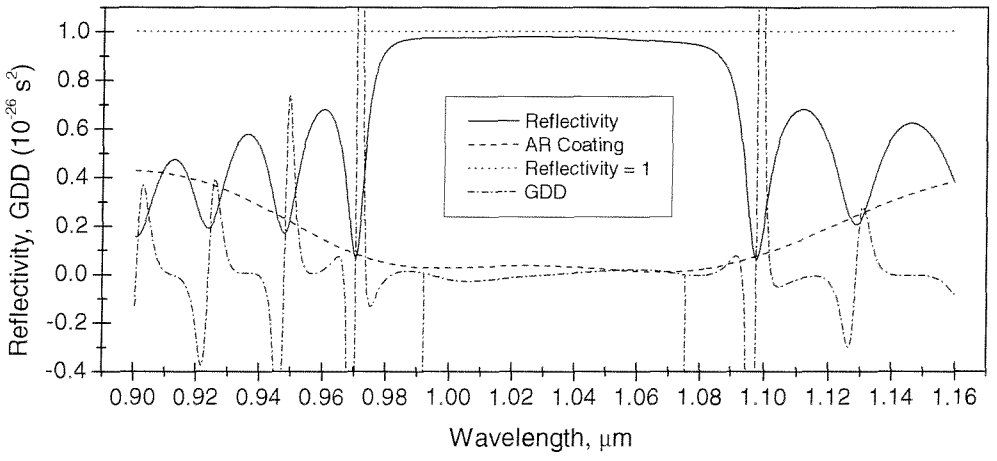


**Fig. CH.III. 4. 9:** Computed reflectivity, AR coating and GDD as a function of wavelength of III-type SUSAM. Structure formula: 74S □ LC L [HL]$^{27}$ (0.204H 0.13L$_{qw}$ [0.095H 0.091L$_s$]$^3$ 0.109H) (1.212L 5.832H 0.945L [1.083H 0.945L]$^3$) □ 1.0; ($\lambda_0 = 1.03$ μm, $n_L(AlAs) = 2.94$, $n_{Ls}(In_{0.20}Ga_{0.80}As) = 3.342$, $n_{Lqw}(In_{0.25}Ga_{0.75}As) = 3.344$, $n_H(Al_{0.1}Ga_{0.9}As) = 3.433$, $n_S(GaAs) = 3.496$), LC – loss component.

Calculations indicate that SUSAM's with no AR coating typically have modulation depth around 1%. Air-semiconductor interface reflects around 30% of incident radiation what increase energy saturation fluence of the device. Any AR coating increase optical field amplitude at the QW position what outomatically increase and modulation depth. SUSAM's with AR coating typically have up to a few percent modulation depth. The SUSAM design that is shown in Fig. CH.III. 4. 9. is particularly intresting. The broad-band AR coating design matches DBR mirror band and GDD is almost linear over 70 nm region.

## CH.III. 5. References


1. H. M. Gibbs, S. L. McCall, T. N. C. Venkatesan, A. C. Grossard, A. Pasner, and W. Wiegmann, "Optical bistability in semiconductors," *Appl. Phys. Lett.*, vol. 35, pp. 451-453, 1979.
2. G. D. Boyd, D. A. B. Miller, S. D. Chemla, S. L. McCall, A. C. Gossard, and J. H. English, "Multiple quantum well reflection modulator," *Appl. Phys. Lett.*, vol. 50, pp. 1119-1121, 1987.
3. T. H. Wood, C. A. Burrus, D. A. B. Miller, D. S. Chemla, T. C. Damen, A. C. Gossard, and W. Wiegmann, "High-speed optical modulation with GaAs/GaAlAs quantum wells in a p-i-n diode structure," *Appl. Phys. Lett.*, vol. 44, pp. 16-18, 1984.
4. G. Stegman, A. Villeneuve, J. Kang, J. S. Aitchison, C. N. Ironside, K. Al-Hemyari, C. C. Yang, C. H. Lin, H. H. Lin, G. T. Kennedy, R. S. Grant, and W. Sibbett, "AlGaAs below half bandgap: The silicon of nonlinear optical materials," *Int. J. Nonlinear Opt. Phys.*, vol. 3, pp. 47-371, 1994.
5. P. W. Smith, Y. Silberberg, and D. A. B. Miller, "Mode locking of semiconductor diode lasers using saturable excitonic nonlinearities," *J. Opt. Soc. Amer.* ***B,*** vol. 2, pp. 1228-1236, 1985.
6. D. S. Chemla, W. H. Knox, D. A. B. Miller, S. Schmitt-Rink, J. B. Stark, and R. Zimmermann, "The excitonic optical Stark effect in semiconductor quantum wells probed with femtosecond optical pulses," *J. Luminescence*, vol. 44, pp. 223-246, 1989.
7. A. Mysyrowicz, D. Hulin, A. Antonetti, A. Migus, W. T. Masselink, and H. Morkoc, "Dressed excitons in a multiple-quantum-well structure: Evidence for an optical stark effect with femtosecond response time," *Phys. Rev. Lett.*, vol.56, no. 25, pp. 2748-2751, 1986.
8. S. Gupta, M. Y. Frankel, J. A. Valdmanis, J. F. Whitaker, G. A. Mourou, F. W. Smith, and A. R. Calawa, "Subpicosecond carrier lifetime in GaAs grown by molecular beam epitaxy at low substrate temperatures," *Appl. Phys. Lett.*, vol. 59, pp. 3276-3278, 1991.

9. R. Takahashi, W.-Y. Choi, Y. Kawamura, and H. Iwamura, "Femtosecond all-optical AND gates based on low-temperature-grown Be-doped strained InGaAs/InAlAs MQW's," in *LEOS 95 Proc.* Vol. 1, p. 343, 1995.

10. M. Kaminska, Z. Liliental-Weber, E. R. Weber, T. George, J. B. Kortright, F. W. Smith, B. Y. Tsaur, and A. R. Calawa, "Structural properties of As-rich GaAs grown by molecular beam epitaxy at low temperatures," *Appl. Phys. Lett.*, vol. 54, pp. 1881-1883, 1989.

11. X. Liu, A. Prasard, J. Nishio, E. R. Weber, Z. Liliental-Weber, and W. Walukiewicz, "Native point defects in low-temperature-grown GaAs," *Appl. Phys. Lett.*, vol. 67, pp. 279-281, 1995.

12. C. Honninger, R. Paschotta, F. Morier-Genoud, M. Moser, U. Keller, "Q-switching stability limits of continuous-wave passive mode-locking," *J. Opt. Soc. Amer.* ***B,*** vol. 16. No 1, pp. 46, /January 1999.

13. P. W. Smith, Y. Silberberg, D. A. B. Miller, "Mode locking of semiconductor diode lasers using saturable excitonic nonlinearities," J. Opt. Soc. Am. **B,** vol. 2, No. 7, pp. 1228-1236, 1985.

14. A. Krotkus, S. Marcinkevicius, J. Jasinski, M. Kaminska, H. H. Tan, and C. Jagadish, *Appl. Phys. Lett.*, vol. 66, p. 3304, 1995.

15. H. H. Tan, C. Jagadish, K. P. Korona, J. Jasinski, M. Kaminska, R. Viselga, S. Marcinkevicius, and A. Krotkus, IEEE J. Sel. Top. Quantum Electron. **2,** p. 630, 1996.

16. C. Jagadish, H. H. Tan, J. Jasinski, M. Kaminska, M. Palczewska, A. Krotkus, and S. Marcinkevicius, *Appl. Phys. Lett.*, vol. 67, p. 1724, 1995.

17. J. Orenstein and M. A. Kastner, "Photocurrent Transient Spectroscopy: Measurement of the Density of Localized States in *a* $As_2Se_3$," *Phys. Rev. Lett.*, vol. 46, Nr. 21, p. 1421-1424, 1981.

18. S. Grabtchak and M. Cocivera, "Behavior of photoconductivity transients due to multiple trapping by a Gaussian distribution of localized states," *Phys. Rev. B*, vol. 60, p. 10997-11004, 1999.

19. G. Seynhaeve, G. J. Adriaenssens, and H. Michiel, "On the density of localized states obtainable from transient photodecay measurements," *Solid State Commun.*, vol. 56, p. 323-326, 1985.

20. Zhigang Zhang, Tadashi Nakagawa, Hideyuki Takada, Kenji Torizuka, Takeyoshi Sugaya, Taisuke Miura, Katsuyuki Kobayashi, "Low-loss broadband semiconductor saturable absorber mirror for mode-locked Ti:sapphire lasers," *Opt. Commun.* 176 (2000) 171-175.

21. Sérgio Tsuda, Wayne H. Knox, S. T. Cundiff, W. Y. Jan, and J. E. Cunningham, "Mode-Locking Ultrafast Solid-State Lasers with Saturable Bragg Reflectors," *IEEE*, vol. 2, No. 3. September 1996.

22. D. Kopf, G. Zhang, R. Fluck, M. Moser, and U. Keller, "All-in-one dispersion-compensating saturable absorber mirror for compact femtosecond laser sources," *Opt. Lett.*, vol. 21, pp. 486-488,1996.

23. S. Tsuda, W. H. Knox, E. A. de Souza, W. Y. Jan, and J. E. Cunningham, "Low-loss intracavity AlAs/AlGaAs saturable Bragg reflector for femtosecond mode locking in solid-state lasers," *Opt. Lett.*, vol. 20, pp. 1406-1408, 1995.

24. U. Keller, T. H. Chiu, and J. F. Ferguson, "Self-starting and self-Q-switching dynamics of passively mode-locked Nd:YLF and Nd:YAG lasers, " *Opt. Lett.*, vol. 18, pp. 217-219, 1993.

25. R. Paschotta, J. Aus der Au, G. J. Spühler, F. Mourier-Genoud, R. Hövel, M. Moser, S. Erhard, M. Karszewski, A. Giesen, U. Keller, " Diode-pumped passively mode-locked lasers with high average power," *Appl. Phys. B* (2000).

26. C. Hönninger, G. Zhang, A. Giesen, and U. Keller, "Femtosecond Yb:YAG laser using semiconductor saturable absorbers," *Opt. Lett.*, vol. 20, pp. 2402-2404, 1995.

27. S. Hoogland, S. Dhanjal, A. C. Tropper, *Member, IEEE,* J. S. Roberts, R. Häring, R. Paschotta, F. Morier-Genoud, and U. Keller, "Passively Mode-Locked Diode-Pumped Surface-Emitting Semiconductor Laser," *IEEE Photon. Technol. Lett.*, vol. 12, pp. 1135-1137, 2000.

28. A. Garnache, S. Hoogland, K. Vyšniauskas, P. Suret, V. Thierry-Mieg, and A. C. Tropper, "Broadband high power sub-picosecond diode-pumped passively mode-locked external-cavity surface-emitting laser at 328 MHz," *Opt. Lett.*, to be published.

# CHAPTER IV
# EXPERIMENTS

## CH.IV. 1. Introduction

The optical characterization and ultra-short pulse CW mode-locked operation of DP-VECSEL laser using novel design of saturable absorber mirrors (SUSAMs) is the main object of this chapter. Optical characterization experiments are performed using as grown wafers taken directly from growth chamber without additional processing. Optical characterization methods that have been used in this work are non-contact and non-destructive involving reflection and/or transmission spectrum measurements, photoluminescence spectrum measurements, and pump-probe experiments. These methods are relatively simple and ensure rapid post-growth analysis of grown samples. The second part of this chapter is focused on ultra-short pulse DP-VECSELs, and passive mode-locking results are discussed. The CW and CW mode-locking results are achieved using the same external cavity. The additional experiments were performed to disclose problems associated with instabilities that appear in ultra-short pulse DP-VECSELs under specific circumstances. Experiments suggest final considerations that are necessary to accomplish optimization of ultra-short pulse DP-VECSELs, and to avoid undesirable instabilities.

## CH.IV. 2. Reflection and Transmision Measurements

Reflection or transmission measurements are non-destructive characterization method suitable for semiconductor wafer investigation, or wafer-mapping. The reflection spectrum of a bulk undoped semiconductor material is generally broad with no pronounced features, even at energies corresponding to critical points of its band structure. In contrast, SUSAM or DP-VECSEL structures yield high reflectivity stop bands and many subsidiary interference peaks and troughs. These devices are complex multi-layer structures whose operating characteristics are highly sensitive to variations in layer thickness and material composition. However, these variations in layer thicknesses and composition, either through the entire device structure or across the plane of the wafer, have a significant effect on the shape of the spectrum. Such variations may be responsible for many of the difficulties in successfully fabricating DBRs, SUSAMs, DP-VECSELs with the required device characteristics. Regions of the wafer suitable for producing operating devices can be found by on-wafer characterization, prior to device further investigation, and if necessary processing.

Here the transmission or reflection spectra measurements were made on all suitable wafers using Perkin-Elmer spectrometer. The wafers were mounted on a stage that allowed to rotate and to translate samples. This method was chosen to keep central symmetry. Measurements were made at an angle of incidence of $0^0$ over a wavelength range from 800 to 1200 nm. This range covers several prominent interference features in the device spectrum, including part of the main stop band. The spectrometer slits were set at 2.0 giving a spot area on the sample of approximately 5 $mm^2$, and resolution (FWHM) of ~2.0 nm in the wavelength range studied. All samples were mapped across their surface rotating them from $0^0$ to $360^0$ and at four radius distances from the wafer centre, including 5 mm, 10 mm, 15 mm, 20 mm as is shown in Fig. CH.IV. 2. 1. In order to display the degree of variation observed in these spectral measurements, for each given wafer, two curves are shown. One shows the variation of design wavelength across the wafer. The second one shows a measured reflectivity spectrum that is typical for that device. In order to simplify this section all grown samples are described by using growth code number and device formula, and are specified in appendix A. Here only results of two grown I-type SUSAMs (with two- and three-repeat strained superlattice) are presented. SUSAM devices

were grown using single-step non-rotational metal-organic chemical-vapor deposition (MOCVD under standard growth conditions. Two wafers, the "up-sample" and the "down-sample", were placed side by side in MOCVD growth chamber, at the same growth time. Therefore results are shown here for both up and down wafers.

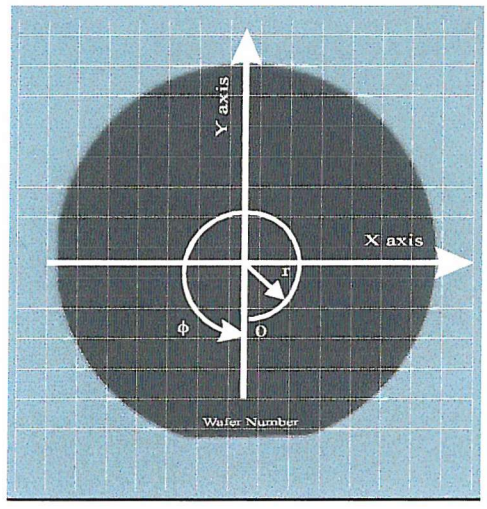


**Fig. CH.IV. 2. 1:** Map of the wafer to co-ordinate system used during the transmission or reflection spectra measurements. Here $r$ is radius, and $\Phi$ is angle of wafer rotation. The wafers were mounted on a stage that allowed to rotate and to translate samples.

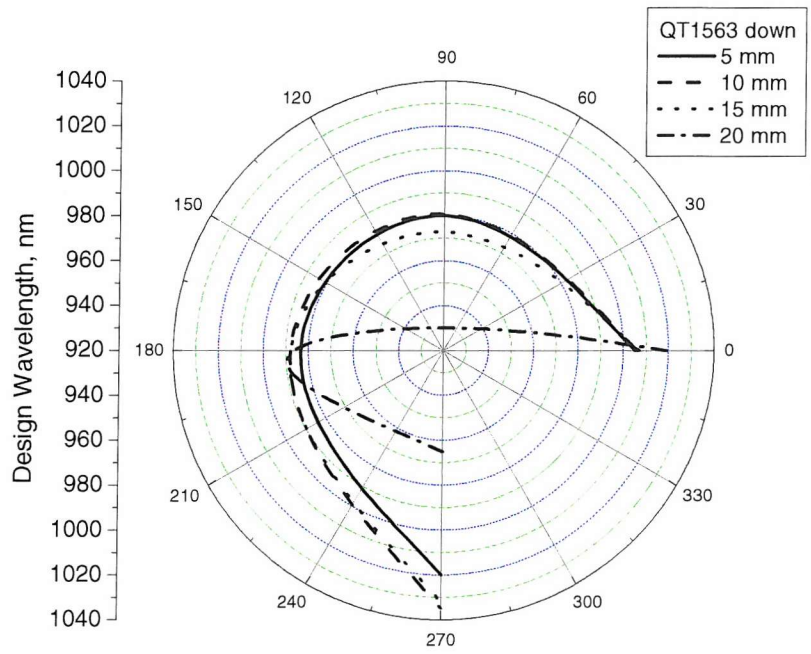


**Fig. CH.IV. 2. 2:** Experimentally measured design wavelength shift in the reflection spectrum across QT1563-down wafer (I-type SUSAM with 2-repeat strained GaAs-$In_{0.2}Ga_{0.8}As$ superlattice, Ingot Number Down-WV 2067.019/Un, (100) $3^0 \rightarrow$ (110) $\alpha = 45^0$).

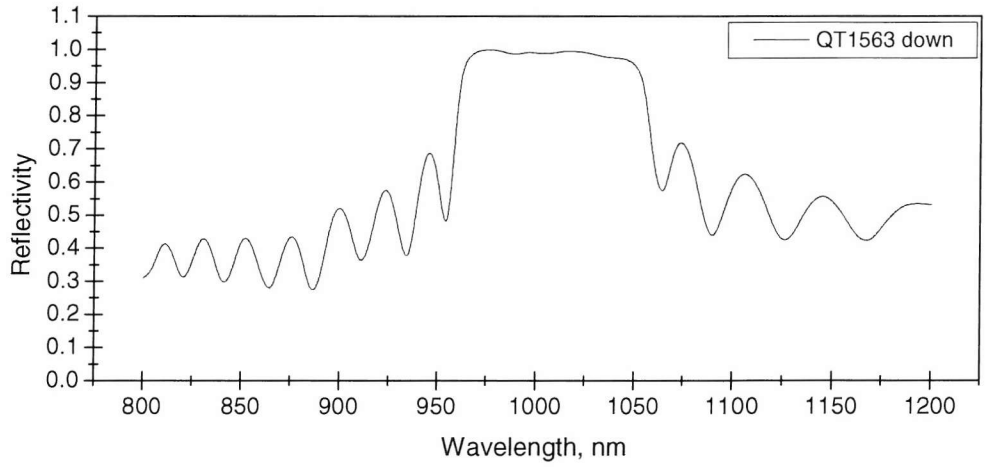


**Fig. CH.IV. 2. 3:** Experimentally measured the reflection spectrum taken at one point on QT1563-down wafer (I-type SUSAM with 2-repeat strained GaAs-$In_{0.2}Ga_{0.8}As$ superlattice, Ingot Number Down-WV 2067.019/Un, (100) $3^0 \rightarrow$ (110) $\alpha = 45^0$).

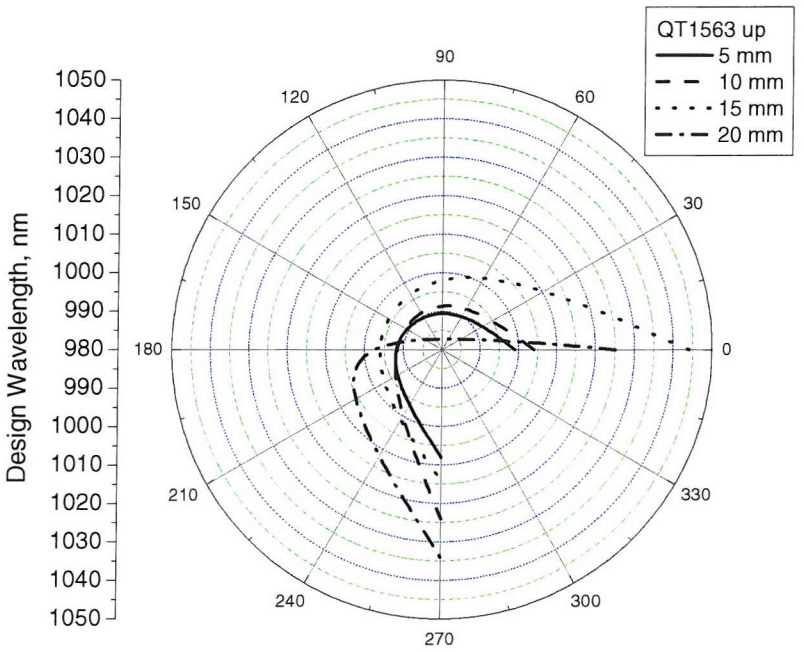


**Fig. CH.IV. 2. 4:** Experimentally measured design wavelength shift in the reflection spectrum across QT1563-up wafer (I-type SUSAM with 2-repeat strained GaAs-$In_{0.2}Ga_{0.8}As$ superlattice, Ingot Number Up-WV 2067.008/Un, (100) $3^0 \rightarrow$ (110) $\alpha = 45^0$).

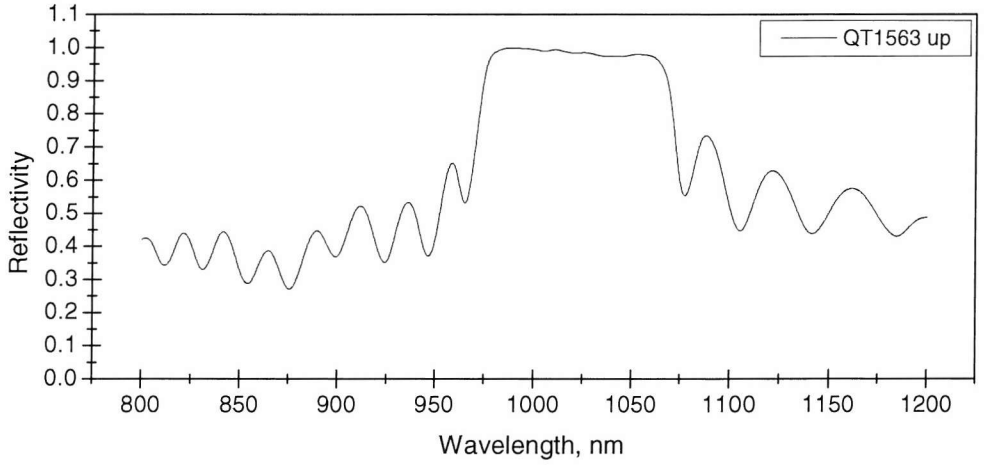


**Fig. CH.IV. 2. 5:** Experimentally measured the reflection spectrum taken at one point on QT1563-up wafer (I-type SUSAM with 2-repeat strained GaAs-$In_{0.2}Ga_{0.8}As$ superlattice, Ingot Number Up-WV 2067.008/Un, (100) $3^0 \rightarrow$ (110) $\alpha = 45^0$).

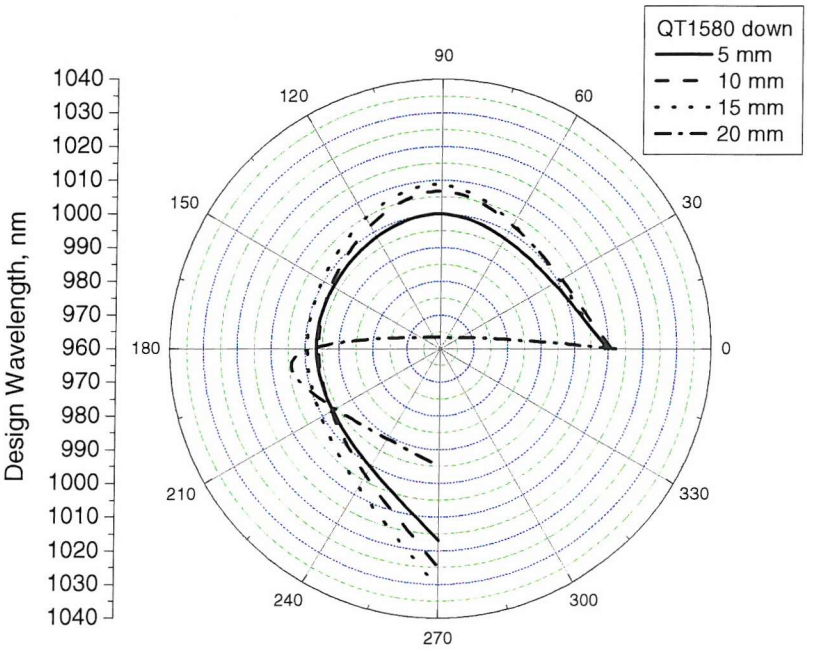


**Fig. CH.IV. 2. 6:** Experimentally measured design wavelength shift in the reflection spectrum across QT1580-down wafer (I-type SUSAM with 3-repeat strained GaAs-$In_{0.2}Ga_{0.8}As$ superlattice, Ingot Number Down-WV 2067.001/Un, (100) $3^0 \rightarrow$ (110) $\alpha = 45^0$).

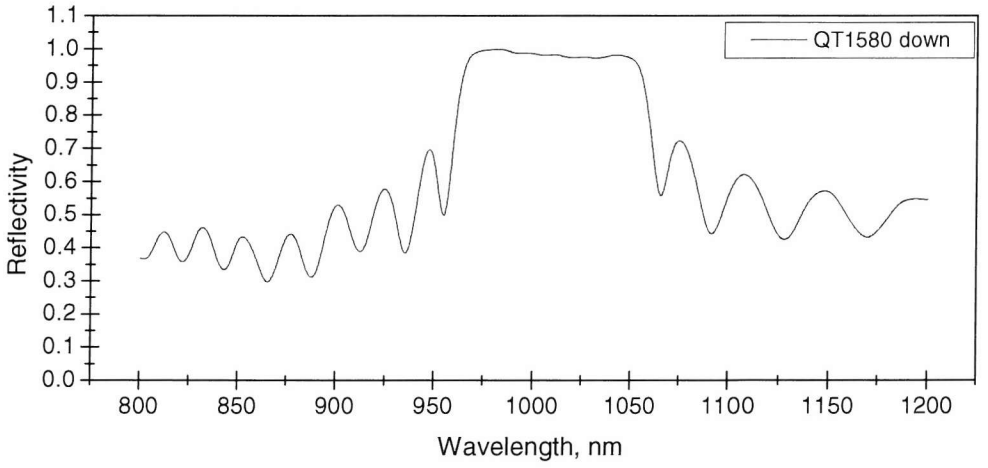


**Fig. CH.IV. 2. 7:** Experimentally measured the reflection spectrum taken at one point on QT1580-down wafer (I-type SUSAM with 3-repeat strained GaAs-$In_{0.2}Ga_{0.8}As$ superlattice, Ingot Number Down-WV 2067.001/Un, (100) $3^0 \rightarrow$ (110) $\alpha = 45^0$).

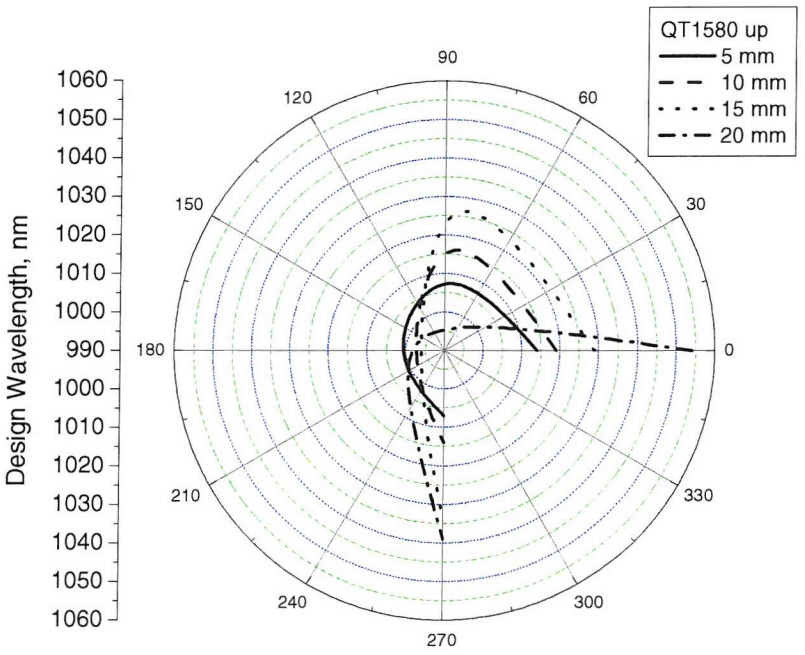


**Fig. CH.IV. 2. 8:** Experimentally measured design wavelength shift in the reflection spectrum across QT1580-up wafer (I-type SUSAM with 3-repeat strained GaAs-$In_{0.2}Ga_{0.8}As$ superlattice, Ingot Number Up-WV 2067.003/Un, (100) $3^0 \rightarrow$ (110) $\alpha = 45^0$).

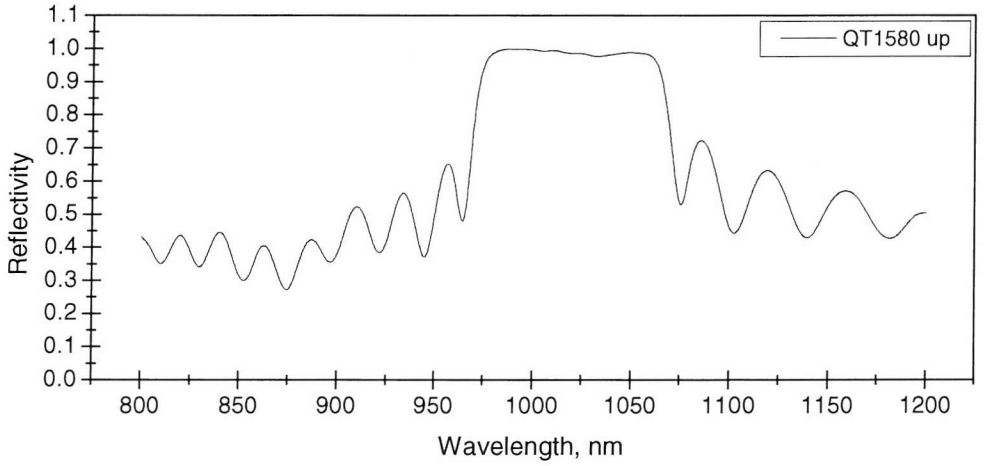


**Fig. CH.IV. 2. 9:** Experimentally measured the reflection spectrum taken at one point on QT1580-up wafer (I-type SUSAM with 3-repeat strained GaAs-$In_{0.2}Ga_{0.8}As$ superlattice, Ingot Number Up-WV 2067.003/Un, (100) $3^0 \rightarrow$ (110) $\alpha = 45^0$).

Clearly, the variations in layer thickness across the wafers result in an overall shift of design wavelength reaching up to 80 nm in specific cases. Lateral diagrams that show variations in spectral characteristic are individual in each wafer growth case indicating considerable non-uniformity. This usually complicates development of devices. SUSAM samples designed to have integrated strained superlattice have shown perfect growth with very small amount of surface defects. It was established that SUSAMs have modulation depth approximately equal to 0.7% centered near 1.04 μm. However, specific design of DP-VECSEL growth was unsuccessful (QT1656 and QT1677 wafers, see appendix A). Therefore DP-VECSEL that is much simple was used (QT1462 wafer, see appendix A). Unsuccessful DP-VECSEL samples were having remarkable surface degradation with very complex combination of surface defects. These samples were designed to have strain-balanced structure, but unfortunately high density of crater-like surface defects have shown growth problems associated with balancing the growth reaction. It seems that grown samples were still degrading over some period of time.

## CH.IV. 3. Pump-Probe Experiments

The pump-probe method is a well known optical measurement technique for the determination of absorption recovery times in the picosecond and nanosecond scale. In the conventional pump-probe technique, test sample is excited using two short pulses (pump and probe). Typically short intense pump pulse enters the sample followed by a much weaker short probe pulse whose arrival time can be adjusted using a variable delay line. This measurement technique is based upon nonlinearity in the luminescence spectra from the sample resulting from a recombination of the carriers. Only changes in reflected intensity originating from the presence of the carriers generated by the probe pulse with those generated by the pump pulse is detected. The duration of both pulses must be short compared with the relevant time constants of the sample, and the probe pulse should contain negligible energy so that is does not itself perturb the system. Here a pump-probe setup is described that was used to measure lifetime absorption recovery characteristics of SUSAMs.

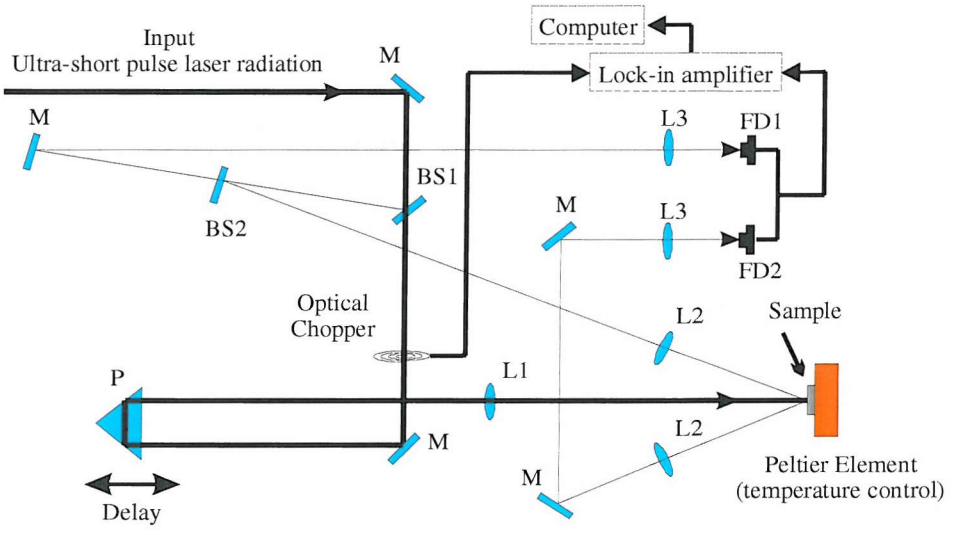


**Fig. CH.IV. 3. 1:** The pump-probe experimental setup. M – HR mirror, BS1 – 30/70 beam splitter, BS2 – 50/50 beam splitter, P – prism, L1, L2, L3 – lenses, FD – photo diodes. The balancing photo-detector (FD1 and FD2 photodiodes), lock-in amplifier and computer are used to record data.

The experimental pump-probe setup is shown in Fig. CH.IV. 3. 1. The laser source used in pump-probe experiments is an ultrashort pulse DP-VECSEL operating at 330 MHz repetition rate and generating 5 ps long pulses (FWHM) at 1035 nm. The optical pulse train is split at a beam splitter (BS1) in two beams of unequal intensity, 70% for pump branch and 30% for probe branch. Beam splitting ratio could be changed to 10/90 by angular adjustment of the beam splitter. The pump beam is modulated using an optical chopper at 300 Hz, and passes through an optical delay line consisting of a mirror (M), prism (P) and focusing lens L1. The probe beam is split at a beam splitter (BS2) into two beams of approximately equal intensity. The probe beam is directed to photo-diode (FD1) through passing an optical system consisting of mirror (M) and focusing lens (L3). The second probe beam is directed through focusing lens (L2) to test sample. The reflected beam from the sample is collected by using the second lens (L2) and is directed though two HR mirrors (M) and lens (L3) to photo diode (FD2).

Two photo diodes form balancing photo detection system that measures only difference in intensity on two photo detectors. This is necessary to avoid undesirable laser emission fluctuations. If intensities on both photo diodes are equal, then balancing signal is equal to zero. The balancing photo detector measures only the signal that is induced by the pump pulse. With the actual configuration used, the probe spot area on the sample was chosen approximately four times smaller than the pump spot area to ensure spatial alignment on the sample. The linearity of the delay system was checked replacing the sample with a HR mirror. The delay line was chosen in the pump branch rather in the probe avoiding undesirable spatial probe beam fluctuations on the small area photo diodes. By varying the delay between pump and probe, the temporal absorption recovery results were obtained.

Some results are illustrated in Fig. CH.IV. 3. 2. in which the measured absorption recovery characteristics of two SUSAMs with 2- and 3-repeat GaAs-$In_{0.2}Ga_{0.8}As$ strained superlattices are compared. The measurements were done at a wavelength of 1035 nm slightly shifted from a resonant wavelength of absorbing $In_{0.26}Ga_{0.74}As$-GaAs QW (1040 nm). In addition, absorption saturation for longer wavelengths (closer to the band gap of QW) can be achieved at lower powers because the reduced number of states available at the bottom of the conduction band for these wavelengths. Unfortunately, tunability of ultrashort pulse DP-VECSEL was limited by optimum operating conditions that have been achieved near 1.035 nm. Pump-probe results show that the strained superlattice quenches

the carrier population in the absorbing QW, the more strain is integrated the shorter absorption recovery of QW can be expected. The SUSAM with 3-repeat strained superlattice has provided ~50 ps absorption recovery without increasing significantly non-saturable losses (~0.3%). Absorption saturation fluence was measured to be approximately equal to ~ 30 μJ/cm$^2$ for a SUSAM with 3-repeat strained superlattice and ~ 17 μJ/cm$^2$ for SUSAM with 2-repeat strained superlattice.

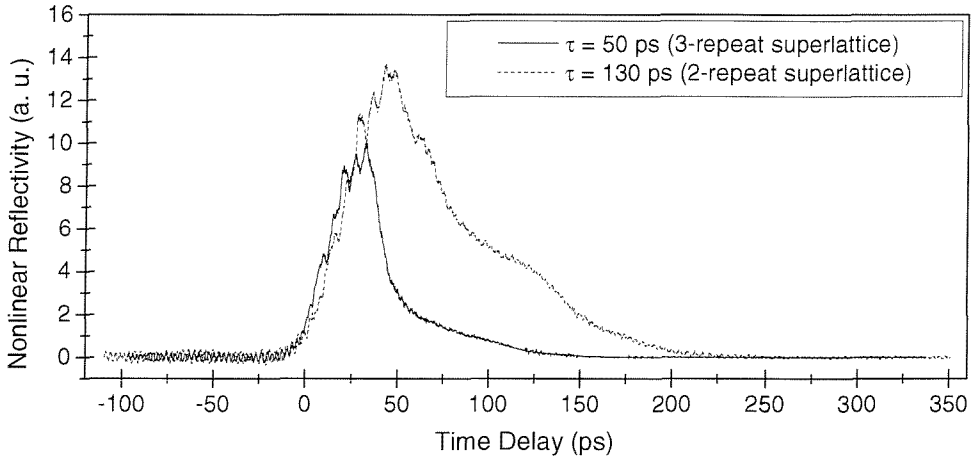


**Fig. CH.IV. 3. 2:** The experimentally measured room temperature absorption recovery lifetime of SUSAMs with 2- and 3-repeat superlattices, QT1563 and QT1580 samples respectively.

The non-exponential absorption recovery character is typical for both SUSAMs as it is shown in Fig. CH.IV. 3. 2. Absorption recovery is approximately equal to ~ 130 ps (at 1/*e* level) for a SUSAM with 2-repeat strained superlattice and ~ 50 ps (at 1/*e* level) for SUSAM with 3-repeat strained superlattice. Therefore, it is evident that induced strain affects the absorption recovery characteristics. In fact both attempts to grow SUSAMs were successful. No further surface degradation has been observed to date. For further understanding of strained superlattice-induced shortening of the carrier lifetime, systematic and growth of II-type and III-type SUSAMs is required.

## CH.IV. 4. Mode Locked DP-VECSEL

### CH.IV. 4-1. *Characterization of the CW lasers*

The CW mode-locked DP-VECSEL is schematically shown in Fig. CH.IV. 4. 1, and was considered to be important to the development of a complete understanding of laser's functionality and of its potential improvements. The complete cavity design was calculated using standard transfer-matrix cavity-design techniques. The standing wave "w-shaped" cavity was used either for CW and CW mode-locked regimes by simply replacing one cavity mirror with saturable absorber mirror. In general, the cavity consists of an output coupler, three highly reflective dielectric mirrors with >99.8% reflectivity centered at 1.04 μm, the DP-VECSEL gain structure (QT1462 sample, 6-QW gain region designed to have maximum absorption centered at 1.01 μm), and I-type SUSAM for CW mode-locking. A fibre-coupled laser (SDL Corporation, Model SDL-6362-P1) capable of delivering a maximum of 1.2 W of power at 0.831 μm was used as a pump laser source. A pump-delivering optical system with two plano-convex lenses formed a ~130 μm pump spot size (diameter) upon DP-VECSEL sample. Fig. CH.IV. 4. 2. shows measured room temperature laser diode output characteristics as a function of drive current. 87% slope efficiency after delivering optics was achieved.

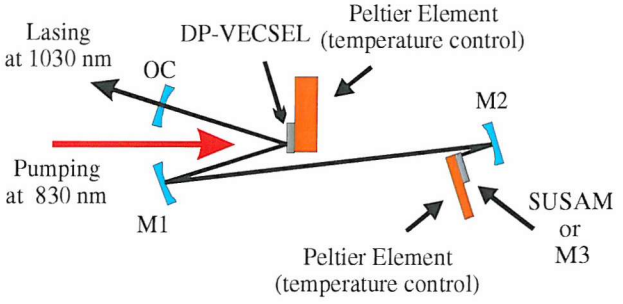


**Fig. CH.IV. 4. 1:** The DP-VECSEL cavity. CO is 0.7% output coupler, Roc = 50 mm; M1- HR mirror with >99.8 reflectivity, Roc = 100 mm; M2 – HR mirror with >99.8 reflectivity, Roc = 38, 25, 15 mm; M3 – HR mirror with >99.8 reflectivity, Roc = ∞.

Much of the cavity alignment is performed in CW regime, as it is the first stage optimization procedure for any mode-locked laser. The optimization is associated with increase of the overlapping between optical cavity mode and pump spot size on DP-VECSEL gain structure. At the beginning this was achieved replacing output coupler with high reflectivity mirror. Usually three parameters are important: lasing threshold, slope efficiency, and transverse mode. Next, a number of output couplers, with different output coupling efficiency (0.7%, 1.0%, 1.5%), were used to optimize output power. At this stage was important to systematically measure laser threshold, slope-efficiency, optical spectrum stability for different DP-VECSEL gain sample temperatures. This helps to establish the optimum laser operating temperature, maximum operating wavelength shift at high pump powers. It is advisable to check whether laser is not operating in a higher order transverse mode after each re-optimization. Initially qualitative investigations of cavity stability were made. The laser output was typically vertically polarized with a contrast ratio in the range 8-16. The divergence was measured equal to ~ 5 mrad.

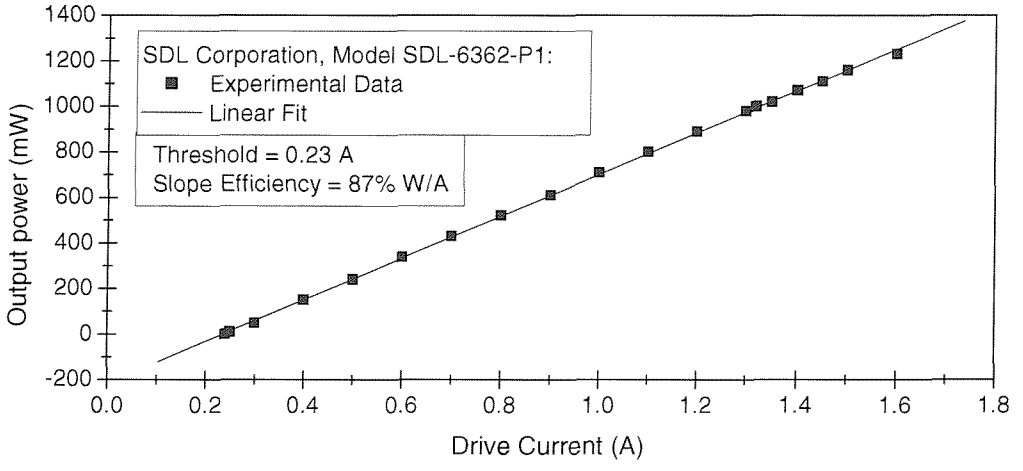


**Fig. CH.IV. 4. 2:** Experimentally measured laser diode (SDL Corporation, Model SDL-6362-P1) output power as a function of diode drive current. Laser threshold is 0.23 A, slope efficiency 87%. Pump delivering system introduced 5% loss.

The cavity used in this work is anisotropic, therefore any depolarization mechanism will result in additional intracavity loss. In case of polarization insensitive gain element, the output radiation from this cavity will be eliptically polarized with larger axis lying along vertical coordinate. Therefore it is advisable to rotate DP-VECSEL gain sample around

cavity axis in order to optimize laser performance. After orientation of DP-VECSEL gain structure, polarization contrast ratio was improved and equal to ~ 16. Fig. CH.IV. 4. 3. shows room temperature edge photoluminescence (PL) measurements of DP-VECSEL gain structure (QT1462 sample, see appendix A) at different pumping levels. It must be pointed out that three parameters are important in PL spectrum for a given variation of sample temperature and pumping level including PL spectrum shape, PL peak wavelength shift and PL spectrum integral. PL spectrum shape does not change a lot with increasing pump power. It is established that for a pump power above 0.7 W, PL spectrum intensity amplitude is starting to saturate. Measurements show no further increase in PL integral above 0.82 W of pump power. It is established that approximately 70% of pump power is absorbed in the MQW region of DP-VECSEL gain structure.

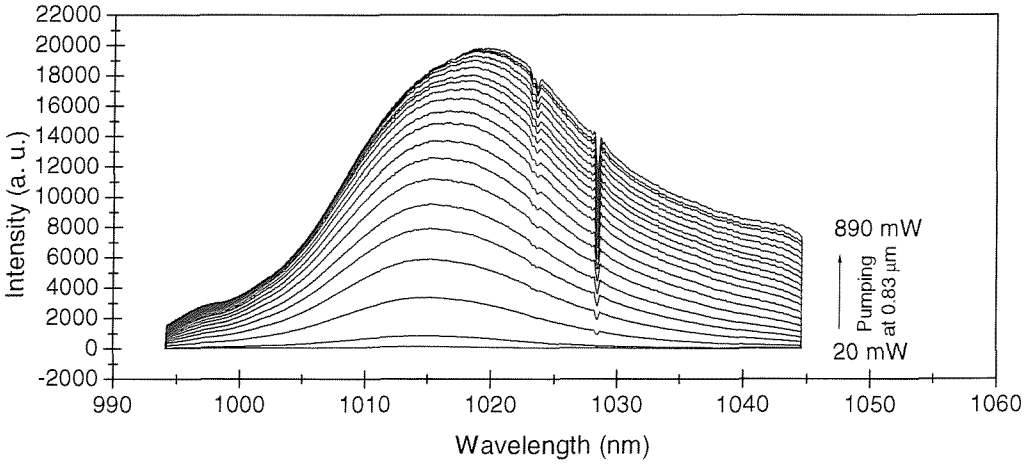


**Fig. CH.IV. 4. 3:** Experimentally measured room temperature edge photoluminescence (PL) spectrum of DP-VECSEL (QT1462 sample) as a function of incident pump power. It is clearly seen that PL spectrum peak wavelength shifts to longer wavelength region with the increase of pump power. No PL spectrum shape deformations are observed.

Fig. CH.IV. 4. 4. shows measured peak wavelength shift in edge PL spectrum. From experimental data it is estimated that peak wavelength shift is linear function of pump power. Peak wavelength shifts to long wavelength region, and shift of 6 nm/W (pump spot size ~ 200 μm) is achieved.

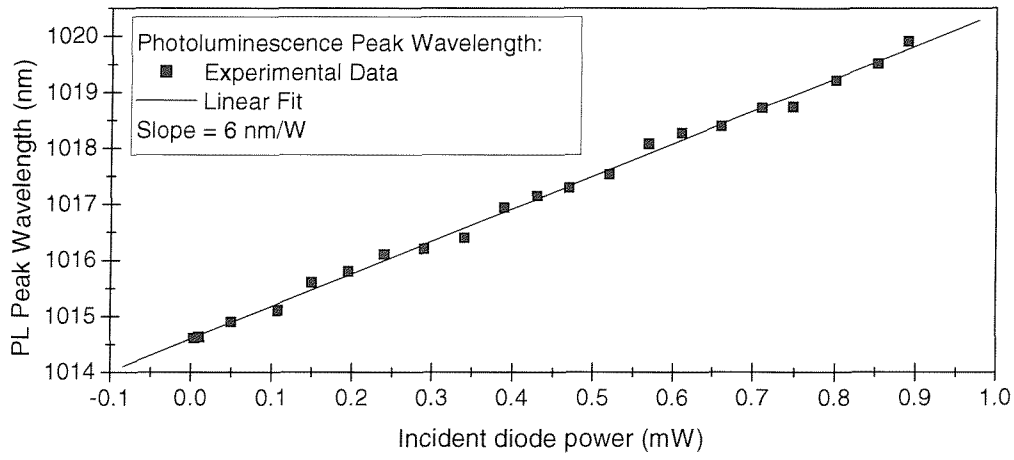


**Fig. CH.IV. 4. 4:** Experimentally measured room temperature edge photoluminescence spectrum of DP-VECSEL (QT1462 sample) as a function of incident pump power. The 6 nm/W peak wavelength shift was achieved, and is characteristic feature of this DP-VECSEL gain structure (pump spot size ~ 200 μm).

Fig. CH.IV. 4. 5. shows measured CW output power of DP-VECSEL gain structure as function of pump power. 8.8% slope efficiency was obtained at room temperature resulting in maximum output power of 64 mW at 1.037 μm for 1.15 W pump power. A CW lasing threshold of 330mW was the lowest observed at room temperature. The temperature of DP-VECSEL gain structure was controlled using Peltier element attached to its holder. The lowest lasing threshold was achieved at 4 $C^0$ and is equal to approximately 300 mW. The maximum slope efficiency was then achieved at 7 $C^0$ and is equal to 12.5%.

Fig. CH.IV. 4. 6. shows typical CW optical spectrum shape increasing incident pump power. Optical spectrum shifts to longer wavelength scale from 1.029 μm to 1.037 μm with increase of pump power from 330 mW to 1.15 W. Fig. CH.IV. 4. 7. shows that the 10.6 nm/W CW optical spectrum shift is larger than in the PL spectrum (6 nm/W), which is due to different temperature conditions of DP-VECSEL gain structure. The temperature rice of DP-VECSEL is related to non-radiative nature of recombination of the photo-generated carriers in MQW gain region. Therefore, DP-VECSEL temperature is always expected to be different for lasing sample and not when radiative recombination is reduced. This is also the reason why quantum efficiency and PL measurements are difficult to compare. Typical temperature of DP-VECSEL lasing sample is approximately

equal to ~ 100 $C^0$ at 0.7 W pump power, which was measured by attaching digital thermometer tip close to a pumping area.

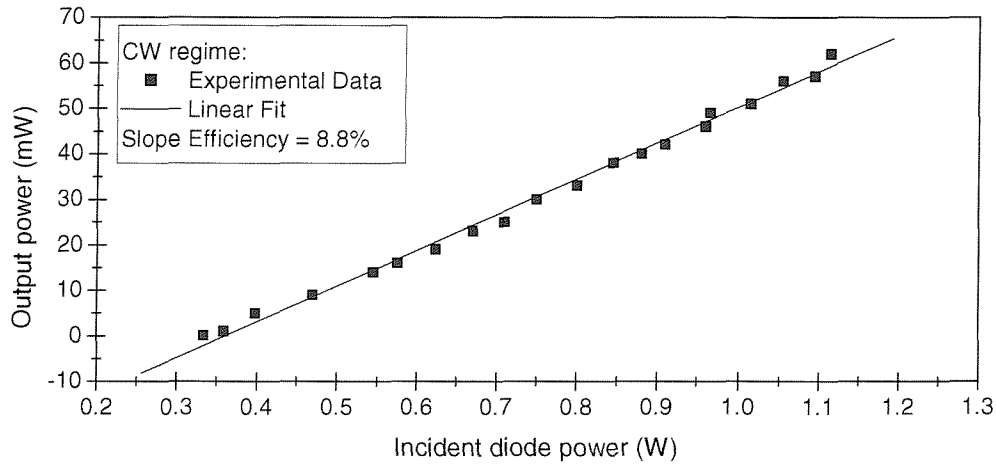


**Fig. CH.IV. 4. 5:** Experimentally measured output power of DP-VECSEL as a function of incident pump power (at room temperature). Slope efficiency is equal to 8.8% (0.7% OC). CW threshold is equal to 330 mW. Slope efficiency increases ab to 13% if 1.0 % OC is used.

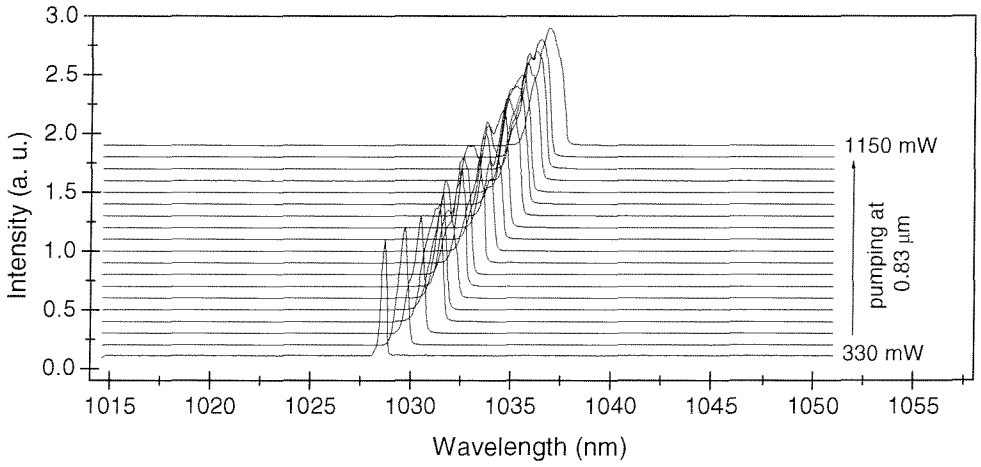


**Fig. CH.IV. 4. 6:** Experimentally measured optical spectrum of DP-VECSEL as a function of incident pump power (at room temperature). CW lasing wavelength shift and linewidth broadening is observed increasing pump power.

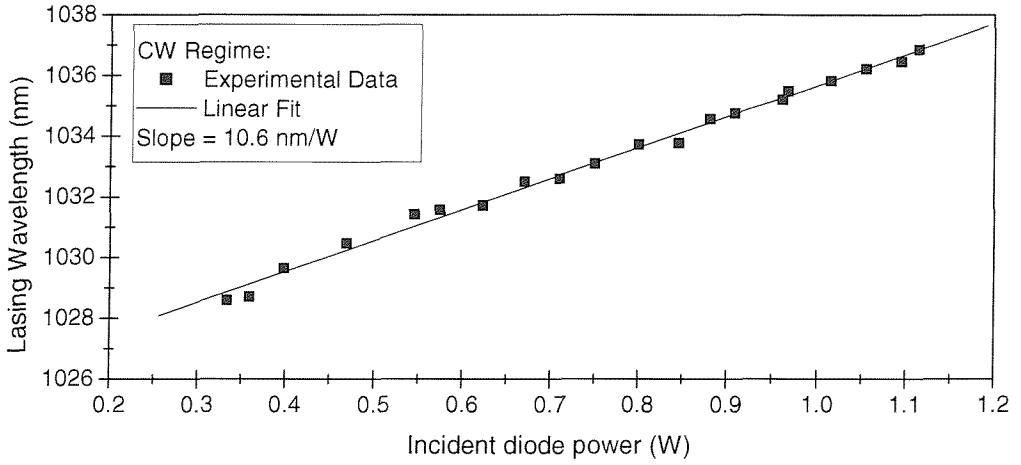


**Fig. CH.IV. 4. 7:** Experimentally measured CW DP-VECSEL laser wavelength shift as a function of incident pump power (at room temperature). Laser wavelength shift is linear function of pump power, and slope is equal to 10.6 nm/W.

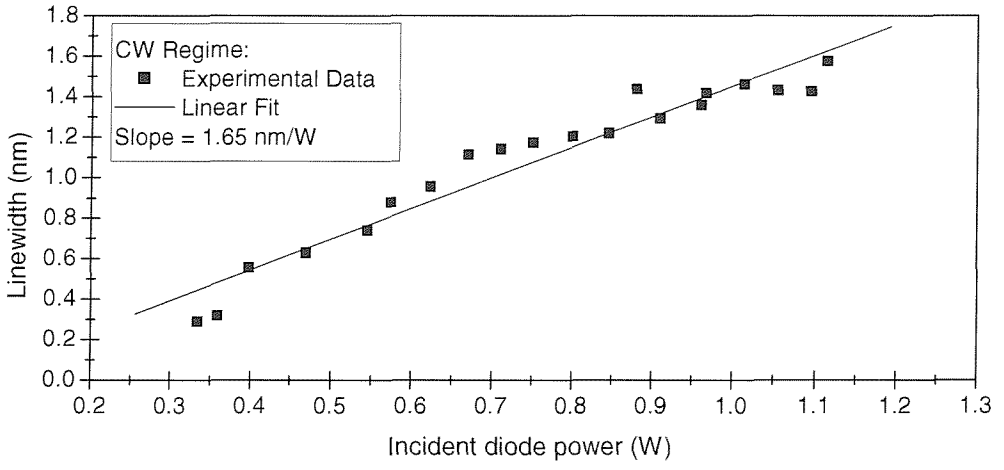


**Fig. CH.IV. 4. 8:** Experimentally measured DP-VECSEL CW linewidth as a function of incident pump power (at room temperature). Laser linewidth is increasing almost linearly with pump power. Slope is estimated equal to 1.65 nm/W.

Fig. CH.IV. 4. 8. shows CW DP-VECSEL linewidth dependence on diode pump power. Results illustrate 1.65 nm/W increase of linewidth with increasing pump power.

## CH.IV. 4-2. *Mode-Locked Operation*

After DP-VECSEL optimization in CW regime, laser was optimized for CW passive mode-locking. To achieve passive mode-locking, the M3 mirror was replaced with saturable absorber mirror. No further cavity alignment is advisable except saturable absorber mirror. Fig. CH.IV. 4. 9. shows passive mode-locking input-output power characteristics achieved using SESAM as saturable absorber mirror in place of M3 mirror. It is observed that saturable absorber mirror with relatively large non-saturable loss turns laser into optically bistable system with characteristic hysteresis in output power. In general any system is said to be bistable if it has two output states for the same value of the input over some range of input values. There are two useful classifications of bistable systems. A system may be absorptive or dispersive depending on whether the feedback from the intracavity elements occurs by the way of an intensity-dependent absorption or refractive index.

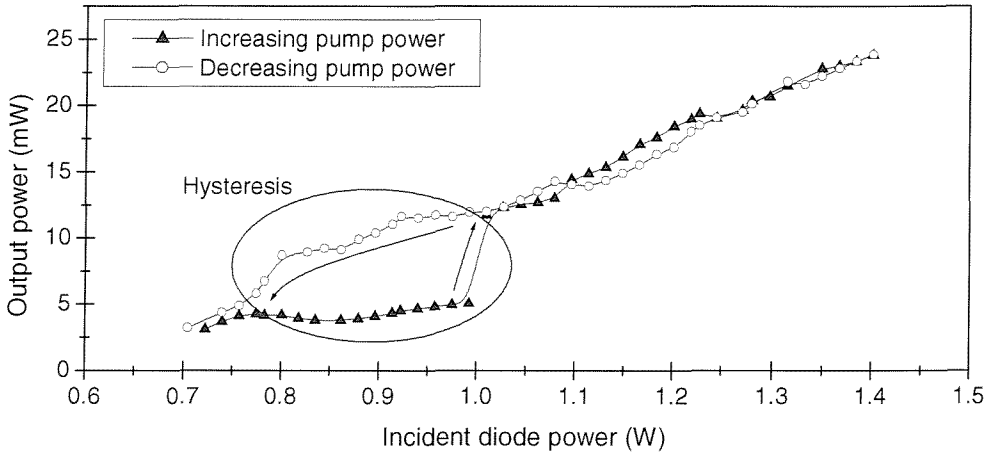


**Fig. CH.IV. 4. 9:** Experimentally measured CW passively mode-locked DP-VECSEL output power as a function of incident pump power (at room temperature) using SESAM (modulation depth ~ 0.7%, non-saturable loss ~ 1.0%, absorption recovery ~ 150ps). Typical hysteresis is characteristic feature in case when saturable absorber mirror has smaller modulation depth than non-saturable loss, and is unsaturated. M2 with Roc = 38 mm was used.

Both absorptive and refractive mechanisms may be significant simultaneous. A passively mode-locked DP-VECSEL laser could be quite complex and hybrid bistable laser system. Hysteresis is the result of a regenerative process that occurs in the vicinity of the absorption saturation of SESAM. In accordance with this process, a slight increase in intracavity optical power causes a slight decrease in the absorption, which, in turn, permits the cavity to accept more power. This added power further saturates the saturable absorber, which again permits more power to be coupled into the cavity. This process is cumulative, with the net result that the change in the power level within the cavity exceeds the original small change in the incident power on saturable absorber. Thus, there is a threshold level at which laser system is unstable and switches into mode-locking regime. As pump power is decreased, the laser responds in a different manner. Because of the high field intensity that builds up within the cavity (pulsed regime), the saturable absorber is maintained in its low attenuation state even though the incident power on the absorber is decreased below starting-up threshold level. As a consequence, the reflected power from saturable absorber remains high.

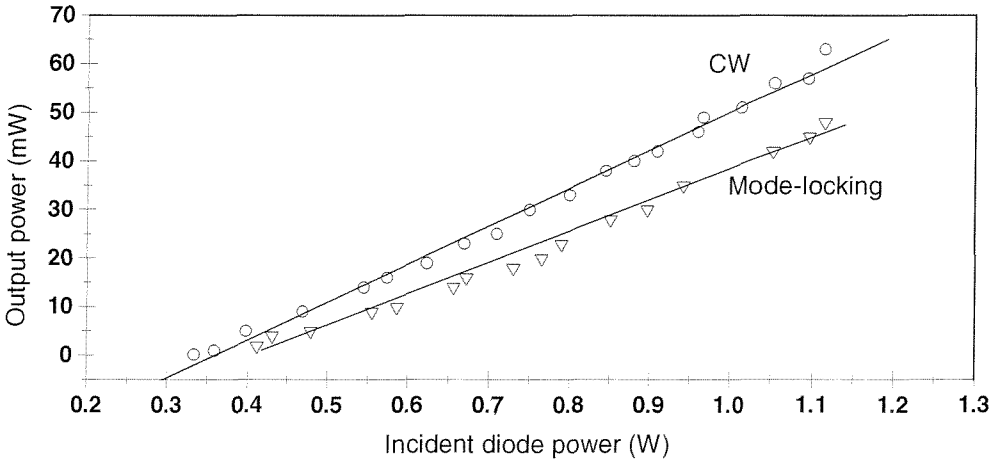


**Fig. CH.IV. 4. 10:** Experimentally measured CW and CW passively mode-locked output power as a function of incident pump power (at room temperature), without and with I-type SUSAM (modulation depth ~ 0.7%, non-saturable loss ~ 0.3%, absorption recovery ~ 50ps). M2 mirror with Roc = 25 mm was used.

Essentially, all the incident power on the absorber continues to sustain the saturable absorber in its low loss state. This continues until the incident power on the absorber can not sustain the saturable absorber in its low-loss state, and laser switches-down. The saturable absorber then switches to its high loss state. In Fig. CH.IV. 4. 10. CW and CW passive mode-locking results are compared. The pulse characteristics will be discussed below. To obtain sufficient bleaching of the SUSAM a concave mirror with a 25 mm radius of curvature was used reducing the effective laser mode diameter (the effective laser mode diameter is the $1/e^2$ Gaussian beam diameter with respect to intensity) approximately to 20 μm upon the SUSAM. The separation between the M2 mirror and the SUSAM was ~ 12.5mm. The low loss introduced by the SUSAM was evident from the 49 mW of mode-locked maximum average output power, when the maximum CW output power with high reflectivity mirror was 63 mW. No hysteresis was observed using SUSAM, showing low insertion loss of this device. From other point of view, hysteresis could disappear if down-switching point in the hysteresis moves to higher power levels while switching-up is practically unaffected. This usually happens when insertion loss is very high. The overal effect of an increasing linear (non-saturable) loss is decrease in the area of the hysteresis curve and in the maximum reflection.

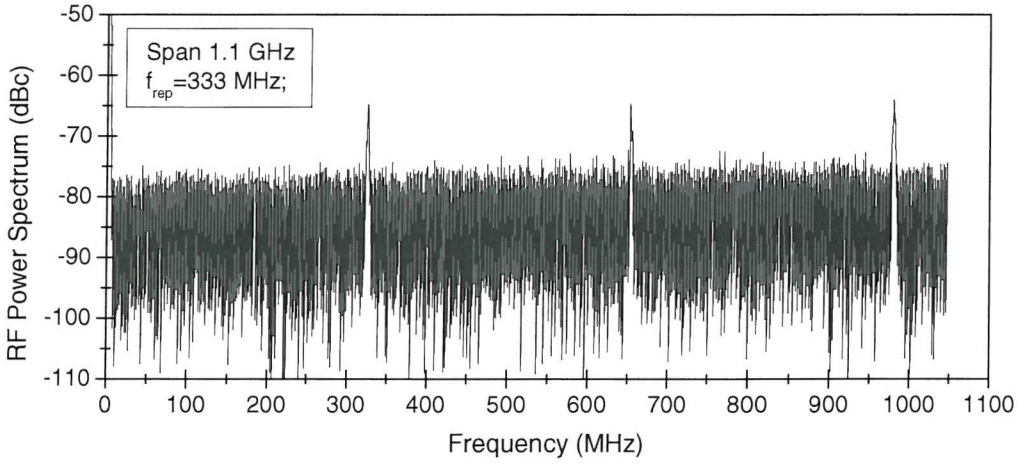


**Fig. CH.IV. 4. 11:** Experimentally measured radio-frequency (RF) power spectrum of CW passively mode-locked DP-VECSEL laser using SUSAM with 3-repeat superlattice (absorption recovery ~ 50 ps).

Span 1.1 GHz, pulse repetition rate 333 MHz. The signal was measured with a 25 GHz photodiode and a 26.5 GHz spectrum analyzer.

Fig. CH.IV. 4. 11. shows measured radio frequency (RF) power spectrum that confirms achieved passive mode-locking with a fundamental pulse repetition rate of 333 MHz. Fig. CH.IV. 4. 12. shows measured radio frequency (RF) power spectrum of CW mode-locked DP-VECSEL laser with 100 kHz span. The signal width was equal to 10 kHz (FWHM) at 333.757 MHz fundamental pulse repetition rate. RF signal width defines time jitter, temporal random pulse deviation in the pulse train. The narrower the RF signal width is, the better jitter corresponds.

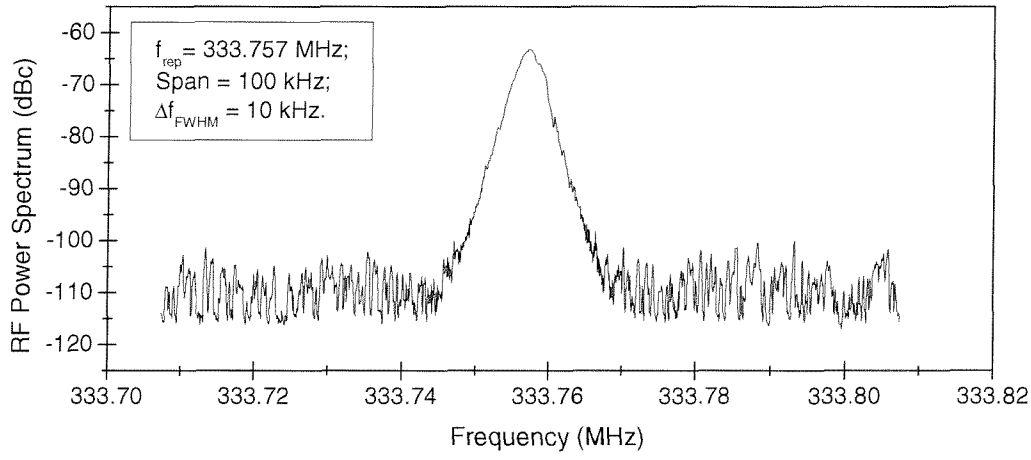


**Fig. CH.IV. 4. 12:** Experimentally measured radio-frequency (RF) power spectrum of CW passively mode-locked DP-VECSEL laser. Span 100 kHz, pulse repetition rate 333.757 MHz. The fundamental pulse repetition rate fluctuations correspond to 10 kHz. The signal was measured with a 25 GHz photodiode and a 26.5 GHz spectrum analyzer.

Fig. CH.IV. 4. 13. shows measured second-order intensity autoccorrelation and corresponding optical spectrum of generated pulses. The pulse duration measurements were made with a non-collinear second-order intensity autocorrelator (Femtochrome, Model FR-103) and a sampling oscilloscope (Tektronix, Model TDS-360) combination. The pulse spectrum was measured with digital triple grating spectrograph (EG&G Princeton Applied Research, Model 1235) with a spectral resolution of 0.1 nm. Unfortunately, second-order autocorrelations, being symmetrical functions, cannot provide

unequivocal information on the pulse shape and in particular its asymmetry (except cross-autocorrelations).

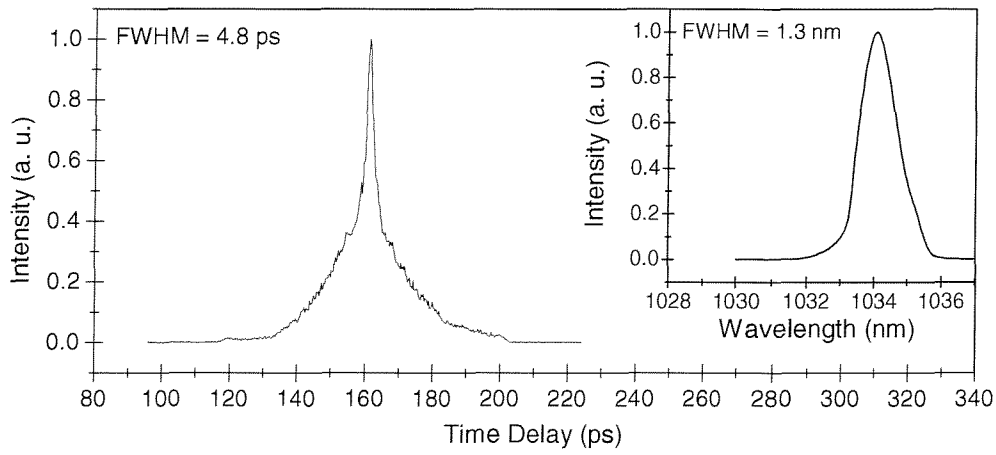


**Fig. CH.IV. 4. 13:** Second-order intensity autocorrelation and corresponding optical spectrum (inset) of resulting pulses. 4.8 ps long (FWHM) pulses were generated using SUSAM with 3-repeat superlattice, optical spectrum bandwidth 1.3 nm (FWHM) centered at 1.035μm. No information about pulse shape can be reconstructed because all phase information in the second-order intensity autocorrelations is overaged out.

Moreover, the intensity autocorrelations that are generally used are very insensitive to the particular pulse shape. In principle, successive optical correlations of increasing order (2,3...) would provide the answer. But it is impractical to use higher-order processes because of the low pulse energies in unamplified pulse trains. The use of interferometric autocorrelations would provide more accurate information pulse envelope and phase modulation effects that happening in ultrashort pulse DP-VECSEL. The passive mode-locking was observed over the 1.030-1.040 μm wavelength range with variation of the pulse duration from 5 to 30 ps. Pulse trace is shown in Fig. CH.IV. 4. 14.

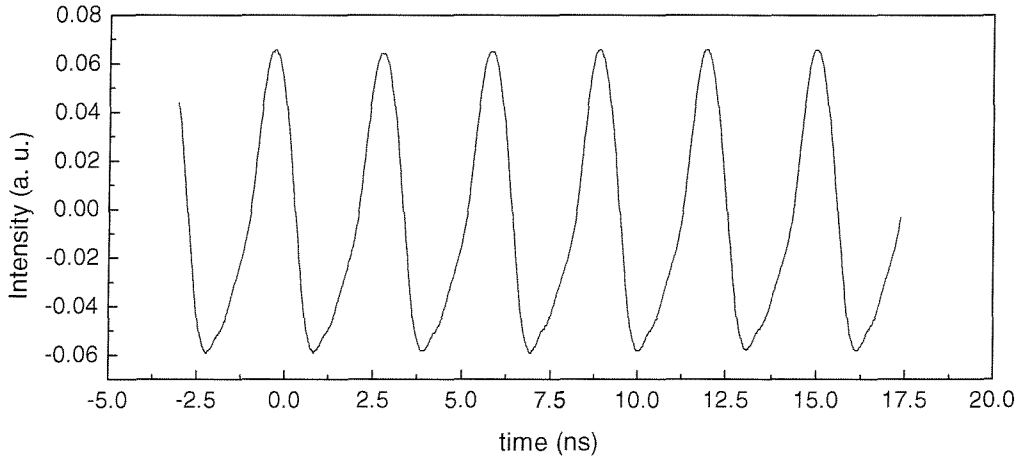


**Fig. CH.IV. 4. 14:** Experimentally measured pulse trace of CW mode-locked DP-VECSEL laser. The signal was measured with a 2 GHz photodiode and a 400 MHz digital sampling oscilloscope.

The 2-repeat superlattice SUSAM also produces mode-locked pulses despite its relatively long absorption recovery time (absorption recovery ~ 130 ps, modulation depth ~ 0.7%, non-saturable loss ~ 0.3%), however the measured second-order intensity autoccorrelation and corresponding optical spectrum of generated pulses show presence of additional satelite-like pulses in the cavity, see Fig. CH.IV. 4. 15. Typical second-order intensity autocorrelation is symmetrical time delay function. An additional side-peak shift from fundamental pulse peak in the region of 5 to 75 ps was observed in second-order intensity autocorrelations. Optical spectrum of resulting pulses shows asymmetry. The 9 ps long pulses were generated at 1.033 μm. In this case satelite-like pulse existence near fundamental pulse is evident.

In general, satelite pulse appearance in the cavity is the result of undesirable feedback originating from intracavity optical elements. Large side-peak shift corresponds to a possible feedback from dielectric mirror substrates. Small side-peak shift is the result of feedback from DP-VECSEL and SUSAM substrates. The third not less important possibility is the pulse reflections at air-semiconductor interface. In all three cases pulse interference effects are involved. In general, these could be divided into two groups: intracavity pulse interference within pulse coherence length, or intracavity pulse interference outside pulse coherence length. The first case involves pulse interference with itself, interference of fundamental pulse and its reflected part from either air-

semiconductor interface and/or substrate. This usually affect pulse formation dynamics, because fundamental pulse that enters DP-VECSEL gain structure or SUSAM experiences interference with already phase-modulated its part. This could result in pulse break-up, rapid pulse shortening, instabilities. This is also the case of possible DP-VECSEL gain structure and SESAM, SUSAM surface degradation, because pulse interference occurs at air-semiconductor interface. The answer to this problem is the use of AR coatings and strong-loss component (heavy delta dopping below buffer layer) below integrated mirrors for both DP-VECSEL gain structure and SUSAM. For the first time, to the best of my knowledge the loss mechanism below the integrated mirrors, and AR coating that controls device dispersion is suggested and described in this thesis. In the case of large side-peak shift that is seen in intensity autocorrelations, pulse satelites originate from mirror substrates.

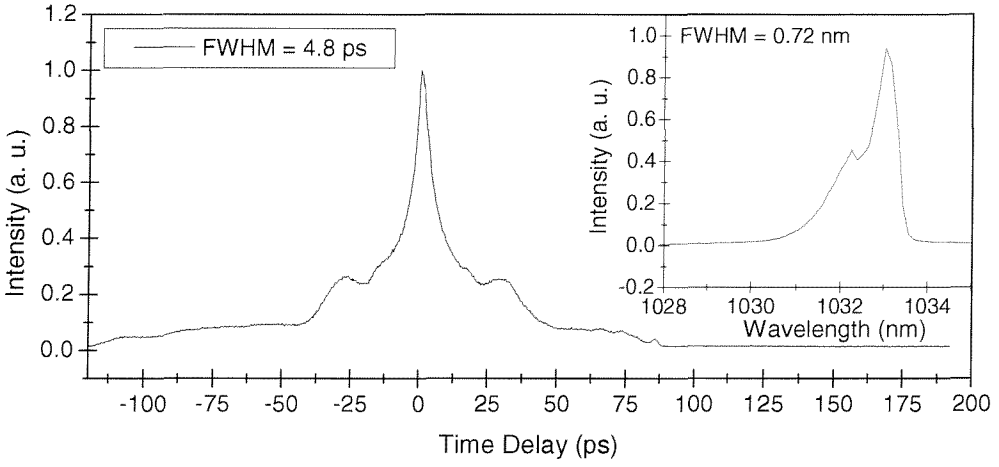


**Fig. CH.IV. 4. 15:** Second-order intensity autocorrelation and corresponding optical spectrum (inset) of resulting pulses. 4.8 ps long (FWHM) pulses were generated using SUSAM with 2-repeat superlattice, optical spectrum bandwidth 0.72 nm (FWHM) is centered near 1.033μm.

The pulse-like satelites appear in the passively mode-locked laser when saturable absorber with relatively long absorption recovery is used. In this case small pulse-like (pulse-like because for example pulse part that is reflected from the substrate could be less coherent due to large random dephasing mechanisms) signal could experience low loss by passing

already saturated saturable absorber mirror by fundamental pulse. This process is regenerative and cumulative with the net result that is satelite pulse existance.

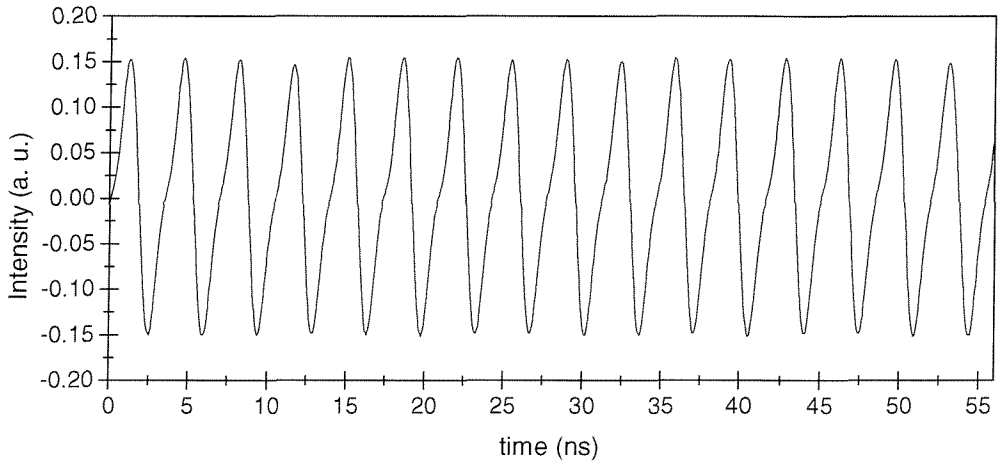


**Fig. CH.IV. 4. 16:** Experimentally measured pulse trace of CW mode-locked DP-VECSEL laser using SUSAM with 2-repeat superlattice. The signal was measured with a 2 GHz photodiode and a 400 MHz digital sampling oscilloscope. Typical asymmetry shows satelite pulse existence in the cavity.

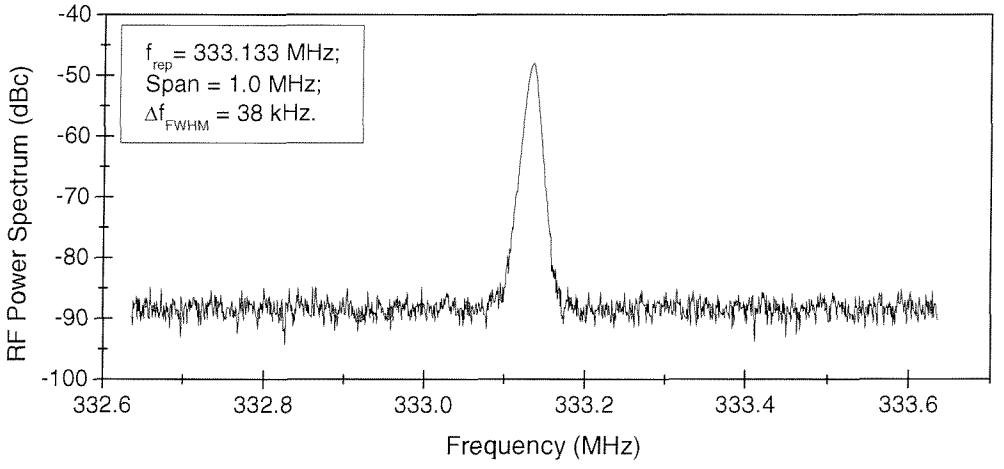


**Fig. CH.IV. 4. 17:** Experimentally measured radio-frequency (RF) power spectrum of CW passively mode-locked DP-VECSEL laser using SUSAM with 2-repeat superlattice. Span 1.0 MHz, pulse repetition rate 333.133 MHz. The fundamental pulse repetition rate fluctuations correspond to 38 kHz. The signal was measured with a 25 GHz photodiode and a 26.5 GHz spectrum analyzer.

Fig. CH.IV. 4. 16. shows experimentally measured pulse trace of CW mode-locked DP-VECSEL laser using SUSAM with ~130 ps absorption response. Satelite existance usually results in larger time jitter in RF spectrum as it is shown in Fig. CH.IV. 4. 17. Timing jitter of a pulse trace was measured approximately equal to 38 kHz at 333.133 MHz fundamental cavity frequency.

The experimental results and observations described in this work could be developed into general conclusion. For the first time successful development and demonstration of SUSAMs in passively mode-locked DP-VECSEL laser is introduced. It is shown that SUSAMs are low-insertion loss devices (non-saturable loss ~ 0.3%) with sufficiently fast absorption recovery characteristics (3-repeat superlattice SUSAM ~ 50ps, and 2-repeat superlattice SUSAM ~130 ps), and which can be manufactured using standard single-step MOCVD growth. No additional post-growth processing is required. In addition, no further SUSAM degradation has been observed. In principle is shown that the strained superlattice adjacent to QWs quenches the carrier population in the absorbing QWs, effectively shortening the carrier lifetime without increasing significantly non-saturable losses in the entire SUSAM device. The strained absorbing active region can be integrated anywhere in the complex SUSAM device if oppositely strained materials are used to balance out the strain over an entire structure. Therefore SUSAMs with AR coatings (preferably with dispersion control) and strong loss mechanism (heavy delta doping below buffer layer) below integrated mirrors is necessary step for further passively mode-locked DP-VECSEL development in order to avoid any pulse break-up processes, instabilities.

# CHAPTER V
# CONCLUSIONS AND FUTURE WORK

## CH.V. 1. CONCLUSIONS

The theoretical, experimental results and observations described in this work could be developed into following conclusions:

- It is established that indirect design methods can be very effective in designing semiconductor devices such as DP-VECSELs and saturable absorber mirrors. The desired specifications of the entire device can be achieved optimizing one part of the device (mostly AR region), while keeping the entire device as simple as possible. It is the most straightforward way to achieve design that is much technologically simple and meets manufacturing demands.

- For the first time there has been developed a novel superlattice-based design of saturable absorber mirror (SUSAM) that has been manufactured by only using single-step metal-organic chemical-vapor deposition (MOCVD) under standard conditions. It is established that the use of strained quaternary $In_{1-x}Ga_xAs_yP_{1-y}$ material for quantum well (QW) devices allows far wider scope for possible structures.

- It is shown that the strained superlattice adjacent to the QWs quenches the carrier population in the absorbing QWs, effectively shortening the carrier lifetime without increasing significantly non-saturable losses in the entire SUSAM device. The strained absorbing active region can be integrated anywhere in the complex SUSAM device if oppositely strained materials are used to balance out the strain over an entire structure.

- SUSAMs have been effectively used to mode-lock a DP-VECSEL near 1035 nm. The 5-ps long pulses at a repetition rate of 330 MHz in a circular diffraction-limited beam have been generated with average power scaling of up to 45 mW.

- The AR coatings (preferably with dispersion control) and strong loss mechanism (heavy delta doping below buffer layer) below integrated mirrors should be necessary step for further passively mode-locked DP-VECSEL development in order to avoid any pulse break-up processes, instabilities.

This conclusion could be important in developing high power CW passively mode-locked DP-VECSELs. There have been reports on rapid DP-VECSEL gain structure degradation at high pump powers (U. Keller's group in Zurich, Switzerland), which is still an open problem. No clear possible explanations have been made to date. Therefore very possible explanation is discussed below. In passively mode-locked DP-VECSEL laser the only element that is optically pumped is DP-VECSEL gain structure. It is well known that laser-based annealing is very important in microelectronic industry. Laser-based annealing modifies semiconductor properties locally changing semiconductor characteristics (local re-crystalization), and therefore no substrate annealing is required. It is also known that laser-based annealing is relatively short process. But it was established that laser annealing could introduce problems associated with laser induced defect migration in semiconductors. Therefore it is very possible that optical pumping induces defect migration into DP-VECSEL gain structure pumped area. It is also known that optical pumping introduces stress, and that migrating defects tend to distribute along the axis of induced anisotropy.

## CH.V. 2. FUTURE WORK

The work described here can be extended in a few new directions. First of all it must be pointed out that indirect design algorithms are very important and should also be explored. These have potential use in further developments of SUSAM and DP-VECSEL devices. Next, possibilities to integrate superlattice coolers that use thermionic and thermoelectric effects with SUSAMs, DP-VECSEL gain structures could be investigated. For commercial applications this would be of primary interest to manufacture efficient, compact and reliable laser sources avoiding complex multi-step manufacturing and packaging procedures. The use of interface plasmon effects could also be considered as potentially possible ultra-fast saturable absorber mirrors. Novel mode-locking mechanism is suggested using electromagnetic field spatial transformations. These all are enumerated in this section below.

- Possible directions for indirect design algorithm development would include more adaptive methods, that change desired device specifications in some range of interest defined by statistical approach. It is also advisable to optimize indirect design, optimization algorithms particularly using integral optical field functions as desired specifications. This would in principle allow us to develop, for example, novel semiconductor lasers with specific effective gain profiles.

- Further improvements of SUSAMs include doping of strained regions with suitable dopants, electrically active, magnetically active defects, which should be considered as well. SUSAM device is expected to offer broad-band fast absorption recovery characteristics by integrating a few absorbing QWs of different compositions into strained supperlattices. The broad-band absorption recovery can be achieved using QWs with inhomogeneously variable alloy composition. In general SUSAMs provide flexibility in growth of any antireflection coating with specific amplitude-frequency and phase-frequency characteristics.

- Potential possibilities integrating superlattice coolers that use thermionic and thermoelectric effects, with SUSAMs, DP-VECSEL gain structures could be a next step optimizing thermal control, simplifying manufacturing and packaging of these devices. It is known that superlattice structures were used to enhance the cooling device performance by reducing the thermal conductivity between the hot and cold junctions, and by providing selective removal of hot carriers through thermionic emission process. Superlattice coolers can be fabricated in an array format electrically in series and thermally in parallel, similar to conventional thermoelectric devices, and thus achieve large cooling capacities (hundreds of watts per square centimeter) with relatively small currents. We expect that SUSAMs, DP-VECSEL gain structures integrated with superlattice coolers could lead to a compact, and cost effective temperature stabilized device.

- Novel mode-locking mechanism is related to an idea of using nano-structured QWs and their orientation in spatially transformed intracavity electromagnetic (EM) fields. It is well established that tight focused light beam in a small region of the MQW layers shortens the absorption recovery time due to lateral carrier diffusion. To the best of my knowledge passive mode-locking was achieved with variety of solid state laser materials focusing light beam into a relatively small but symmetric spot region of the QW based device. The idea is to focus light beam into, for example, a small line-type, ring-type, spiral-type region of the QW based device in order to modify carrier lateral diffusion conditions from interaction region. Possibilities to have angular tunability of temporal response characteristics are evident. The following features are:
    a) The absorption recovery characteristics are averaged over large area.
    b) Increased saturation intensity – important for high power pulsed microchip lasers.
    c) For passive mode-locking or Q-switching can be used standard large area commercially available VECSELs.

  In general, periodically and/or aperiodically nano-structured QW based device orientated with respect to incident light spatial form could broaden general device characteristics for wide range applications.

- Periodically alternating structured multilayers in combination with gain or absorbing regions are novel type micro devices. The nano-structuring of semiconductor layer increases its absorption typically by 60% (absorption depth decreases from 1 μm to a few tens of nm). The nano-structured layer as an average graded composition-depth profile smoothly changes the layer's effective optical constants. This graded refractive index reduces the reflection from air-semiconductor interface in much wider spectral region than it can be achieved with multilayer AR coatings. In general the effect can be attributed to coupling of the incident radiation to interface electromagnetic wave. I suggest to use periodically structured interfaces close to QWs in order to increase absorption in much smaller volume. I believe that this will make very efficient single-QW-based lasers, integrated laser based devices.

- It is known that the macroscopic optical properties of thin films can be greatly modified by nano-structuring the surface on a scale smaller than the optical wavelength. It has been shown that the reflectivity of surface has been reduced, and the absorption of semiconductor layers has been greatly increased by structuring surfaces (phonon-plasmon iteractions). The effect relates to light coupling to a surface wave in the absorbing region formed by the structured interface. The structured interface modifies carrier lateral diffusion conditions in similar way as it is in tight light focusing case. Therefore the use of periodically and/or aperiodically nano-structured interfaces of the absorbing QWs is another way of shortening the absorption recovery time in MQW-based devices. It is very possible that the plasma could be very unstable under specific circumstances. Therefore fast switching can be achieved using nano-structured QW interfaces involving phonon-plasmon iteractions.

# APPENDIX A

## SAMPLE GROWTH AND CHARACTERIZATION

In order to simplify thesis all grown samples are described and specified in this section. Samples were grown using metal-organic chemical-vapor deposition (MOCVD) technology. Most samples typically were grown by MOCVD at normal growth temperatures on a 0.5-mm-thick undoped GaAs wafers oriented $3^0$ from the (100) toward the (110) plane ((100) $3^0 \rightarrow$ (110) $\alpha = 45^0$). Maximum two wafers were placed and positioned in the growth chamber reactor – "down-wafer" and "up-wafer". Therefore experimental results are shown for both "down" and "up" wafers. Samples were tested first of all visually, taking microscope images to check surface quality, and then making reflection/transmission measurements across the whole wafer. This is important and the most time consuming part of the characterization in order to define more accurately the best part of the sample. Therefore some characterization results are given in this section.

1. DP-VECSEL (A. Garnache).

QT1462 sample, standard MOCVD growth;

Ingot Number WV 0000/Un, (100) $3^0 \rightarrow$ (110) $\alpha = 45^0$;

Structure formula: S □ buffer $[HL]^{28}$ GM □ 1.0; ($\lambda_0 = 1.03$ μm, $n_L(AlAs) = 2.94$, , $n_H(Al_{0.1}Ga_{0.9}As) = 3.433$, $n_S(GaAs) = 3.496$). Device contains 6 10-nm thick $GaAs_{0.94}P_{0.06}$-$In_{0.20}Ga_{0.80}As$-$GaAs_{0.94}P_{0.06}$ QWs have maximum absorption at 1.01 μm.

2. QT1511 sample, standard MOCVD growth.

Ingot Number WV 3527.029/Un, (100) $3^0 \rightarrow$ (110) $\alpha = 45^0$;

Structure formula: 12S □ buffer AR □ 1.0; ($\lambda_0 = 1.03$ μm, $n_L(AlAs) = 2.94$, $n_{Lqw}(In_{0.25}Ga_{0.75}As) = 3.344$ $n_H(Al_{0.1}Ga_{0.9}As) = 3.433$, $n_S(GaAs) = 3.496$).

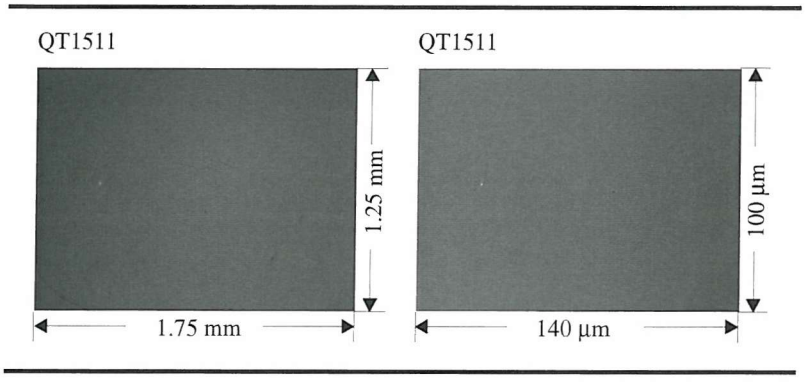


**Fig. A. 1:** Microscope images of QT1511 sample.

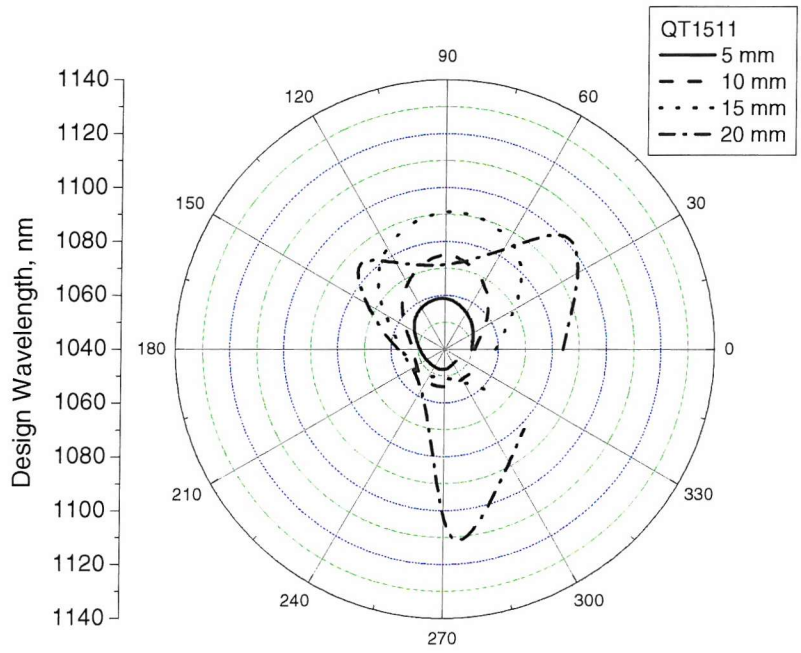


**Fig. A. 2:** Experimentally measured design wavelength shift in the transmission spectrum across QT1511 wafer.

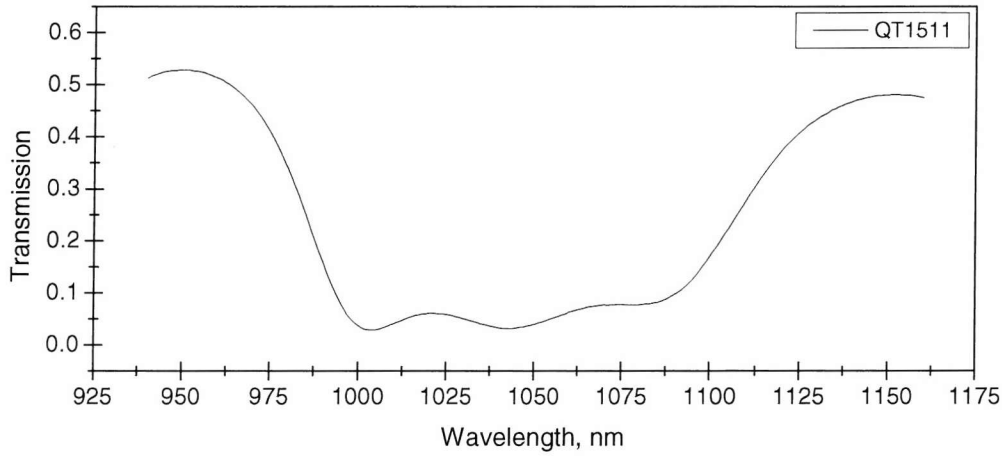


**Fig. A. 3:** Experimentally measured the transmission spectrum at one point of QT1511 wafer.

3. QT1531 sample, standard MOCVD growth of Saturable absorber mirror.

Ingot Number Up-WV 3527.014/Un, (100) $3^0 \rightarrow$ (110) $\alpha = 45^0$;

Ingot Number Down-WV 3527.026/Un, (100) $3^0 \rightarrow$ (110) $\alpha = 45^0$;

Structure formula: 62S □ buffer $[HL]^{27}$ 0.204H $0.13L_{qw}$ 0.665H □ 1.0; ($\lambda_0 = 1.03$ μm, $n_L(AlAs) = 2.94$, $n_{Lqw}(In_{0.25}Ga_{0.75}As) = 3.344$ $n_H(Al_{0.1}Ga_{0.9}As) = 3.433$, $n_S(GaAs) = 3.496$). Device contains single 10-nm thick GaAs-$In_{0.25}Ga_{0.75}As$-GaAs designed to have maximum absorption at 1.04 μm.

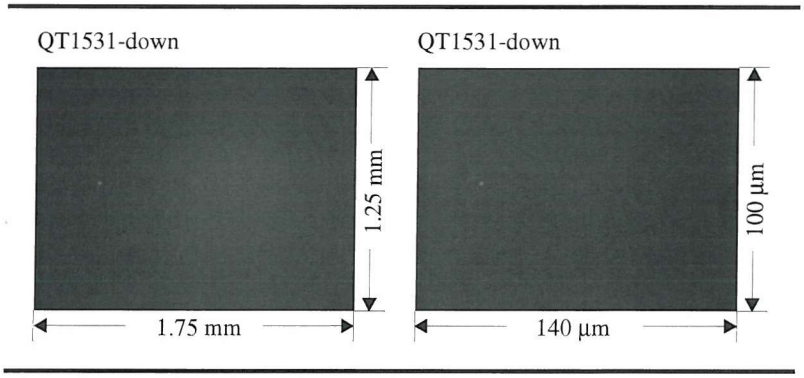


**Fig. A. 4:** Microscope images of QT1531-down sample.

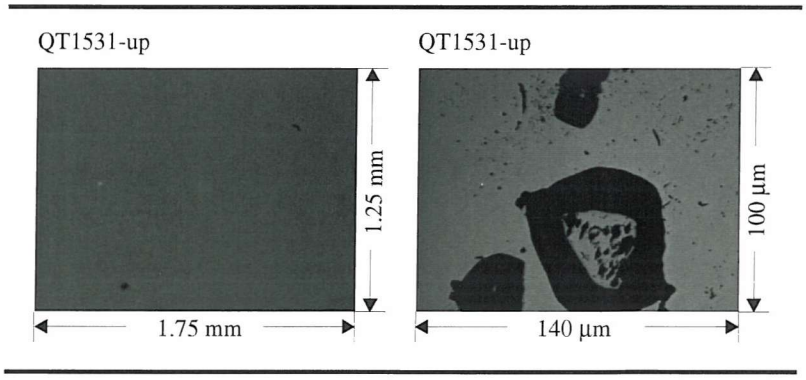


**Fig. A. 5:** Microscope images of QT1531-up sample.

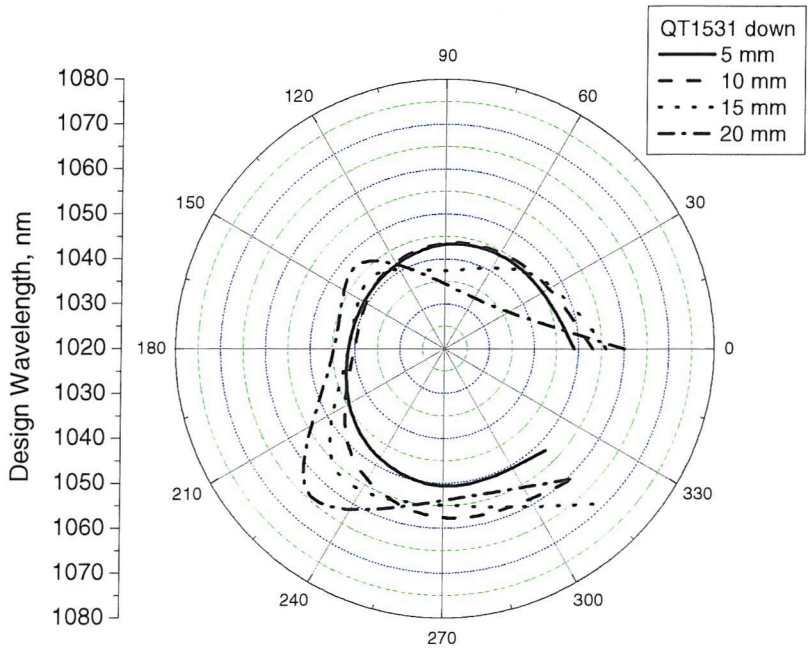


**Fig. A. 6:** Experimentally measured design wavelength shift in the transmission spectrum across QT1531-down wafer.

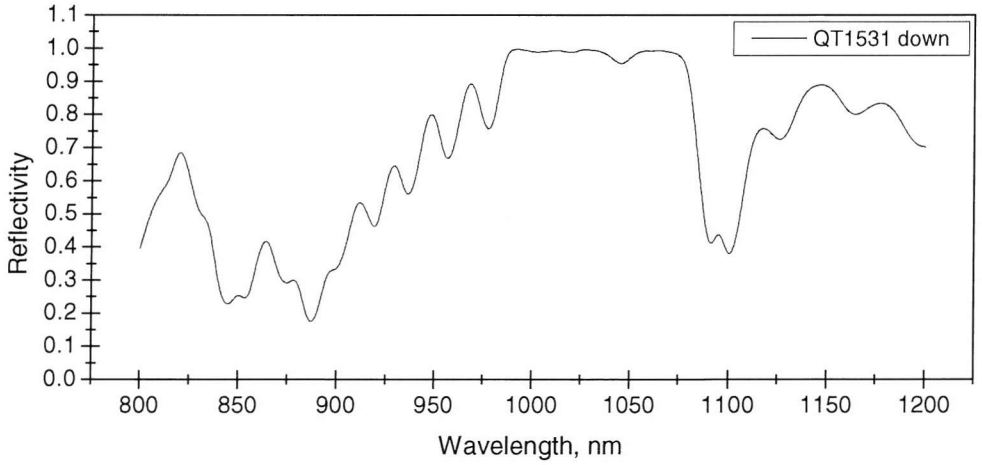


**Fig. A. 7:** Experimentally measured the reflection spectrum at one point of QT1531-down wafer.

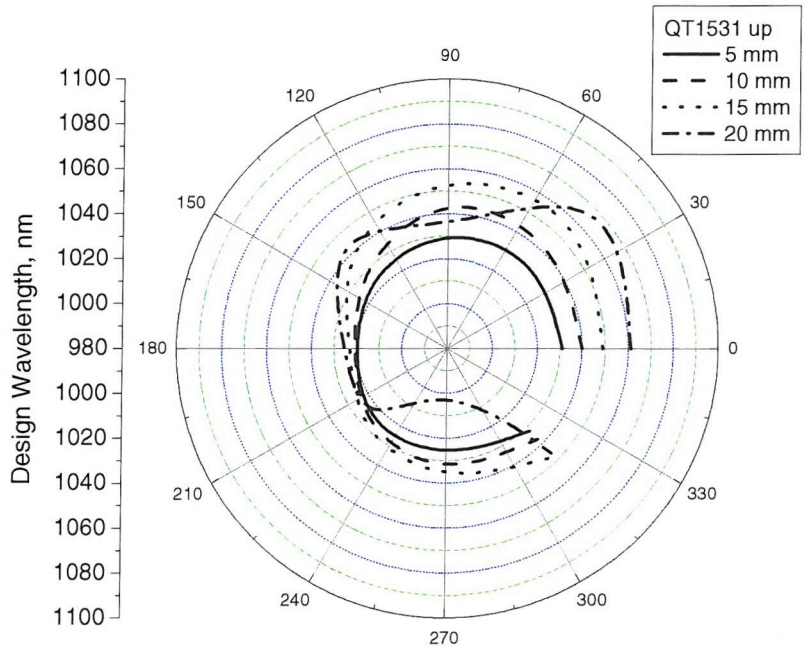


**Fig. A. 8:** Experimentally measured design wavelength shift in the reflection spectrum across QT1531-up wafer.

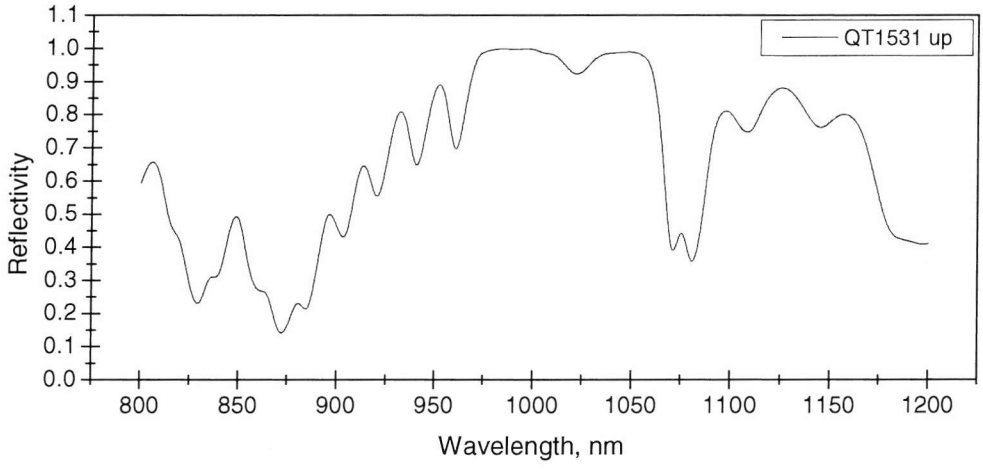


**Fig. A. 9:** Experimentally measured the reflection spectrum at one point of QT1531-up wafer.

3. QT1548 sample, standard MOCVD growth of saturable absorber mirror.

Ingot Number Up-WV 2067.002/Un, (100) $3^0 \rightarrow$ (110) $\alpha = 45^0$;

Ingot Number Down-WV 4061.047/Un, (100) $3^0 \rightarrow$ (110) $\alpha = 45^0$;

Structure formula: 62S □ buffer $[HL]^{27}$ 0.204H 0.13$L_{qw}$ 0.665H AR □ 1.0; ($\lambda_0 = 1.03$ μm, $n_L(AlAs) = 2.94$, $n_{Lqw}(In_{0.25}Ga_{0.75}As) = 3.344$ $n_H(Al_{0.1}Ga_{0.9}As) = 3.433$, $n_S(GaAs) = 3.496$). Device contains single 10-nm thick GaAs-$In_{0.25}Ga_{0.75}As$-GaAs designed to have maximum absorption at 1.04 μm.

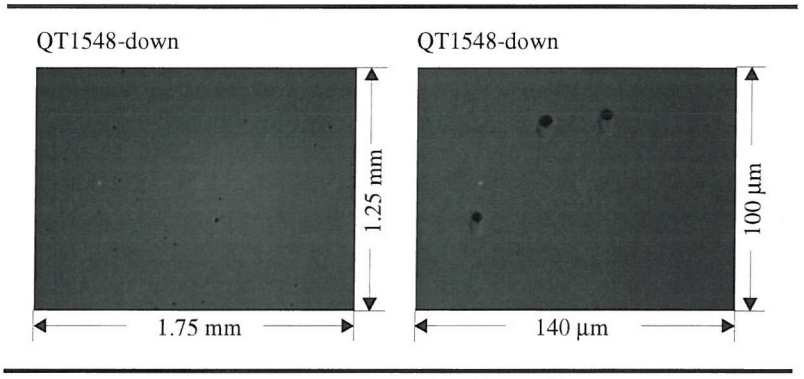


**Fig. A. 10:** Microscope images of QT1548-down sample.

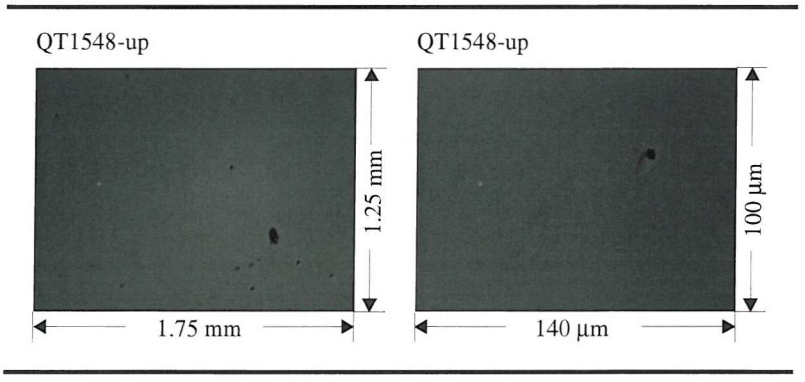


**Fig. A. 11:** Microscope images of QT1548-up sample.

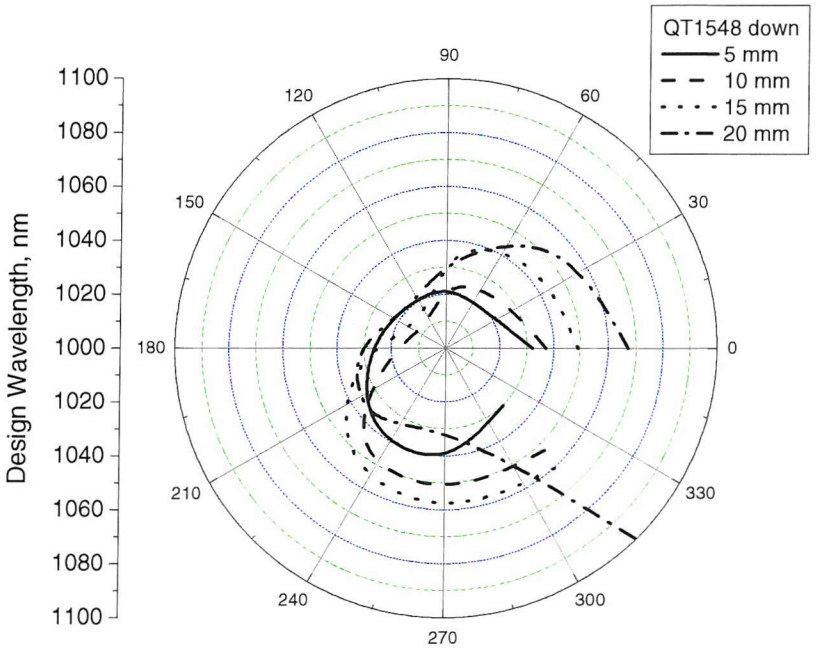


**Fig. A. 12:** Experimentally measured design wavelength shift in the reflection spectrum across QT1548-down wafer.

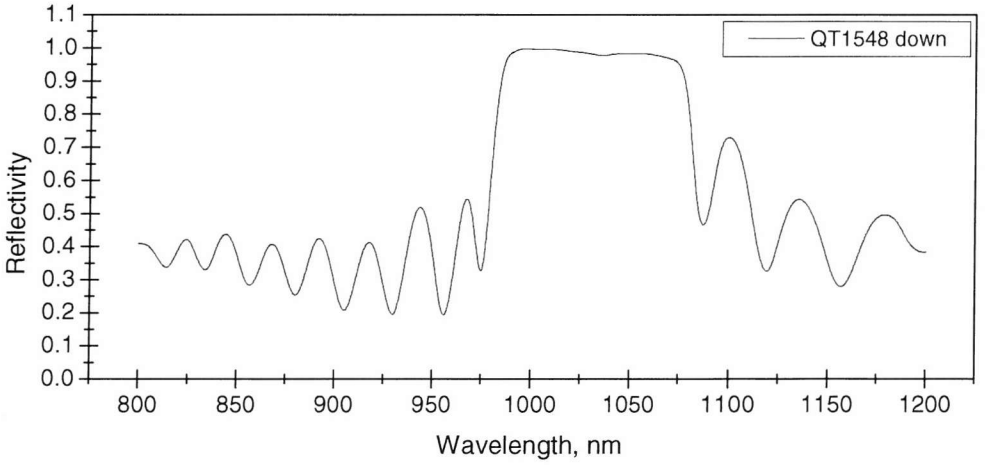


**Fig. A. 13:** Experimentally measured the reflection spectrum at one point of QT1548-down wafer.

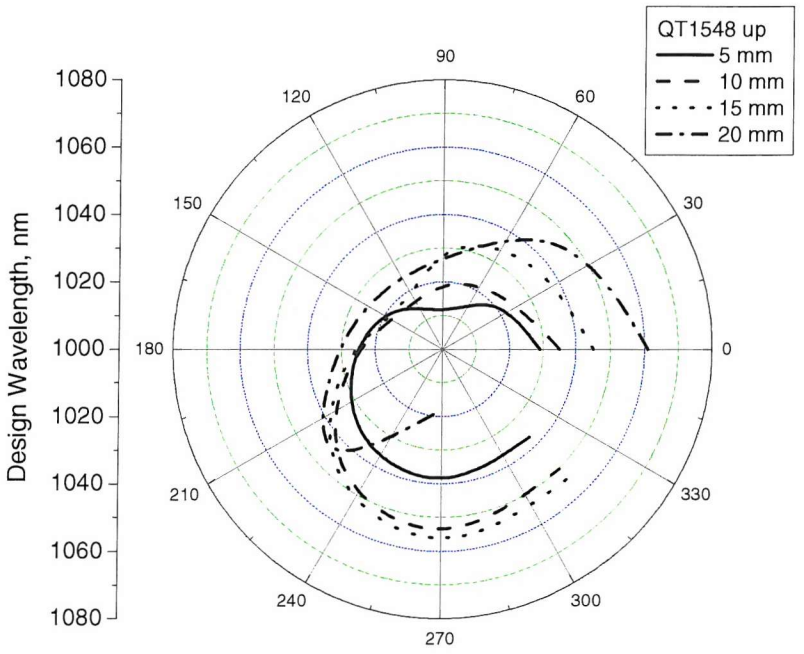


**Fig. A. 14:** Experimentally measured design wavelength shift in the reflection spectrum across QT1548-up wafer.

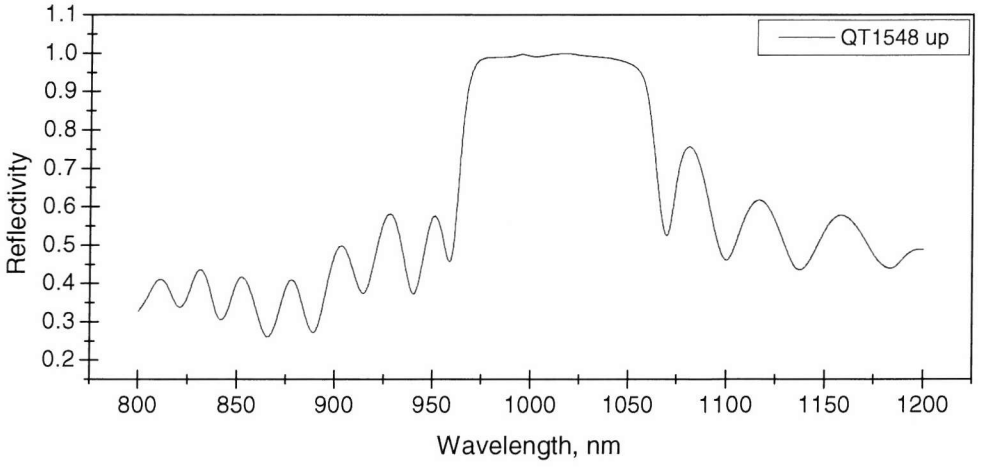


**Fig. A. 15:** Experimentally measured the reflection spectrum at one point of QT1548-up wafer.

4. I-type SUSAM QT1563 sample, standard MOCVD growth.

Ingot Number Up-WV 2067.008/Un, (100) $3^0 \rightarrow$ (110) $\alpha = 45^0$;

Ingot Number Down-WV 2067.019/Un, (100) $3^0 \rightarrow$ (110) $\alpha = 45^0$;

Structure formula: 62S □ buffer LC $[HL]^{27}$ 0.204H $0.13L_{qw}$ $[0.142H\ 0.136L_s]^2$ 0.109H □ 1.0; ($\lambda_0 = 1.03$ μm, $n_L(AlAs) = 2.94$, $n_{Ls}(In_{0.20}Ga_{0.80}As) = 3.342$, $n_{Lqw}(In_{0.25}Ga_{0.75}As) = 3.344$ $n_H(Al_{0.1}Ga_{0.9}As) = 3.433$, $n_S(GaAs) = 3.496$), LC – loss component. Device contains single 10-nm thick GaAs-$In_{0.25}Ga_{0.75}As$-GaAs designed to have maximum absorption at 1.04 μm.

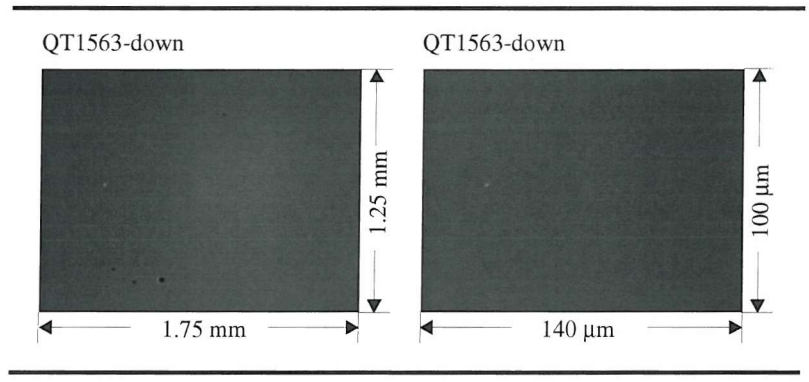


**Fig. A. 16:** Microscope images of QT1563-down sample.

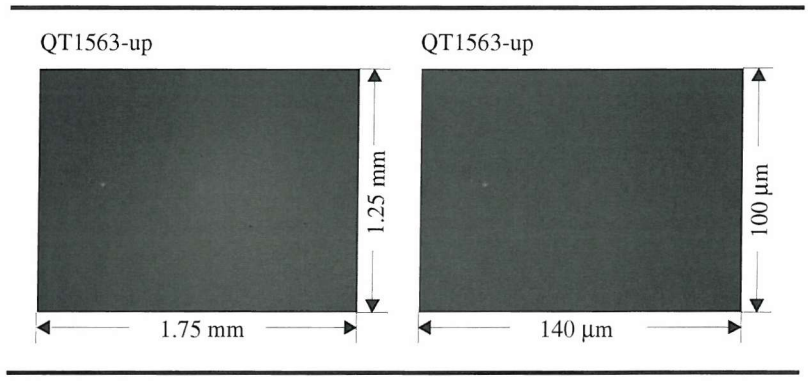


**Fig. A. 17:** Microscope images of QT1563-up sample.

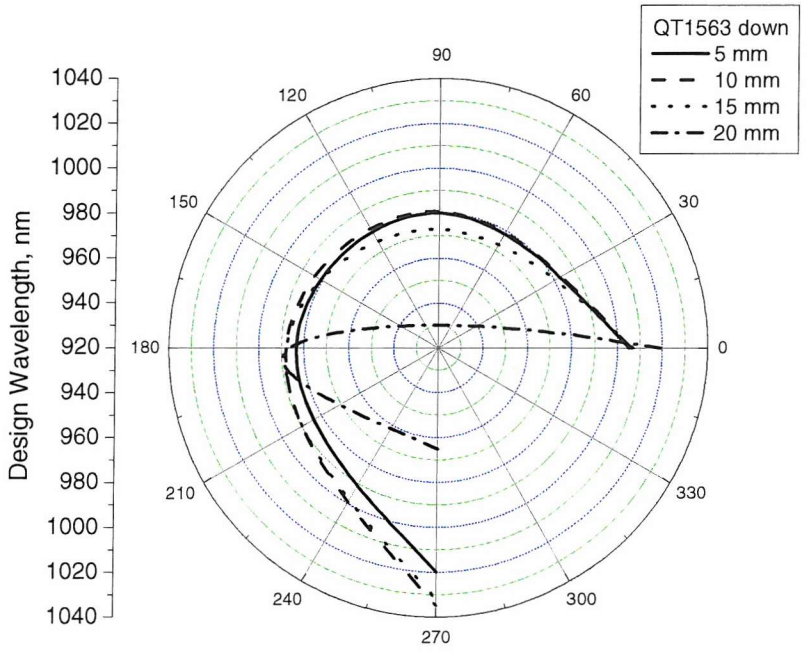


**Fig. A. 18:** Experimentally measured design wavelength shift in the reflection spectrum across QT1563-down wafer.

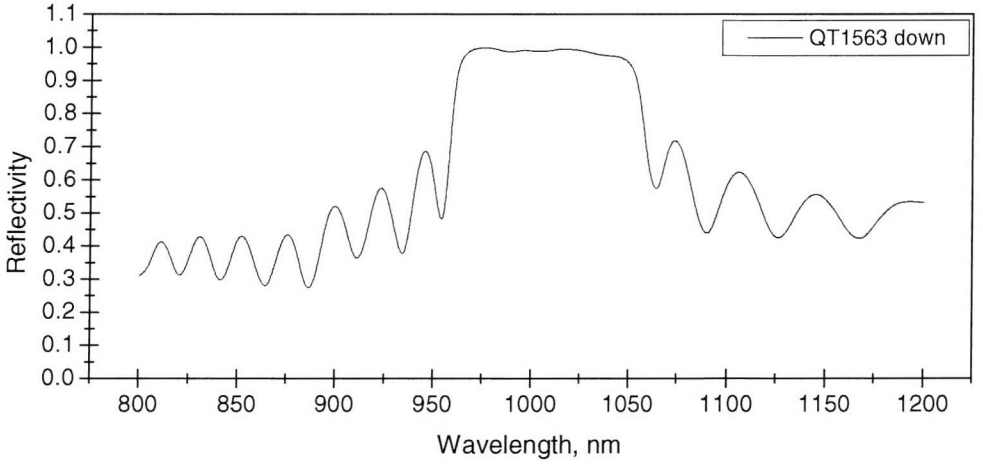


**Fig. A. 19:** Experimentally measured the reflection spectrum at one point of QT1563-down wafer.

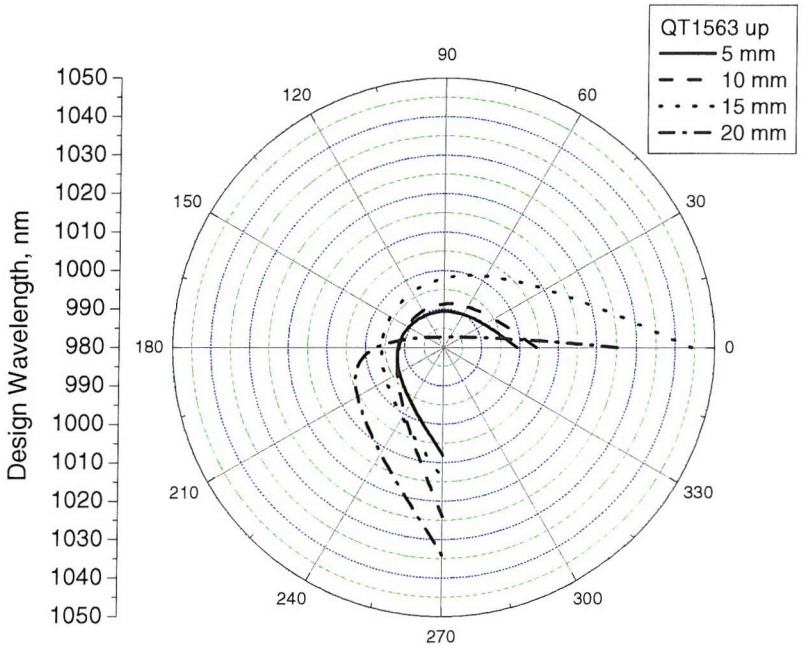


**Fig. A. 20:** Experimentally measured design wavelength shift in the reflection spectrum across QT1563-up wafer.

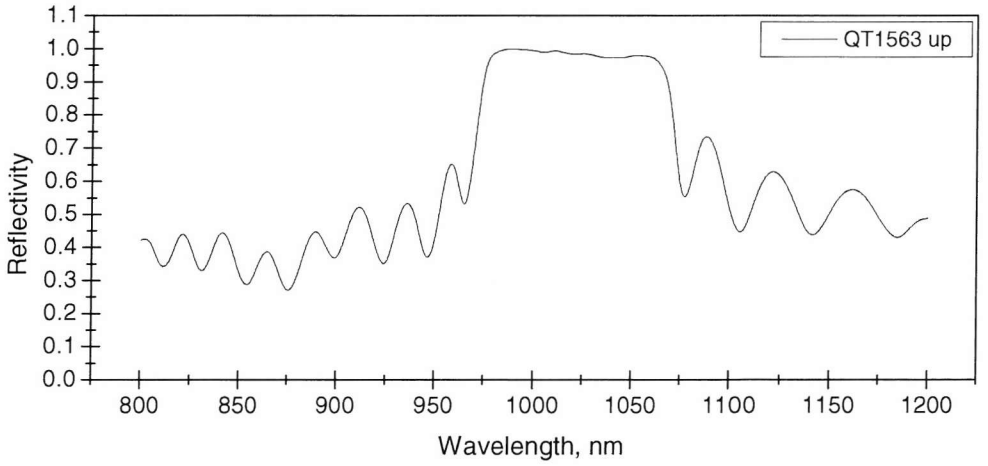


**Fig. A. 21:** Experimentally measured the reflection spectrum at one point of QT1563-up wafer.

5. I-type SUSAM QT1580 sample, standard MOCVD growth.

Ingot Number Up-WV 2067.003/Un, (100) $3^0 \rightarrow$ (110) $\alpha = 45^0$;

Ingot Number Down-WV 2067.001/Un, (100) $3^0 \rightarrow$ (110) $\alpha = 45^0$;

Structure formula: 64S □ buffer LC $[HL]^{27}$ 0.204H $0.13L_{qw}$ $[0.095H\ 0.091L_s]^3$ 0.109H □ 1.0; ($\lambda_0 = 1.03$ μm, $n_L(AlAs) = 2.94$, $n_{Ls}(In_{0.20}Ga_{0.80}As) = 3.342$, $n_{Lqw}(In_{0.25}Ga_{0.75}As) = 3.344$ $n_H(Al_{0.1}Ga_{0.9}As) = 3.433$, $n_S(GaAs) = 3.496$), LC – loss component. Device contains single 10-nm thick GaAs-$In_{0.25}Ga_{0.75}As$-GaAs designed to have maximum absorption at 1.04 μm.

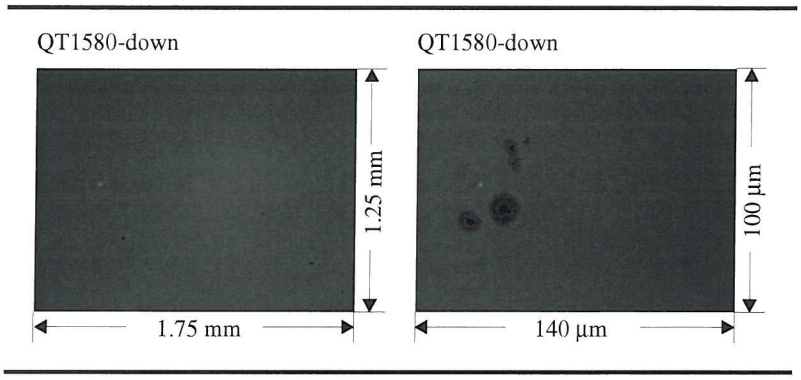


**Fig. A. 22:** Microscope images of QT1580-down sample.

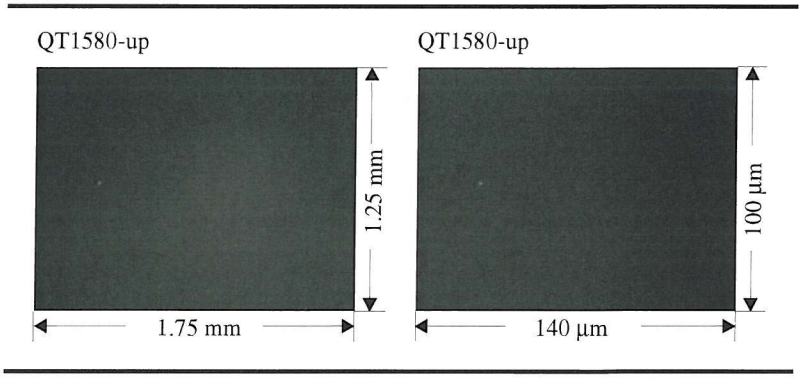


**Fig. A. 23:** Microscope images of QT1580-up sample.

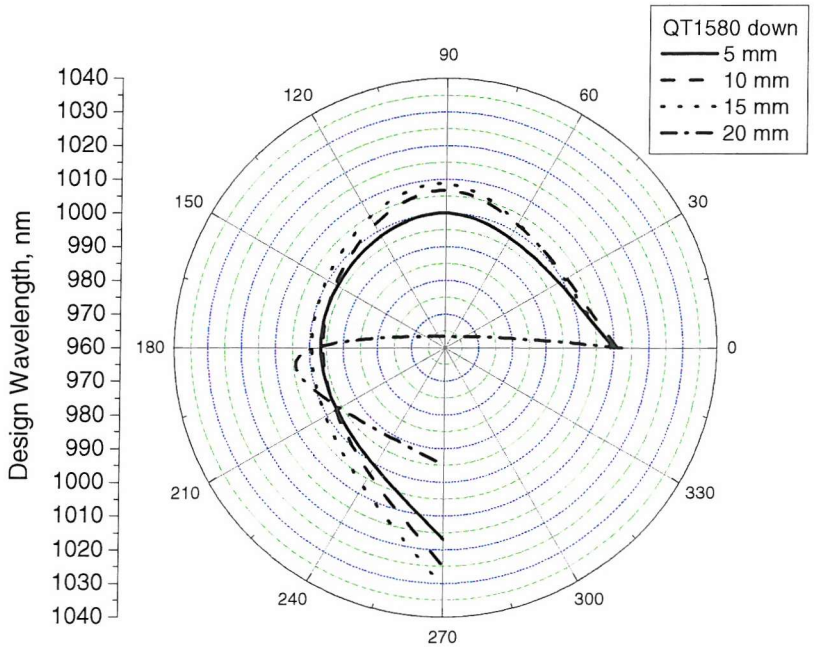


**Fig. A. 24:** Experimentally measured design wavelength shift in the reflection spectrum across QT1580-down wafer.

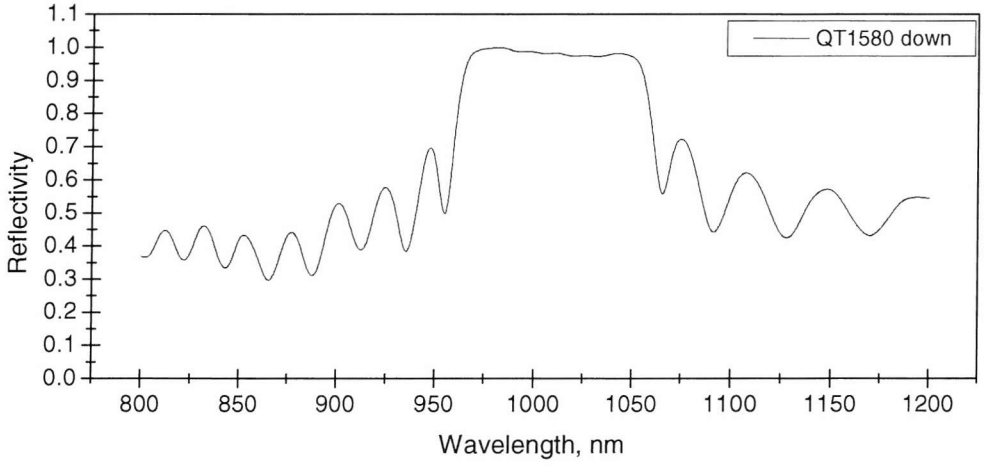


**Fig. A. 25:** Experimentally measured the reflection spectrum at one point of QT1580-down wafer.

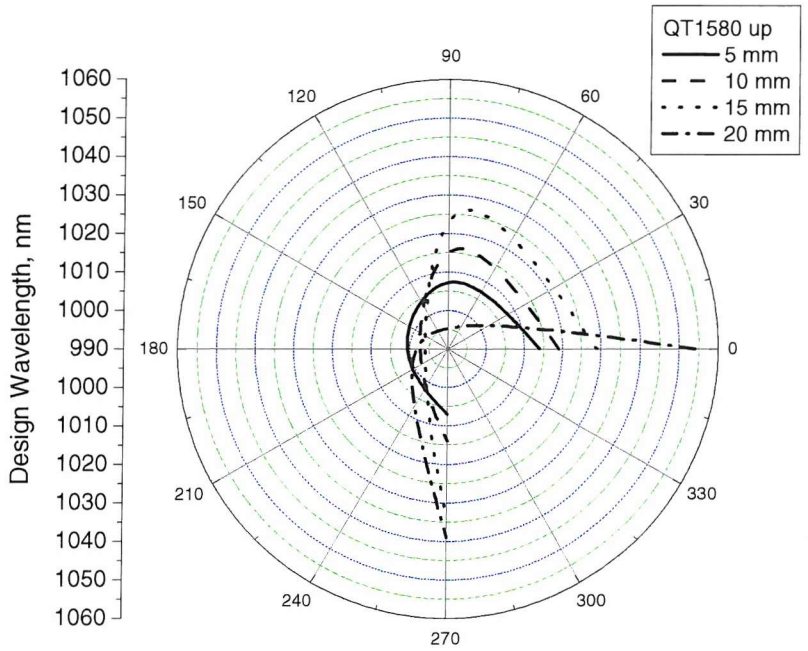


**Fig. A. 26:** Experimentally measured design wavelength shift in the reflection spectrum across QT1580-up wafer.

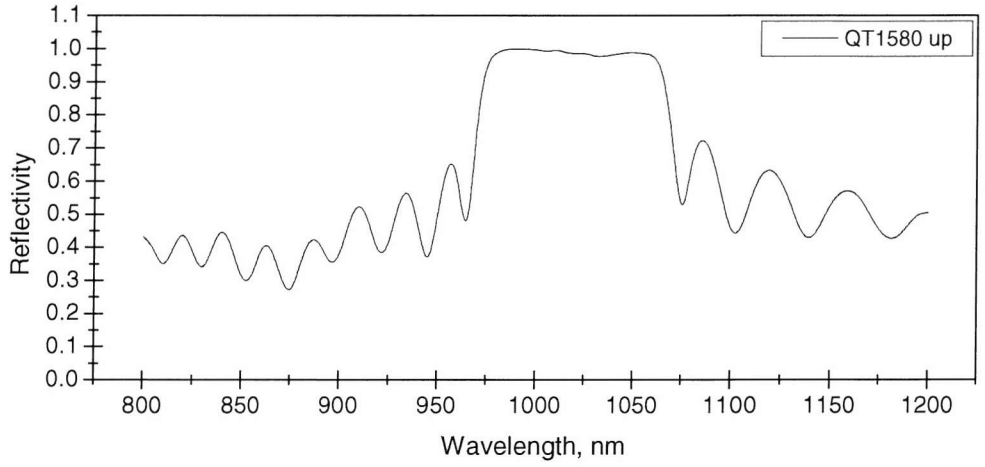


**Fig. A. 27:** Experimentally measured the reflection spectrum at one point of QT1580-up wafer.

6. Test sample (only superlattice).

QT1608A sample, standard MOCVD growth:

Ingot Number WV 7842.048/Un, (100) $3^0 \rightarrow$ (110) $\alpha = 45^0$;

Structure formula: 7S □ buffer [0.095H 0.091$L_s$]$^3$ 0.109H □ 1.0; ($\lambda_0 = 1.03$ μm, $n_L(AlAs) = 2.94$, $n_{Ls}(In_{0.20}Ga_{0.80}As) = 3.342$, $n_H(Al_{0.1}Ga_{0.9}As) = 3.433$, $n_S(GaAs) = 3.496$). Device contains superlattice having three 7-nm thick GaAs-$In_{0.20}Ga_{0.80}As$-GaAs QWs designed to have maximum absorption at 1.01 μm.

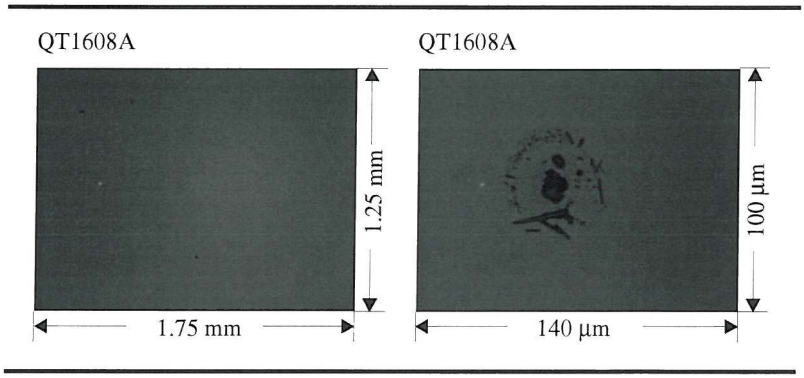


**Fig. A. 28:** Microscope images of QT1608A sample.

7. Test sample (QW & superlattice).

QT1608B sample, standard MOCVD growth:

Ingot Number WV 8031.009/Un, (100) $3^0 \rightarrow$ (110) $\alpha = 45^0$;

Structure formula: 9S □ buffer 0.204H $0.13L_{qw}$ $[0.095H\ 0.091L_s]^3$ 0.109H □ 1.0;

($\lambda_0 = 1.03$ μm, $n_L(AlAs) = 2.94$, $n_{Ls}(In_{0.20}Ga_{0.80}As) = 3.342$, $n_{Lqw}(In_{0.25}Ga_{0.75}As) = 3.344$ $n_H(Al_{0.1}Ga_{0.9}As) = 3.433$, $n_S(GaAs) = 3.496$). Device contains single 10-nm thick GaAs-$In_{0.25}Ga_{0.75}As$-GaAs designed to have maximum absorption at 1.04 μm and superlattice having three 7-nm thick GaAs-$In_{0.20}Ga_{0.80}As$-GaAs QWs designed to have maximum absorption at 1.01 μm.

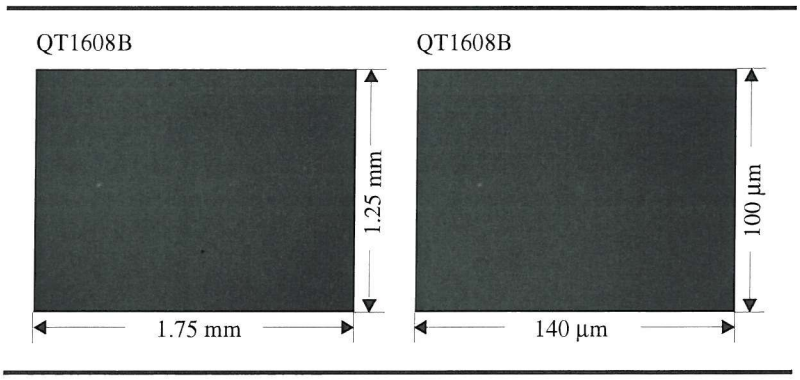


**Fig. A. 29:** Microscope images of QT1608B sample.

8. DP-VECSEL QT1656 sample, standard MOCVD growth.

Ingot Number Up-WV 7842.061/Un, (100) $3^0 \rightarrow$ (110) $\alpha = 45^0$;

Ingot Number Down-WV 7842.059/Un, (100) $3^0 \rightarrow$ (110) $\alpha = 45^0$;

Device contains 6 10-nm thick $GaAs_{0.94}P_{0.06}$-$In_{0.20}Ga_{0.80}As$-$GaAs_{0.94}P_{0.06}$ QW's design to have maximum absorption at 1.01 μm (Fig. CH.II. 8-8. 1, 2., Table CH.II.8-8. 1.)

AR structure formula: 11S □ 0.572L [0.667H 1.143L]$^2$ 0.667H 1.715L [0667H 1.143L]$^2$ □ 1.0; HR structure formula: 71S □ buffer 0.59L 1.03H 0.88L 1.37H 0.88L 1.03H 1.18L 0.35H 1.18L 0.69H 1.18L [1.03H 0.88L]$^2$ 1.37H [0.88L 1.03H]$^3$ 0.88L 1.37H [0.88L 1.03H]$^3$ 0.88L 1.37H [0.88L 1.03H]$^3$ 0.88L 1.37H [0.88L 1.03H]$^3$ 0.88L 1.37H [0.88L 1.03H]$^3$ 0.88L 1.37H [0.88L 1.03H]$^3$ 0.73L □ 3.496; ($\lambda_0 = 1.03$ μm, $n_L(AlAs) = 2.94$, $n_H(Al_{0.1}Ga_{0.9}As) = 3.433$, $n_S(GaAs) = 3.496$).

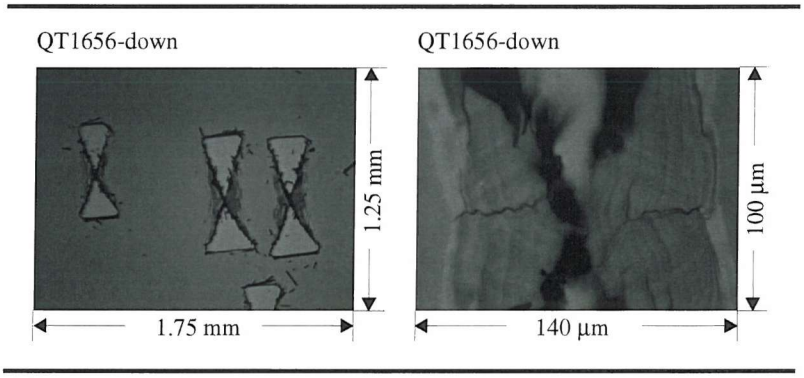


**Fig. A. 30:** Microscope images of QT1656-down sample.

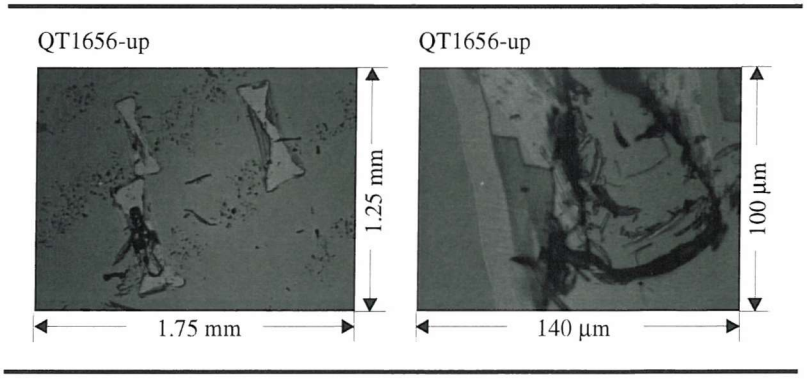


**Fig. A. 31:** Microscope images of QT1656-up sample.

9. DP-VECSEL QT1677 sample, standard MOCVD growth.

Ingot Number Up-WV 7842.075/Un, (100) $3^0 \rightarrow$ (110) $\alpha = 45^0$;

Ingot Number Down-WV 7842.067/Un, (100) $3^0 \rightarrow$ (110) $\alpha = 45^0$;

Device contains 6 10-nm thick $GaAs_{0.94}P_{0.06}$-$In_{0.20}Ga_{0.80}As$-$GaAs_{0.94}P_{0.06}$ QW's design to have maximum absorption at 1.01 μm (Fig. CH.II. 8-8. 1, 2., Table CH.II.8-8. 1.)

AR structure formula: 11S □ 0.572L [0.667H 1.143L]$^2$ 0.667H 1.715L [0667H 1.143L]$^2$ □ 1.0; HR structure formula: 71S □ buffer 0.59L 1.03H 0.88L 1.37H 0.88L 1.03H 1.18L 0.35H 1.18L 0.69H 1.18L [1.03H 0.88L]$^2$ 1.37H [0.88L 1.03H]$^3$ 0.88L 1.37H [0.88L 1.03H]$^3$ 0.88L 1.37H [0.88L 1.03H]$^3$ 0.88L 1.37H [0.88L 1.03H]$^3$ 0.88L 1.37H [0.88L 1.03H]$^3$ 0.88L 1.37H [0.88L 1.03H]$^3$ 0.73L □ 3.496; ($\lambda_0 = 1.03$ μm, $n_L(AlAs) = 2.94$, $n_H(Al_{0.1}Ga_{0.9}As) = 3.433$, $n_S(GaAs) = 3.496$).

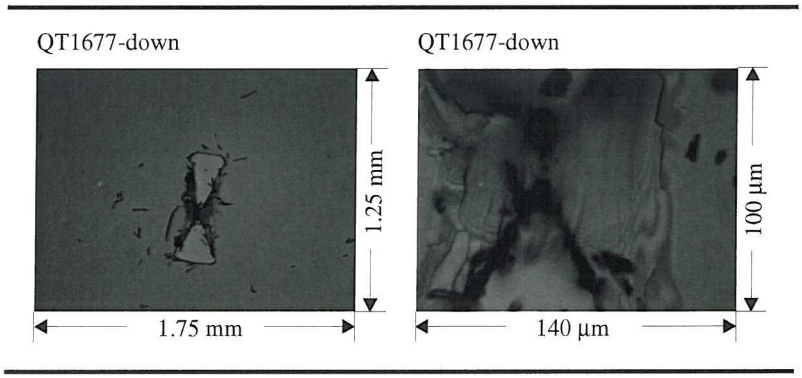


**Fig. A. 32:** Microscope images of QT1677-down sample.

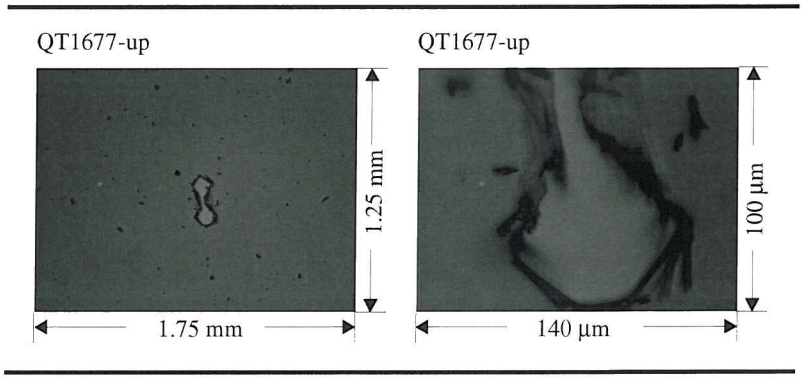


**Fig. A. 33:** Microscope images of QT1677-up sample.

Perhaps it is worth to add that the last two attempts to grow DP-VECSEL gain structures (QT1656 and QT1677 samples) were unsuccessful. Both "down" and "up" wafers of both attempts were having remarkable surface degradation with very complex combination of surface defects. These samples were designed to have strain-balanced structure. However high density of crater-like surface defects have shown growth problems associated with balancing the growth reaction. It seems that grown samples were still degrading over some period of time. On other hand SUSAMs (QT1563 and QT1580 samples) designed to have integrated strained superlattice have shown very perfect growth with very small amount of surface defects.

# APPENDIX B

## LOW-INSERTION-LOSS SUPERLATTICE-BASED SATURABLE ABSORBER MIRROR FOR SEMICONDUCTOR LASER MODE LOCKING

This paper was presented at the international quantum electronics conference on lasers, applications, and technologies (IQEC/LAT) in Moscow, Russia (June 22-27, 2002). It is the first publication that concludes first demonstration of a novel low-loss superlattice-based saturable absorber mirror (SUSAM) in which a strained superlattice enhances quantum well carrier recombination. 5-ps pulse generation at a repetition rate of 330 MHz with average power of up to 45 mW in a circular diffraction-limited beam from an external cavity surface-emitting semiconductor laser (DP-VECSEL) has been demonstrated.

# Low-insertion-loss superlattice-based saturable absorber mirror for semiconductor laser mode locking

*K. Vyšniauskas*[a], P. Suret[a], M. Jones[a], S. Hoogland[a], A Garnache[a], A. C. Tropper[a], J. S. Roberts[b]

[a] Department of Physics and Astronomy, University of Southampton, Southampton SO17 1BJ, UK.
kv@phys.soton.ac.uk / Tel. +44.2380.592.066 / Fax +44.2380.593.910
[b] EPSRC Central Facility for III-V Semiconductors, Department of Electronics and Electric Engineering, University of Sheffield, Mappin Street, Sheffield S1 3JD, UK.

Semiconductor saturable absorber mirrors (SESAMs) are used for numerous applications, such as laser tuning elements, wavelength-sensitive detectors [1], optical noise pulse suppression in high-speed optical communication [1], and in particular for passive mode-locking of a variety of solid-state laser materials [2]. Fast recovery of the saturable absorption can be achieved, for example using quantum wells (QW) grown by molecular-beam-epitaxy (MBE) at low temperatures to enhance carrier recombination rates. The use of low temperature MBE growth however introduces non-saturable losses [3]. It has recently been shown that SESAMs can mode-lock diode-pumped external-cavity surface-emitting lasers (DP-VECSELs) [4]. However the performance of these inherently low-gain devices is sensitive to the non-saturable loss.

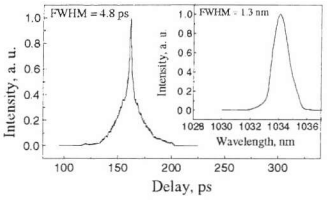


Fig. 1. Autocorrelation and optical spectrum (inset).

We report a novel superlattice-based design of saturable absorber mirror (SUSAM), grown by metal-organic chemical-vapor deposition (MOCVD) under standard conditions, in which a strained superlattice, adjacent to the absorbing quantum well, provides sufficiently rapid absorption recovery that this device has been used to mode-lock a DP-VECSEL at a repetition rate of 330 MHz. The insertion loss of this device is estimated to be <0.3%; roughly half that of a comparable low temperature grown SESAM. The SUSAM saturable absorber is a single $In_{0.26}Ga_{0.74}As$:GaAs QW adjacent to a 3-repeat GaAs:$In_{0.2}Ga_{0.8}As$ superlattice. The 26.5-pair distributed Bragg reflector is optically isolated from the substrate by two $In_{0.26}Ga_{0.74}As$ QWs. The generated chirped pulses at 1034 nm are 5 ps long (FWHM – full width at half maximum), as evident from the measured autocorrelation and optical spectrum shown in Fig. 1. The maximum average output power of 45 mW was obtained.

In summary, we demonstrate a novel type of MOCVD-grown saturable absorber mirror, in which a strained superlattice is used to shorten the carrier lifetime without increasing significantly non-saturable losses. A SUSAM structure has been used to mode lock a DP-VECSEL at 1034 nm, generating chirped 5-ps pulses at a repetition rate of 330 MHz with average power of up to 45 mW in a circular diffraction-limited beam.

References:

1. D. A. B. Miller, *IEEE J. Quantum Electron.*, vol. 30, pp. 732-749, 1994.
2. U. Keller, Kurt J. Weingarten, Franz X. Kärtner, *IEEE* Journal of Selected Topics in Quantum Electronics, vol. 2, No. 3, September 1996.
3. D. Kopf, G. Zhang, R. Fluck, M. Moser, and U. Keller, Optics Letters, vol. 21, No. 7. April 1996.
4. S. Hoogland, S. Dhanjal, A. C. Tropper, *Member, IEEE,* J. S. Roberts, and U. Keller, *IEEE Photon. Technol. Lett.*, vol. 12, pp. 1135-1137, 2000.